

CHARACTERIZATION OF THIN BIOLOGICAL FILMS BY RAMAN AND FOURIER
TRANSFORM INFRARED SPECTROSCOPY

by

MICHAEL ROLAND MURPHY

(Under the Direction of RICHARD A. DLUHY)

ABSTRACT

Applications of thin films and coatings span the entire gamut of science and technology. As new methods of manufacturing thin films develop, new techniques to study the films must also develop. The work presented in this dissertation demonstrates the effectiveness of Raman and Infrared spectroscopy for the analysis of thin and monomolecular films. In Chapter III, both horizontal attenuated total reflection spectroscopy and Raman microscopy are used for the characterization of a biomimetic film designed for an implantable medical device. HATR FTIR was used to verify the results obtained by Raman microscopy. Infrared analysis is the acknowledged method for determining percent polymerization but due to water interference in the sample, this was not possible. Raman microscopy was verified to be a suitable alternative to infrared spectroscopy for the determination of percent polymerization in these types of samples, thus providing an additional analysis tool for the researcher.

Horizontal attenuated total reflection infrared spectroscopy is used for real-time monitoring of photoinitiated polymerization in Chapter IV. The classical metallocenes, ferrocene and ruthenocene, as well as benzoyl-substituted versions of each are investigated as anionic photoinitiators. The use of HATR real-time monitoring allows for the determination of percent

polymerization at any point during the reaction as well as providing data that can be used to calculate the rate of polymerization. The use of the metallocenes as photoinitiators provides for an enormous reduction in the amount of solvent necessary for the photoinitiation process.

Unenhanced Raman spectroscopy of monolayers at the air-water interface has met with limited success. In Chapter V, the design and implementation of a custom designed trough for air-water studies is discussed. This novel sample interface was developed to acquire spectra of monomolecular films at the air-water interface. Using total internal reflection sampling geometry and a leveling device to maintain constant water level, a spectrum of an arachidic acid monolayer film was obtained.

INDEX WORDS: RAMAN SPECTROSCOPY, RAMAN MICROSCOPY, RAMAN, AIR-WATER INTERFACE, A/W INTERFACE, FT-IR, HATR, ATR, PHOSPHOLIPIDS, BIOMATERIALS, MEMBRANE-MIMETIC FILM, SURFACTANT PROTEINS, BIOMEMBRANES, VIBRATIONAL SPECTROSCOPY, PHOTOINITIATION, METALLOCENES

CHARACTERIZATION OF THIN BIOLOGICAL FILMS BY RAMAN AND FOURIER
TRANSFORM INFRARED SPECTROSCOPY

by

MICHAEL ROLAND MURPHY

B.A., Southern Illinois University at Carbondale, 1998

A Dissertation Submitted to the Graduate Faculty of The University of Georgia in Partial
Fulfillment of the Requirements for the Degree

DOCTOR OF PHILOSOPHY

ATHENS, GEORGIA

2004

© 2004

MICHAEL ROLAND MURPHY

All Rights Reserved

CHARACTERIZATION OF THIN BIOLOGICAL FILMS BY RAMAN AND FOURIER
TRANSFORM INFRARED SPECTROSCOPY

by

MICHAEL ROLAND MURPHY

Major Professor: RICHARD A. DLUHY

Committee: CHARLES R. KUTAL
MICHAEL K. JOHNSON

Electronic Version Approved:

Maureen Grasso
Dean of the Graduate School
The University of Georgia
May 2004

DEDICATION

I would like to dedicate this work to the people in my life who have encouraged and supported me so that I can be where I am now.

To Marla: I continue to thank God each day that he blessed me by bringing you into my life. Your love, understanding, encouragement, patience, and support these past two years has allowed me to complete this work. Without you, I could not have done this. I love you with all of my heart and look forward to our future together.

To my mother, Joy: I cannot express my gratitude and love with words alone. Thank you for all the sacrifices and the opportunities that you provided for me during this journey. Your love and encouragement laid the foundation for accomplishing this goal. I love you.

To my brother, Dean: You, better than anyone else, know the sacrifices made to reach this goal. Your constant quest for knowledge and desire to excel academically has always been a source of inspiration to me. Thank you for the long talks and advice when I needed it most. I love you.

To my sister, DeAnn: Thank you for all the support and encouragement through the years. Thank you so much for my niece and nephew who also helped Uncle Michael make it through all those long hours of study. I love you all.

To my grandparents, Alice and Roland, and my Great Aunt Pearl: I only wish that you were all still here to share this accomplishment with me. Each of you, in your own way, taught me how important an education is. More importantly than that, you loved me and took the time to teach me right from wrong. You all gave me strong principles to live by and made me a much better person than I would be otherwise. I will never forget you and I will always do my best to make you proud. I miss you all!

ACKNOWLEDGEMENTS

I would like to gratefully acknowledge the people who were instrumental in encouraging me to pursue my doctoral degree.

Grateful acknowledgement is extended to my research advisor, Richard A. Dluhy for the research experience and knowledge that I have received both as a teaching assistant and research assistant and the generous financial support that made this endeavor much easier. I would also like to acknowledge the current and former members of my doctoral committee, Drs. J. A. de Haseth, A.D. King, T.E. Johnson, M.K. Johnson, and C.R. Kutal for their guidance and critical review of my work.

I would also like to thank the current and former members of the Dluhy research group. As mentors and friends, you have made this a more pleasant experience than it would have been otherwise. I wish you all the best of luck in whatever career path that you choose.

I would also like to acknowledge Dr. Joe M. Davis from Southern Illinois University at Carbondale. Your work and guidance while I was an undergraduate researcher in your lab inspired me to pursue a graduate career. It was your mentoring and feedback that helped me to decide that I wanted to pursue a doctoral degree. Well after any professional responsibility was discharged on your part, you also counseled me on career decisions. Thank you for being such a tremendous mentor and friend.

TABLE OF CONTENTS

| | Page |
|--|------|
| ACKNOWLEDGEMENTS | vi |
| LIST OF TABLES | ix |
| LIST OF FIGURES | x |
| CHAPTER | |
| I INTRODUCTION | 1 |
| II LITERATURE REVIEW | 3 |
| Characterization of Thin Films..... | 3 |
| Infrared Spectroscopy..... | 4 |
| Fourier Transform Infrared Spectroscopy (FT-IR) | 9 |
| Attenuated Total Reflectance (ATR) Fourier Transform Infrared Spectroscopy ... | 14 |
| Raman Scattering Theory..... | 18 |
| Classical Theory of Light Scattering from Molecules | 18 |
| Quantum-Mechanical Theory of Light Scattering from Molecules..... | 22 |
| Raman vs. IR | 26 |
| Langmuir Films | 28 |
| Self-Assembled Monolayers | 32 |
| Photo-initiated Polymerization..... | 33 |
| REFERENCES..... | 35 |

| | | |
|-----|--|-----|
| III | ANALYSIS OF PHOTO-INITIATED POLYMERIZATION IN A MEMBRANE MIMETIC FILM USING RAMAN MICROSCOPY AND FOURIER TRANSFORM INFRARED SPECTROSCOPY | 40 |
| | REFERENCES | 76 |
| IV | REAL-TIME FT-IR MEASUREMENTS OF PHOTO-INITIATED POLYMERIZATION | 78 |
| | REFERENCES | 121 |
| V | DEVELOPMENT OF A NOVEL SAMPLING ACCESSORY FOR RAMAN SPECTROSCOPIC STUDIES AT THE AIR-WATER INTERFACE | 126 |
| | REFERENCES | 151 |
| VI | CONCLUSION | 155 |
| | APPENDICES | 157 |
| | A RAW DATA ANALYSIS METHODS FOR CHAPTER III | 158 |

LIST OF TABLES

| | Page |
|---|------|
| Table II-1: The Electromagnetic Spectrum..... | 5 |
| Table A-1: Numerical Values for Raw IR Data..... | 171 |
| Table A-2: Numerical values for Interpolated IR data. | 171 |
| Table A-3: Numerical values for raw Raman data. | 191 |
| Table A-4: Numerical values for smoothed Raman data..... | 191 |
| Table A-5: Numerical values for peak fitting Raman data. | 193 |
| Table A-6: Standard deviation in Raman and IR data measurements. | 195 |
| Table A-7: Raman COG and Peak Fit values for green irradiation..... | 198 |
| Table A-8: Tabulated data for PTFE graft irradiation. | 205 |

LIST OF FIGURES

| | Page |
|---|------|
| Figure II-1: The Electromagnetic Spectrum | 6 |
| Figure II-2: FT-IR Spectrometer Diagram..... | 10 |
| Figure II-3: Internal Reflection Element..... | 16 |
| Figure II-4: Raman Energy Level Diagram | 24 |
| Figure II-5: A pressure-area (π -A) isotherm of stearic acid. | 29 |
| Figure III-1a: Membrane-Mimetic Film | 44 |
| Figure III-1b: Monoacrylate-PC Structure..... | 44 |
| Figure III-2a: FT-IR Spectrum of 12mM Monoacrylate-PC | 47 |
| Figure III-2b: FT-IR Spectrum of Deuterated 12mM Monoacrylate-PC | 47 |
| Figure III-3a: Decrease in C=C Band measured by HATR..... | 51 |
| Figure III-3b: Decrease in Ester Carbonyl Band measured by HATR | 51 |
| Figure III-4a: Decrease in C=C Band measured by Raman Microscopy | 59 |
| Figure III-4b: C-N Stretch measured by Raman Microscopy..... | 59 |
| Figure III-5: Raman vs. ATR Measurement | 62 |
| Figure III-6: Percent Polymerization of Monoacrylate-PC measured by Raman Microscopy..... | 65 |
| Figure III-7a: Raman Spectrum of Graft Prior to Irradiation | 67 |
| Figure III-7b: Raman Spectrum of Graft after Irradiation | 67 |
| Figure III-8: Percent Polymerization for Graft measured by Raman Microscopy | 74 |
| Figure IV-1: Schematic of Photoinitiated Reaction..... | 81 |

| | |
|--|-----|
| Figure IV-2: Metallocene Structure | 84 |
| Figure IV-3: Charge-Transfer-To-Solvent of FeCp ₂ and Electron Accepting Solution | 87 |
| Figure IV-4: Irradiation Assembly Components | 92 |
| Figure IV-5: Spectrum of CA containing FeCp ₂ before irradiation | 94 |
| Figure IV-6: Spectrum of CA containing FeCp ₂ after irradiation | 96 |
| Figure IV-7: Plot of Polymerization versus Time for CA containing FeCp ₂ | 98 |
| Figure IV-8: Mechanism of D-A Complex Between Ferrocene and Solvent..... | 101 |
| Figure IV-9: Spectrum of CA containing RuCp ₂ before irradiation..... | 103 |
| Figure IV-10: Spectrum of CA containing RuCp ₂ after irradiation..... | 106 |
| Figure IV-11: Plot of Polymerization versus Time for CA containing RuCp ₂ | 108 |
| Figure IV-12: Mechanism of Metal-Ring Bond Cleavage of DBF | 110 |
| Figure IV-13: Resonance Structure of DBF | 112 |
| Figure IV-14A: Plot of Polymerization versus Time for CA containing BFC..... | 115 |
| Figure IV-14B: Plot of Polymerization versus Time for CA containing DFC..... | 115 |
| Figure IV-15: Plot of Polymerization versus Time for CA containing BRC | 119 |
| Figure V-1: Photo of Custom Trough Assembly Showing Components | 132 |
| Figure V-2: Cartoon of Water Leveling Device | 135 |
| Figure V-3: Cutaway of Trough Assembly Showing TIR..... | 138 |
| Figure V-4: Raman spectrum of water in the C-H stretching region..... | 140 |
| Figure V-5: Arachidic Acid Monolayer..... | 143 |
| Figure V-6A: Film behavior at low surface pressure with different barrier material..... | 147 |
| Figure V-6B: Film behavior at high surface pressure with different barrier material | 147 |
| Figure A-1A: Sample 1 HATR data decrease in C=C band during irradiation | 159 |

| | |
|---|-----|
| Figure A-1B: Sample 1 HATR data Ester Carbonyl Band during irradiation..... | 159 |
| Figure A-2A: Sample 2 HATR decrease in C=C band during irradiation..... | 162 |
| Figure A-2B: Sample 2 HATR Ester Carbonyl Band during irradiation..... | 162 |
| Figure A-3A: Sample 1 decrease in C=C band during irradiation for interpolated data | 165 |
| Figure A-3B: Ester Carbonyl Band during irradiation for interpolated data | 165 |
| Figure A-4A: Sample 2 decrease in C=C band during irradiation for interpolated data | 168 |
| Figure A-4B: Ester Carbonyl Band during irradiation for interpolated data | 168 |
| Figure A-5A: Sample 1 change in C=C stretch during irradiation | 174 |
| Figure A-5B: Sample 1 change in C-N during irradiation..... | 174 |
| Figure A-6A: Sample 2 change in C=C stretch during irradiation | 177 |
| Figure A-6B: Sample 2 change in C-N stretch during irradiation | 177 |
| Figure A-7A: Sample 1 smoothed C=C stretch during irradiation..... | 180 |
| Figure A-7B: Sample 1 smoothed C-N stretch during irradiation | 180 |
| Figure A-8A: Sample 2 smoothed C=C Stretch during irradiation | 183 |
| Figure A-8B: Sample 2 smoothed C-N stretch during irradiation..... | 183 |
| Figure A-9A: Sample 1 normalized C=C stretch..... | 186 |
| Figure A-9B: Sample 2 normalized C=C stretch..... | 186 |
| Figure A-9C: Sample 1 smoothed and normalized C=C stretch | 186 |
| Figure A-9D: Sample 2 smoothed and normalized C=C stretch | 186 |
| Figure A-10: Plot of percent polymerization Raman vs. IR | 196 |
| Figure A-11A: C=C stretch during irradiation by 514.5 nm light | 200 |
| Figure A-11B: C-N stretch during irradiation by 514.5 nm light | 200 |
| Figure A-12: Normalized C=C data for 514.5 nm irradiation | 203 |

| | |
|--|-----|
| Figure A-13A: PTFE Graft C=C after subtraction | 206 |
| Figure A-13B: PTFE Graft C-N stretch during irradiation..... | 206 |
| Figure A-14: Normalized C=C data from Graft sample | 209 |

Chapter I

INTRODUCTION

In the past two decades, there has been an explosion in the number of applications utilizing thin films. Applications of thin films and coatings span the entire gamut of science and technology, with thin films of semiconductors, metals, insulators, and polymers currently being used in applications such as microelectronic interlayers, computer chip packaging, protective coatings, adhesion, and tribological films. Organic thin films, in particular, are used in implantable medical devices, as coatings on quartz crystal microbalances for the detection of chemical warfare agents, and in solar cells. With the growing importance of thin films, there has also been a growing need to obtain detailed structural and conformational information about them. The understanding of the physical and chemical properties of the film is essential to the design and fabrication of thin film systems.

Vibrational spectroscopic techniques such as Fourier Transform Infrared Spectroscopy and Raman Spectroscopy are well suited to the analysis of thin films. They have been used to determine structural and conformational information on monomolecular films. Each has been applied in theoretical research and in production line quality control for industry. In this dissertation, these techniques are used to gain structural information from a membrane mimetic film, kinetic information from an anionic photopolymerization, and to study monomolecular films at the air-water interface. The work is presented in chapters that represent different scientific papers.

This chapter serves as an introduction to the work presented in this dissertation. Chapter II is a review of the applicable literature and includes the theory of Raman and Infrared spectroscopy. Chapter II also contains information about Fourier Transform Infrared Spectroscopy (FT-IR) and Horizontal Attenuated Total Reflection (HATR) FT-IR Spectroscopy. Langmuir films and self-assembled monolayers are also discussed in detail. The final section of Chapter II discusses photoinitiated polymerization and the use of photoinitiators. Chapter III details the use of Raman microscopy and Infrared spectroscopy to determine percent polymerization in a membrane mimetic film. This work legitimizes the use of Raman microscopy for the determination of percent polymerization. Chapter IV is a compilation of two experiments that illustrate the use of HATR FT-IR for the determination of percent cure and kinetics of photoinduced polymerization using classical metallocenes as photoinitiators. This work also studies the effect of the inhibitor methanesulfonic acid on the rates of reaction in the polymerization. Chapter V discusses the development of a sampling accessory for the study of monomolecular films at the air-water interface. This accessory was developed for use with Raman spectroscopy and incorporates features not available on models ready for purchase from suppliers such as NIMA. In this chapter, a monolayer spectrum of arachidic acid, collected at the air-water interface, is reported. The final part of this dissertation is a short chapter that summarizes the conclusions reached in each of the previous chapters.

CHAPTER II

LITERATURE REVIEW

Characterization of Thin Films

The continued development of techniques for the design and manufacturing of thin film systems relies heavily upon the availability of methods to determine the physical and chemical properties of the films. Many techniques have been developed in order to acquire information about surface properties and film structure.¹⁻³ Most of these techniques employ electrons or ions as the incident or emitted particles. These particles have a strong interaction with materials and provide a high sensitivity in the measurement.^{1, 2, 4, 5} However, electron and ion-based techniques have the limitation that they are only suited for measurements at vacuum-solid interfaces and may damage the film that is being studied. Additionally, not all techniques are applicable for in-situ experiments.⁶ Due to these limitations, a continuous search for new techniques and improvement of existing techniques such as Scanning Tunneling Microscopy and Atomic Force Microscopy continues.^{1, 7-11}

Vibrational spectroscopy has been shown to be an attractive alternative to the previously mentioned techniques. Raman and Infrared spectroscopy are the two most commonly used types of vibrational spectroscopy and are utilized throughout this manuscript. Each has been shown to be sensitive for surface analysis and can be used on a wide variety of samples. They are nondestructive, although photobleaching or thermal damage may occur from incident laser intensity with Raman spectroscopy. Sensitivity to biological systems has been proven to the monolayer level with both techniques.¹²⁻¹⁴ Each of these techniques and their applications to thin film analysis will be discussed in detail later in this chapter.

Infrared Spectroscopy

Infrared or IR spectroscopy is one type of vibrational spectroscopy. Vibrational spectroscopy is used to examine molecular vibrations. Most of what we know today about the structure of atoms and molecules comes from studying their interaction with light, which we also know as electromagnetic radiation. The electromagnetic spectrum is the term that we use to refer to the entire range of light, both visible and invisible to the naked eye. Different regions of this spectrum provide different kinds of information based on their interaction. A given frequency or wavelength of light has an energy associated with it that we call a photon as illustrated in Table II-1. The relationship between frequency and wavelength is given by

$$\lambda\nu = c \quad (\text{II-1})$$

where λ = wavelength, ν = frequency, and c = velocity of light

The relationship between frequency and energy is given by

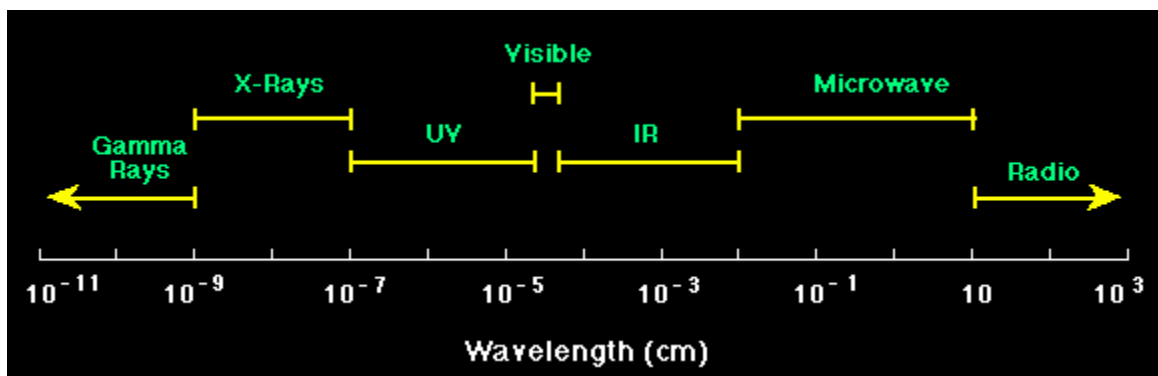
$$E = h\nu \quad (\text{II-2})$$

where E = energy and h = Planck's constant. We see that energy and frequency change proportionally but wavelength has an inverse relationship with these quantities. It is for this reason that the most commonly used unit of measure in spectroscopy is reciprocal centimeters, or as they are more commonly called, wavenumbers (cm^{-1}). On the immediate high energy side of the visible region in the electromagnetic spectrum lies the ultraviolet region and on the low energy side lies the infrared region (Figure II-1). The portion of the infrared region most useful for analysis of organic compounds falls between 2.5 and 25 μm or between 4,000 and 400 wavenumbers (cm^{-1}). Photon energies associated with this part of the infrared are not large enough to excite electrons, but may induce vibrational excitation of covalently bonded atoms and

Table II-1. The Electromagnetic Spectrum. This table shows the different regions of the electromagnetic spectrum along with their corresponding wavelength, frequency, and energy values.

| Spectrum of Electromagnetic Radiation | | | | |
|--|-------------------------------|---------------------------------------|---|--------------------|
| Region | Wavelength (Angstroms) | Wavelength (centimeters) | Frequency (Hz) | Energy (eV) |
| Radio | $> 10^9$ | > 10 | $< 3 \times 10^9$ | $< 10^{-5}$ |
| Microwave | $10^9 - 10^6$ | $10 - 0.01$ | $3 \times 10^9 - 3 \times 10^{12}$ | $10^{-5} - 0.01$ |
| Infrared | $10^6 - 7000$ | $0.01 - 7 \times 10^{-5}$ | $3 \times 10^{12} - 4.3 \times 10^{14}$ | $0.01 - 2$ |
| Visible | $7000 - 4000$ | $7 \times 10^{-5} - 4 \times 10^{-5}$ | $4.3 \times 10^{14} - 7.5 \times 10^{14}$ | $2 - 3$ |
| Ultraviolet | $4000 - 10$ | $4 \times 10^{-5} - 10^{-7}$ | $7.5 \times 10^{14} - 3 \times 10^{17}$ | $3 - 10^3$ |
| X-Rays | $10 - 0.1$ | $10^{-7} - 10^{-9}$ | $3 \times 10^{17} - 3 \times 10^{19}$ | $10^3 - 10^5$ |
| Gamma Rays | < 0.1 | $< 10^{-9}$ | $> 3 \times 10^{19}$ | > 1 |

Figure II-1. The Electromagnetic Spectrum.



groups. Covalent bonds may bend and stretch, as a result, bond lengths and angles are continuously changing. So, in addition to the rotation of groups about a single bond, molecules also undergo a wide range of vibrational motions characteristic of their component atoms. Consequently, nearly all, organic compounds will absorb infrared radiation that corresponds in energy to these vibrations.

A molecule absorbs infrared radiation when the vibration of the atoms in the molecule produces an oscillating electric field with the same frequency as the frequency of incident IR radiation. All of the motions can be described in terms of two types of molecular vibrations. One type of vibration, a stretch, produces a change of bond length. A stretch is a rhythmic movement along the line between the atoms so that the interatomic distance is either increasing or decreasing. The second type of vibration, a bend, results in a change in bond angle. These are also sometimes called scissoring or rocking motions. Each of these two main types of vibration can have variations. A stretch can be symmetric or asymmetric. Bending can occur in the plane of the molecule or out of plane; it can be scissoring, like blades of a pair of scissors, or rocking, where two atoms move in the same direction.¹⁵ Different stretching and bending vibrations can be visualized by considering the CH₂ group in hydrocarbons. The stretching motions require more energy than the bending ones. Higher wavenumbers are indicative of the higher energy required for these vibrations. Lower wavenumber values are consistent with the lower energy required to cause these vibrations.¹⁶

Any given molecule absorbs a unique set of IR light frequencies and its IR spectrum is often likened to a person's fingerprints. However, it only absorbs those frequencies of IR light that match vibrations causing a change in the dipole moment of the molecule. Bonds in symmetric molecules such as N₂ and H₂ do not absorb IR radiation because stretching does not

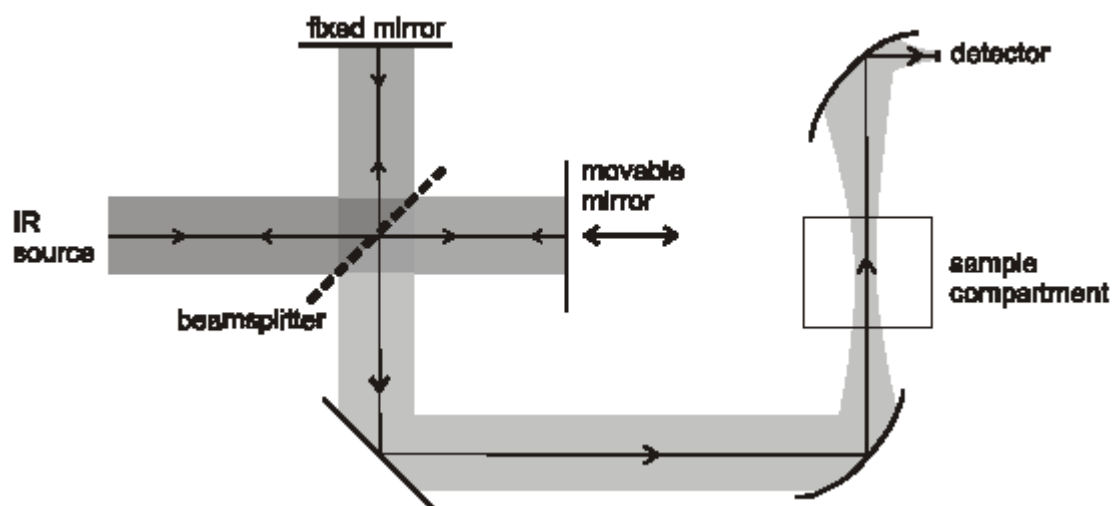
change the dipole moment and bending cannot occur with only 2 atoms in the molecule. Any individual bond in an organic molecule with symmetric structures and identical groups at each end of the bond will not absorb in the IR range. In a complicated molecule, many fundamental vibrations are possible, but not all are observed. Some motions do not change the dipole moment for the molecule, while others are so much alike energetically that they coalesce into one band.

Even though each molecule has its own unique IR spectrum, there are certain groups of atoms that give rise to absorption bands at or near the same wavenumber, regardless of the structure of the rest of the molecule.¹⁷ These persistent characteristic bands enable you to identify major structural features of the molecule after a quick inspection of the spectrum and aid in rapid identification of compounds.

Fourier Transform Infrared Spectroscopy (FT-IR)

The development of interferometry occurred in 1880 when Dr. Albert A. Michelson invented his interferometer to study the speed of light and to fix the standard meter with the wavelength of a known spectral line.¹⁸ Most FT-IR spectrometers are based on Michelson's interferometer and are designed according to the general set-up depicted in Figure II-2. The spectrometer is based on the Michelson interferometer, which is the left part of Figure II-2. In an interferometer, a polychromatic beam of radiation is divided into two beams. These two beams are recombined after a path length difference has been introduced, allowing interference to occur between the beams. The intensity variations of the resulting beam are measured as a function of the path length difference. The Michelson interferometer consists of two mutually perpendicular mirrors, one of which is moveable. Between the fixed and moving mirror is a beamsplitter, where the light of the IR source can be partially reflected to the fixed mirror and partially transmitted to the

Figure II-2. FT-IR Spectrometer Diagram.



movable mirror. The spectrometer gives the best performance when the beamsplitter has a transmittance of 50% for the wavenumber region of interest. The resulting beam from the Michelson interferometer is focused in a sample compartment with the help of mirrors. After passing through the sample compartment, the light beam is focused onto the detector.

Because of the effect of interference, the intensity of the beam measured with the detector depends on the difference in path length in the interferometer. The optical path difference, called the retardation δ , is twice the path difference between the two arms of the interferometer. The intensity for a specific wavenumber, ν , at the detector can then be described as:

$$I(\delta) = \frac{1}{2} I^{\circ}(\nu) \{1 + \cos 2\pi\delta\nu\} \quad (\text{II-3})$$

where $I^{\circ}(\nu)$ is the light intensity of the source. Only the varying part of the measured intensity is of interest for FT-IR spectroscopy, so generally the DC-component in the signal is subtracted or filtered out. This signal that remains after filtering the DC-component is called the interferogram, $I(\delta)$. In practice, the light intensity of the source, I° , has additional wavenumber dependence because of instrumental characteristics such as beamsplitter efficiency, mirrors or detector response and the characteristics of the system that is being studied. The interferogram is then written as:

$$I(\delta) = B(\nu) \cos 2\pi\nu\delta \quad (\text{II-4})$$

where $B(\nu)$ gives the single beam spectral intensity of the source at wavenumber ν as modified by the system that is studied and by instrumental response function. The response of the system that is studied is part of this spectrum and can be resolved with a suitable reference measurement that corrects the measured spectrum for the wavenumber dependent intensity of the source and instrument response function. $I(\delta)$ can be seen as the cosine Fourier transform of the spectrum

$B(\nu)$. The spectrum is calculated from the interferogram $I(\delta)$ by computing the cosine Fourier transform of $I(\delta)$, thus giving, the technique its name of FT-IR spectroscopy.

When the spectrum of the light source is continuous, the interferogram can be represented by the integral:

$$I(\delta) = \int_{-\infty}^{\infty} \{B(\nu) \cos 2\pi\nu\delta\} d\nu \quad (\text{II-5})$$

and:

$$B(\nu) = 2 \int_0^{\infty} \{I(\delta) \cos 2\pi\nu\delta\} d\delta \quad (\text{II-6})$$

where the fact that $I(\delta)$ is an even function is taken into account. This means that, provided the light source has sufficient temporal coherence, the spectrum, $B(\nu)$ can be measured with infinitely high resolution from 0 to 4000 cm^{-1} if the moving mirror of the interferometer is scanned over an infinitely long distance. Also, the Fourier transform has to be digitized at infinitely small retardations. In practice, the signal is digitized at finite sampling distances. These distances can be determined from the interference fringes of the light from a calibration He-Ne laser that also passes through the interferometer. Its signal is measured separately from the IR signal and shows a long coherence length. The spectral range that can be measured is greater when the sampling interval is smaller.

FT-IR offers several advantages over dispersive/grating instruments. Although an exhaustive examination of the advantages of FT-IR spectroscopy is beyond the scope of this work, the primary advantages; the Jacquinot and Fellgett advantages will be discussed briefly. The first advantage is the Jacquinot or throughput advantage. FT-IR spectrometry does not require the use of slit or other aperture device, particularly at low resolution, and the total IR-source output can be passed through the sample continuously. Because of that, the total radiation

on the detector is much higher than that in the grating spectrometer, with the same spectral resolution and recording time.¹⁸

$$\frac{(S/N)_{FT}}{(S/N)_G} \approx 200 \quad (\text{II-7})$$

where $(S/N)_{FT}$ is the signal to noise ratio in FT-IR spectrometers and $(S/N)_G$ is the signal to noise ratio in grating spectrometers. The reason for this is that at the optimum resolution the area of the circular aperture in the FT-IR spectrometer is about 200 times larger than the area of the slit in the grating spectrometer. Thus, the SNR is markedly better in FT-IR spectrometers.

The second advantage FT-IR spectrometers have over dispersive grating instruments is the Fellgett or multiplex advantage. In FT-IR spectrometers, all the wavenumbers are recorded simultaneously. The Fellgett advantage comes from the signal-to-noise ratio (SNR) per unit time. The Fellgett advantage is proportional to the square root of the number of resolution elements being monitored, and results from the large number of resolution elements being monitored simultaneously. Due to the multiplex advantage, an FT-IR spectrometer can be about 500 times faster than a dispersive instrument, collecting on a millisecond time scale or faster.

FT-IR has been used extensively for the analysis of thin and monomolecular films. Due to its rapid scan acquisition, it has been used for the study of kinetics in polymerization reactions¹⁹⁻²¹ as discussed in Chapter 5 of this work.

Attenuated Total Reflectance (ATR) Fourier Transform Infrared Spectroscopy

Attenuated Total Reflectance (ATR) is a relatively recent development in sampling techniques used with Fourier transform infrared (FT-IR) spectroscopy. ATR is based on the reflective energy at the optical interface of two media having differing refractive indices. ATR has a sampling depth from tenths of a micrometer to one micrometer (Figure II-7). Spectra are obtained by placing a sample against an internal reflection element (IRE) made of zinc selenide

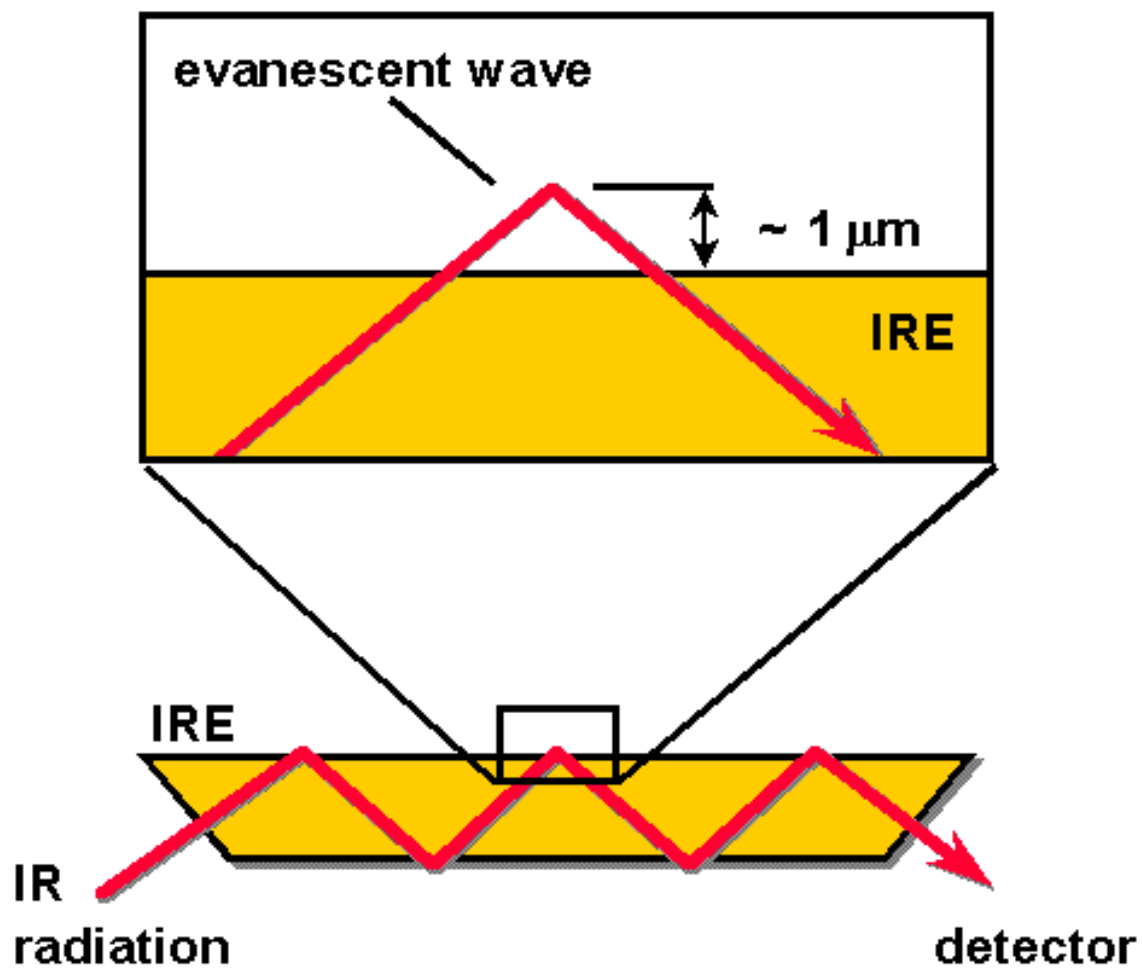
(ZnSe) or germanium (Ge). The IRE is then placed in the sample compartment of a FT-IR spectrometer. The design of the ATR accessory may range from horizontal to more elaborate designs such as the “split pea”. However, the design used for work included in this manuscript was the horizontal ATR (HATR) illustrated in Figure II-3.

In this design, a trapezoidal shaped crystal is mounted horizontally in a holder with the 45-degree slant facing downward. Radiation enters the end of the crystal and is reflected down the length of the IRE at an angle that exceeds the critical angle. At each reflection point, an evanescent wave penetrates beyond the interface into the sample (Figure II-3). One very important aspect is the depth of penetration (d_p) of the evanescent wave into the sample. This quantity is the depth at which the intensity of the electric field (E) goes to e^{-1} times its value at the crystal-sample interface and is given by:

$$d_p = (\lambda_1) / 2\pi(\text{Sin}^2\theta - n_{21}^2)^{1/2} \quad (\text{II-8})$$

where $\lambda_1 = \lambda/n_1$, and $n_{21} = n_2/n_1$. Equation II-8 shows the dependence of d_p on the wavelength of light (λ), the angle of incidence (θ), and the ratio of refractive indices of the sample (n_2) to the crystal (n_1). As the wavelength of light increases, d_p becomes larger. This points out the major spectral difference between samples measured by transmittance and by ATR. Intensities of higher frequency bands will be lower for ATR than for transmittance, while lower frequency bands will be stronger when measured by the ATR technique. It is this unique phenomenon of evanescent waves that allows us to take absorbance spectra of samples that are placed in contact with the IRE. For a much more detailed discussion of the internal reflection technique, readers are encouraged to review N.J. Harrick’s excellent work on the subject.²²

Figure II-3. Internal Reflection Element. Schematic illustrating radiation path through an IRE and the principle of an evanescent wave. Radiation enters the IRE at an angle so that the internal reflection will take place through the element. The top picture shows the penetration of the evanescent wave at the interface.



Raman Scattering Theory

Several reviews may be found in the literature that offer thorough discussions of the Raman scattering phenomenon.^{7, 23-26} Rather than duplicate this effort, only a brief review of the theory will be presented here. Raman data is typically expressed in shifts from the incident radiation in units of wavenumber (cm^{-1}). The shifts that are observed represent the absolute energy differences between eigenstates of the molecule. It is because of this that the wavenumber shifts do not change as a function of the wavelength selected for irradiation. Two different theories exist that attempt to predict the behavior of the Raman scattering phenomenon. The first is the classical light scattering theory and the second is quantum mechanical theory. Although the quantum mechanical theory is more rigorous in its approach, a basic understanding of the Raman scattering phenomenon can be reached through the discussion of the classical light scattering theory. It is because of this that more time will be spent examining this theory. It should be noted that both models are important for a full understanding of this effect and to correctly predict experimental data.

Classical Theory of Light Scattering from Molecules

Several constraints will be placed on the discussion of this theory. For purposes of our discussion, we will assume that the diameter of the molecules (d_m) in question is much smaller than the wavelength of the incident radiation that is striking them. This assumption means that the entire molecule is enveloped in a homogenous electric field. The assumption is also made that the incident radiation is monochromatic, with its frequency represented by ν_0 . Maxwell's equations describe the propagation of electromagnetic (EM) radiation. These equations define the behavior of the electric and magnetic components of the EM radiation in space and time. We assume that the EM radiation is a plane-polarized wave in a homogenous medium. The electric

vector of the incident radiation is directed along the X-axis and is represented by E_x . The magnetic portion of the radiation is oriented orthogonal to E_x and is parallel to the Y-axis. Both components propagate in the Z direction. The electric field, E_x , can thus be described by the following equation.

$$E_x = E_x^0 \exp(-\omega_o \kappa Z / c) \exp[-i\omega_o (nZ / c - t)] \quad (\text{II-9})$$

where $\omega_o = 2\pi\nu_o$. The variables n and κ represent the real and imaginary components of the index of refraction of the medium. The variable c is the speed of light in free space and t represents the time. The amplitude of the EM wave is E^0 and the origin of the z-axis is arbitrary. The factor $\exp[-i\omega_o (nZ / c - t)]$ is periodic in space and time, and the velocity of the propagation of the wave is expressed as c/n . The factor $\exp(-\omega_o \kappa Z / c)$ represents the loss in the EM energy due to absorption by the medium. The variable κ , which is the imaginary part of the refractive index of the medium, is proportional to the absorption coefficient in Beer's Law. In free space, $n = 1$ and $\kappa = 0$.

When the electric field, E_x , impinges on a molecule, an induced oscillating dipole is formed from the polarization of the electron cloud of the molecule. This polarization is represented by α , which stands for the polarizability ($\text{C}^2 \text{m}^2 \text{J}^{-1}$; SI units) of a molecule. The polarizability is the degree to which the molecular orbitals of a molecule are deformed by the presence of an external electric field.²⁶ The polarizability is a tensor composed of nine real components that are derived from the coordinate system and the molecular symmetry of the molecule.

The oscillating dipole induced on a molecule by an external electric field is most commonly described by the following equation:

$$\mu(t) = \alpha(t)E_x(t) \quad (\text{II-10})$$

This equation shows that both α and E_x are time dependent, therefore the induced dipole moment will oscillate in time. The oscillating dipole will then re-emit radiation at the exact frequency of the oscillation. This is the classical model of the scattering process. The polarizability and the incoming electric field may be expressed as harmonic functions. In direct relation to this, equation II-10 predicts that μ will contain a number of frequency components due to the beat pattern between α and E_x . These various components include both elastic and inelastic scattered radiation. Therefore, the scatter produced by the oscillating dipole will be in all directions at all frequency components of the oscillating dipole.

This explanation may be simplified even further. The real part of E_x from equation 1 can be isolated and represented by

$$E_x = E_x^0 \cos(2\pi\nu_0 t) \quad (\text{II-11})$$

A diatomic molecule has a vibration with a frequency ν_v . Assuming a simple harmonic oscillator, the nuclear displacement, q_v , can be expressed as

$$q_v = q_v^0 \cos(2\pi\nu_v t) \quad (\text{II-12})$$

where q_v^0 is the amplitude of the vibration. If the vibration of the diatomic molecule has a small amplitude, then α is a linear function of q_v and can be expanded as a Taylor series in q_v as follows:

$$\alpha = \alpha^0 + \left(\frac{d\alpha}{dq_v}\right)_0 q_v + \dots, \quad (\text{II-13})$$

This equation can be simplified by neglecting higher order terms due to small atomic displacements giving

$$\alpha = \alpha^0 + \left(\frac{d\alpha}{dq_v}\right)_0 q_v^0 \cos(2\pi\nu_v t) \quad (\text{II-14})$$

Substituting this equation for the polarizability into equation 2 leads to the expression

$$\mu = E_x^0 \alpha^0 \cos(2\pi\nu_0 t) + E_x^0 \left(\frac{d\alpha}{dq_v}\right)_0 q_v^0 \cos(2\pi\nu_0 t) \cos(2\pi\nu_v t) \quad (\text{II-15})$$

which is equal to

$$= E_x^0 \alpha^0 \cos(2\pi\nu_0 t) + E_x^0 \left(\frac{d\alpha}{dq_v}\right)_0 q_v^0 \{\cos[(2\pi(\nu_0 - \nu_v)t] + \cos[(2\pi(\nu_0 + \nu_v)t]\} \quad (\text{II-16})$$

The first term, $E_x^0 \alpha^0 \cos(2\pi\nu_0 t)$, represents the oscillation of the induced dipole at the same frequency of the incident radiation and thus the formation of elastic scattered light or as it is more commonly known, Rayleigh scattering. The next two terms represent the inelastic scattered light or Raman scattering. The Raman scatter is composed of radiation that exists at frequencies that are lower than the incident radiation, Stokes ($\nu_0 - \nu_v$), and at frequencies that are more energetic than the incoming radiation, anti-Stokes ($\nu_0 + \nu_v$). From equation II-16, it is obvious that the polarizability tensor, α^0 , will be much larger than its first derivative. This implies that the Rayleigh scatter will be much more intense than the Raman scatter. Experimentally, the Rayleigh scatter is approximately 3 orders of magnitude less than the incoming radiation, but it has an intensity that is at least 3 orders of magnitude larger than the intensity of the Raman side bands. The intensity of the Raman scatter is dependent on the derivative of the polarizability with respect to the molecular coordinate $(d\alpha/dq_v)_0$ from equation II-16. This factor is also very important because if the polarizability does not change during the nuclear displacement of a given vibration, then no Raman scattering will be observed for this particular vibration. Classical

theory predicts that the anti-Stokes scatter will also be more intense than Stokes scatter due to the wavelength dependence of the scatter.²⁶ However, this prediction is wrong. The Stokes scatter is much more intense than the anti-Stokes scatter experimentally. This failure in predicting the intensity of the different forms of the scatter results in the need for another model that can correctly predict the experimental outcomes.

Quantum-Mechanical Theory of Light Scattering from Molecules

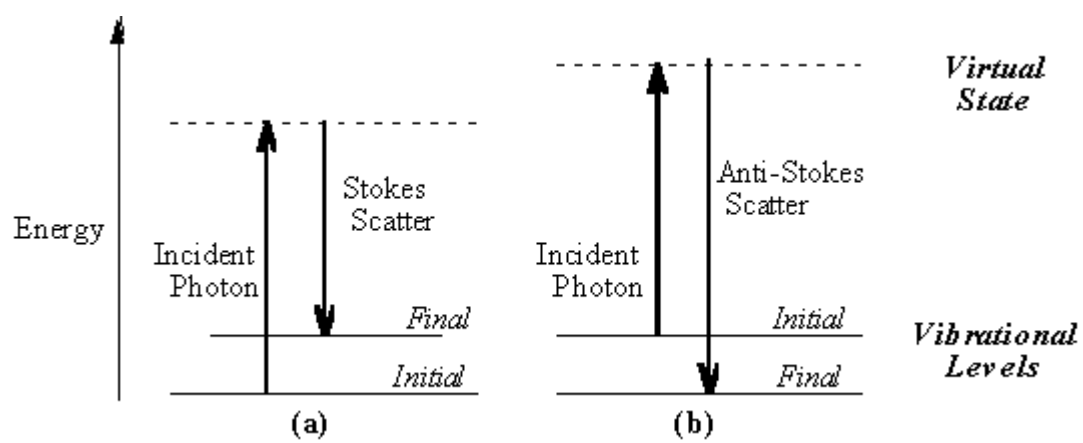
In quantum mechanics, a molecular motion may only exist in certain discrete energy states. A change in the state occurs by either gaining or losing one or more quanta of energy. This is defined by $E=h\nu_v$ where h is Planck's constant and ν_v is the classical frequency of a molecular motion. The interaction between electromagnetic radiation and a molecule may be classified as an energy-transfer mechanism. The absorption process illustrates the simplest example of this behavior. In absorption, a molecule will have a gain in quantum energy, accompanied by the annihilation of a quantum of light.

In light scattering processes, incident radiation with energy equal to $E=h\nu_0$ will strike the molecule causing a momentary excitation to what is referred to as a *virtual state*. This momentary interaction of the light and matter involves at least two quanta of energy acting simultaneously in this system.²³ In elastic scattering, a quantum of energy is created at the same time that an identical quantum of energy is annihilated. This leaves the molecule unchanged by the interaction and the elastic scatter thus exists at the same frequency as the incoming radiation. In inelastic scattering processes, the two photons created are not identical and a net energy change in the molecule has occurred. In Stokes-Raman ($\nu_0 - \nu_v$) scattering, a molecule may acquire a quantum of vibrational energy from the incoming light resulting in scattering that is less energetic than the original radiation by an amount that is exactly equal to the energy required

for excitation of a particular vibrational mode, ν_v . This is schematically shown in Figure II-4. For anti-Stokes scatter, the created photon is more energetic than the incoming radiation. The ability of a vibrational mode to generate Raman scattering depends on the extent to which the vibrational mode is able to generate a change in the polarizability of the molecule. The polarizability tensor may be used to calculate the magnitude of the oscillating dipole when it oscillates at the same frequency as the Rayleigh scatter. However, if a molecule changes states based on the interaction with the radiation, the changes in the polarizability tensor may be calculated and the new Raman scatter from the induced dipole may be observed. The maximum induced dipole at these particular frequencies is calculated using the perturbation theory. The results agree well with the predictions obtained from the Classical theory. The perturbation theory does an excellent job in predicting the induced oscillating dipoles, but is not practical in estimating absolute scattering intensities. Placzek's semi-classical polarizability theory is much more practical for these calculations. A thorough explanation of this theory may be found in the literature.²⁶

The primary point that should be understood from the quantum-mechanical model is that when light interacts with molecules, Raman scattering is produced from a transition between two states of the molecule. Since vibrational states are quantized, the scattered photon carries off the difference in vibrational energy states for the molecule and is observed as a shift from the frequency of the incident radiation. Classical theory predicts that Stokes and anti-Stokes scatter are equally probably. However, the quantum-mechanical model explains that anti-Stokes scatter is not possible if the molecule exists in the lowest vibrational state ($m^v=0$). From the Boltzmann distribution equation, it is evident that the majority of the molecules will exist in the lowest vibrational state at room temperature. Therefore, Stokes scatter is the favored process for

Figure II-4. Raman Energy Level Diagram. (a) Stokes Raman scattering (b) anti-Stokes Raman scattering.



scattered radiation as compared to anti-Stokes. This leads to the fact that the Stokes radiation is stronger in intensity than the anti-Stokes scatter, which is a correct prediction based on experimental results.

Raman vs. IR

Through discussion in previous sections, the differences and similarities should be fairly obvious to the reader. However, due to the importance of the material, a brief review will be undertaken. The fundamental difference between these two spectroscopic techniques lies within the mechanism that governs each. Raman activity is based on a change in polarizability of a molecule, while IR activity is based on a net change in the dipole moment of a molecule. The symmetry for a given molecule will determine whether a vibration will be IR-active, Raman active, or active in both.

Raman tends to be more sensitive for stretching vibrations such as $C\equiv C$, $C=C$, $C-C$, $S-S$, and $C-S$ bonds. IR is a more sensitive technique for vibrations such as $O-H$ and $N-H$. In general terms, IR is most sensitive to ionic bonds while Raman is most sensitive to bonds that are more covalent in nature.²⁴ It is because of these differences that Raman and IR should be recognized as complementary techniques and both used in order to elucidate vibrational information from a particular system.

Raman makes use of the visible wavelength region for experiments and this is an important advantage over IR. The use of the visible region allows for the easier sampling of materials. Substrates such as glass, Pyrex, or metal oxides that cannot be used in IR due to their strong absorption are used commonly in Raman experiments. An additional advantage of operating in the visible region is the spectral acquisition window. The region of $4000-50\text{ cm}^{-1}$

may be acquired in a single scan in typical Raman systems while the same coverage in an IR experiment would require a change of beamsplitter, filters, or detectors.

Another significant advantage offered by Raman is the ability to study aqueous samples because water is a weak Raman scatterer. The vibrations of water are very-IR active tend to either completely mask or at the least, interfere with the vibrational bands from the analyte of interest. Raman also has the ability to study compounds that are hygroscopic or air-sensitive by analyzing these systems through glass containers.

However, for all these advantages, Raman does have significant disadvantages compared to IR. The primary disadvantage is that Raman scattering is a very weak phenomenon, only 1 in 1,000,000 photons is Raman active. This means that IR absorption is nearly nine times more probable than the Raman effect. This is the major reason for the limited number of applications for Raman in thin films although this is slowly changing as technology advances.^{7, 23-26} In addition, to facilitate quantitative measurements in Raman, it is often helpful to have an internal reference as discussed in Chapter III of this work to aid in quantitation due to intensity differences run-to-run.

One other notable problem associated with the weakness of Raman scattering is that of fluorescence. The powerful lasers used to produce the Raman scatter may induce fluorescence in the sample, which can completely obscure bands of interest in much the same way that bulk water interferes with IR measurements. The laser may also cause localized heating or photodecomposition of the sample, which is also undesirable in most cases. The problems associated with fluorescence have been overcome to some extent by the use of near IR lasers as excitation sources. Raman is also at a disadvantage when it comes to obtaining rotational spectra

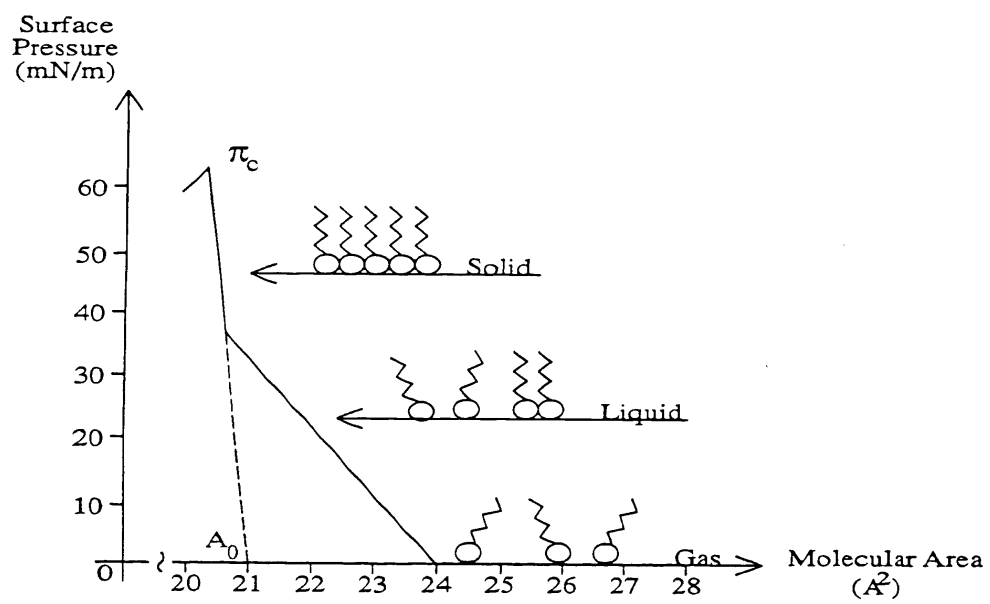
when compared to IR due to the problems with having high resolving power in the visible region.

Langmuir Films

A Langmuir film is a one-molecule thick monolayer of amphiphilic water insoluble molecules located at the air/water (A/W) interface. The characteristics of monomolecular films on water were observed by Gaius Plinius Secundus or as he is better known, Pliny the Elder, and Plutarch two thousand years ago.²⁷ Benjamin Franklin noted the calming effect that a teaspoon of oil had on a half-acre pond in 1774.²⁸ However, it was not until Agnes Pockels performed her work in 1882 that a true understanding, with reproducible measurements, existed. Miss Pockels performed much of her work in her kitchen using bowls to contain water, serving as an early Langmuir trough. She used a button as a rudimentary film balance and measure changes in surface tension after the addition of a film to the water surface. She communicated her finding to Lord Rayleigh (John William Strutt) who had published work similar to her own the previous year²⁹, and he aided her in having the results published in *Nature*.³⁰

Miss Pockels introduced many of the basic concepts of amphiphilic monolayers, including the use of a spreading solvent to deliver a small quantity of material rapidly and accurately to the surface, and her isotherm of a stearic acid monolayer is now recognized to be essentially correct (a representation is shown in Figure II-5). Lord Rayleigh was inspired by this contact to continue his own experiments, from which he concluded that these layers were a single molecule thick.³¹ Monomolecular films at the A/W interface received little further attention until 1917 when Irving Langmuir performed his pioneering work on the films that today bear his name. Langmuir developed a film balance, which also bears his name, that is used

Figure II-5. A pressure-area (π -A) isotherm of stearic acid



for the measurement of surface pressures of monomolecular films.^{32,33} With this work, he was able to show that the limiting molecular surface area of different chain length fatty acids on the surface of water was equal to 2100 nm². This helped prove that these amphiphilic, rod-like molecules were oriented vertically at the A/W interface. One of the most useful and studied properties of Langmuir films is surface pressure. The deposition of organic films on a water surface lowers the surface tension of the water. As a result, a surface pressure will result from the formation of the monomolecular film at the A/W interface. This pressure, π , is defined as:

$$\pi = \gamma_0 - \gamma \quad (\text{II-17})$$

where γ_0 is the surface tension of the pure subphase, γ is the surface tension of the surface containing the monolayer film, and π is a two-dimensional pressure with units of mN/m. Through the use of moveable barriers on the trough, the surface pressure can be altered by expanding or reducing the surface area that contains the film. If the surface pressure of the monomolecular film is plotted against the changing molecular area, a pressure-area (π -A) isotherm may be obtained. This isotherm gives detailed information regarding the physical state of the molecules on the surface of the subphase.

Of the numerous techniques available for measuring surface pressure, the most effective is the Wilhelmy technique. Ludwig Wilhelmy developed the technique that bears his name in 1863.³⁴ The Wilhelmy technique utilizes a thin plate (usually made from filter paper) suspended from a microbalance in such a way that the plate just penetrates the surface of the subphase. A greater downward pressure is exerted on the plate by the pure subphase than when a film is present on top of the subphase. A change in surface pressure, $\Delta\pi$, is a function of the change in pull that the microbalance detects times the perimeter of the plate. A representative π -A isotherm of stearic acid spread at the A/W interface is illustrated in figure II-5. Several distinct regions of

differing compressibility are observed and labeled in the figure. The regions include a gas (G) phase, a liquid (L) phase, and a solid (S) phase. These physical states are two-dimensional analogues of the bulk gas, liquid, and solid phases.

Self-Assembled Monolayers

Monolayer film assemblies that are spontaneously formed by the immersion of an appropriate substrate into a solution of active amphiphile dissolved in an organic solvent are referred to as self-assembled monolayers or SAMs.^{7, 35} Although organic films of organosilicon on hydroxylated surfaces^{36, 37} and alkanethiols on metal surfaces are the most common SAM systems found in the literature, SAMs such as those found in membrane supported films are more relevant to the work found in this manuscript.³⁸ SAMs are much more stable and uniform than other monolayer techniques such as Langmuir-Blodgett transfers due to the strong chemisorption of the headgroup of the amphiphile to the substrate surface.⁷

By examining the different moieties that comprise the adsorbate, the highly ordered assembly of these molecules may be understood. The first moiety is the headgroup that provides the strongest interaction with the surface and is the reason self-assembly occurs. The chemisorption to the surface results in the pinning of the headgroup to a specific site on the surface through a chemical bond. In the examples cited above, the chemisorption to the surface is achieved through the covalent Si-O bond of the organosilanes on the hydroxylated surface and through the covalent but slightly polar Au-S bond for alkanethiols. The energies associated with the chemical bonds formed between the headgroups and these surfaces are on the order of tens of kcal/mol.³⁵ Consequentially, these strong interactions result in the adsorbate molecules occupying every potential binding site on the surface, which in turn forces these films to pack together into a high degree of order.

The second moiety to be considered is the alkyl chains of these molecules. Due to van der Waals attractive forces, the chains from neighboring molecules will exhibit interchain interactions. This interaction is secondary to the chemisorption of the headgroup and is less than 10 kcal/mol.³⁵ The terminal groups are the final moiety to consider, Depending on the functional group, different packing arrangements may be achieved for the SAMs. Selection of the terminal group becomes important if a given surface activity is required.^{39, 40} An example of this would be the choice of deposition with the poly-l-lysine and alginate layers in the membrane mimetic film discussed in chapter three of this work.

Photo-initiated Polymerization

Polymerization, as defined by Merriam-Webster dictionary, is a chemical reaction in which two or more molecules combine to form larger molecules that contain repeating structural units. More precisely, it is a process where subunits, monomers, are joined together to create a larger compound or polymer. There are several reaction pathways to achieve polymerization. However, for the work presented in this manuscript, we will concentrate on photochemically initiated polymerizations and in particular, anionic photoinitiated polymerizations.

Photoinduced polymerization encompasses the chemical and physical reactions of organic-based materials that are initiated by the application of electromagnetic radiation. The current and future importance of photoinitiated polymerization is matched only by its rapid expansion in recent years. Advances in this technique are being driven by its rapid adoption in industrial applications where it is generally referred to as UV curing. Its uses encompass both high-volume applications such as coatings, adhesives, and printing inks as well as advanced high technology uses such as microelectronic encapsulation, photo and stereolithography, and holographic data storage media.⁴¹ The primary advantage in using photoinitiated polymerization

is the high rate of reaction that may be achieved under intense radiation. This allows the phase change from liquid to solid to take place in less than 1 second.^{42, 43} A second important feature of light-induced initiation is that polymerization occurs only in illuminated areas, therefore allowing the generation of high resolution images for the production of printing plates, optical discs and microcircuits.^{44, 45} Most recently, its applications have covered three-dimensional stereolithography and holographic recording.⁴⁶

One of the basic laws in photochemistry states that a photochemical reaction can only occur if light has been absorbed by the medium. As most monomers are essentially transparent to the radiations emitted by conventional UV sources, usually mercury lamps, they do not produce initiating species with sufficiently high yields. Therefore, it is necessary to introduce in the UV-curable formulation a photoinitiator, which will effectively absorb the incident light and generate reactive free radicals or ions by cleavage of the electronically excited states. The photoinitiator plays a key role in that it governs both the rate of initiation and the depth of cure through its absorbance. Due to its importance, new initiators are constantly being examined. The information presented in Chapter IV of this manuscript details the use of classical metallocenes as photoinitiators in anionic polymerization.¹⁹ In this work, we have utilized real-time FTIR analysis to monitor the kinetics of the reaction as reported previously.^{20, 21}

REFERENCES

1. Bubert, H. and Jenett, H., eds. *Surface and Thin Film Analysis*. 2002, Wiley-VCH: Weinheim.
2. Czanderna, A.W., *Methods of Surface Analysis*. 1975, Amsterdam: Elsevier.
3. Kane, P.F. and Larabee, G.B., *Characterization of Solid Surfaces*. 1974, New York: Plenum.
4. Feuerbacher, B., et al., *Photo-Emission and Electronic Properties of Surfaces*. 1978, New York: Wiley.
5. Ibach, H., *Electron Spectroscopy for Surface Analysis*. 1977, Berlin: Springer.
6. Wolfram, T., *Inelastic Electron Tunneling Spectroscopy*. 1978, Berlin: Springer.
7. Ulman, A. and Fitzpatrick, L.E., eds. *Characterization of Organic Thin Films*. Materials Characterization Series, ed. C.R. Brundle and J. Charles A. Evans. 1995, Butterworth-Heineman: Boston.
8. Binnig, G., et al., *Surface Studies by Scanning Tunneling Microscopy*. Physical Review Letters, **1982**. 49(1): 57-61.
9. Binnig, G., et al., *Atomic Force Microscope*. Physical Review Letters, **1986**. 56(9): 930-33.
10. Latyshev, A.V., et al., *Transformations on Clean Si(111) Stepped Surface During Sublimation*. Surface Science, **1989**. 213(1): 157-69.
11. Rohrer, H., *Scanning Tunneling Microscopy: A Surface Science Tool and Beyond*. Surface Science, **1994**. 299-300: 956-64.

12. Dluhy, R.A., et al., *Vibrational Spectroscopy of Biophysical Monolayers - Applications of Ir and Raman-Spectroscopy to Biomembrane Model Systems at Interfaces*. Spectrochimica Acta Part A, **1995**. 51(8): 1413-47.
13. Leverette, C.L. and Dluhy, R.A., *A Novel Fiber-Optic Interface for Unenhanced External Reflection Raman Spectroscopy of Supported Monolayers*. Langmuir, **2000**. 16(8): 3977-83.
14. Leverette, C.L., et al., *Development of a Novel Dual-Layer Thick Ag Substrate for Surface-Enhanced Raman Scattering (Sers) of Self-Assembled Monolayers*. Journal of Physical Chemistry B, **2002**. 106(34): 8747-55.
15. Griffiths, P.R. and Haseth, J.A.d., *Ft-Ir Spectroscopy*, in *Ft-Ir Spectroscopy*. 1986, Wiley: New York. p. 656.
16. Fadini, A. and Schnepel, F.-M., *Vibrational Spectroscopy: Methods & Applications*. English ed. Ellis Horwood Series in Analytical Chemistry, ed. E. Horwood. 1989, New York: Halstead Press. 205.
17. Ingle, J.D. and Crouch, S.R., *Spectrochemical Analysis*. 1st ed. 1988, New York: Prentice Hall. 608.
18. Kauppinen, J.K. and Hollberg, M.R., *Infrared Spectrometers*, in *Encyclopedia of Applied Physics*, G.L. Trigg, et al., Editors. 1997, John Wiley & Sons: New York. p. 265-87.
19. Sanderson, C.T., et al., *Classical Metallocenes as Photoinitiators for the Anionic Polymerization of an Alkyl 2-Cyanoacrylate*. Macromolecules, **2002**. 35(26): 9648-52.
20. Yang, D.B., *Kinetic-Studies of Photopolymerization Using Real-Time Ft-Ir Spectroscopy*. J. Polym. Sci. Pol. Chem., **1993**. 31(1): 199-208.

21. Decker, C. and Moussa, K., *A New Method for Monitoring Ultra-Fast Photopolymerizations by Real-Time Infrared (Rtir) Spectroscopy*. MAKROMOLEKULARE CHEMIE, **1988**. 189(10): 2381-94.
22. Harrick, N.J., *Internal Reflection Spectroscopy*. 1967, New York: John Wiley & Sons, Inc. 327.
23. Turrell, G. and Corset, J., *Raman Microscopy: Developments and Applications*. 1996, London: Academic Press.
24. Nakamoto, K. and Ferraro, J.R., *Introductory Raman Spectroscopy*. 1994, San Diego: Academic Press.
25. Lewis, I.R. and Edwards, H.G.M., *Handbook of Raman Spectroscopy: From the Research Laboratory to the Process Line*. Practical Spectroscopy, ed. I.R. Lewis and H.G.M. Edwards. Vol. 28. 2001, New York: Marcel-Dekker, Inc.
26. Laserna, J.J., *Modern Techniques in Raman Spectroscopy*. 1996, Chichester: John Wiley and Sons.
27. Secundus, G.P., *Natural History*. 77.
28. Franklin, B., *Of the Stilling of Waves by Means of Oil*. Philosophical Transactions, **1774**. 64: 445-60.
29. Rayleigh, L., Proc. Roy. Soc., **1890**. 47: 364.
30. Pockels, A., *Surface Tension*. Nature, **1891**. 43: 437.
31. Rayleigh, L., Phil. Mag., **1899**. 48: 337.
32. Langmuir, I., *The Constitution and Fundamental Properties of Solids and Liquids. Ii. Liquids*. Journal of the American Chemical Society, **1917**. 39(9): 1848-906.
33. Langmuir, I., *Two-Dimensional Gases Liquids and Solids*. Science, **1936**. 84(2183): 379-83.

34. Wilhelmy, L.F., *Annalen der Physik und Chemie*, **1863**. 119: 177.
35. Ulman, A., *An Introduction to Organic Thin Films from Langmuir-Blodgett to Self-Assembly*. 1991, San Diego: Academic Press.
36. Maoz, R. and Sagiv, J., *Penetration-Controlled Reactions in Organized Monolayer Assemblies. 2. Aqueous Permanganate Interaction with Self-Assembling Monolayers of Long-Chain Surfactants*. *Langmuir*, **1987**. 3(6): 1045-51.
37. Sagiv, J., *Organized Monolayers by Adsorption. 1. Formation and Structure of Oleophobic Mixed Monolayers on Solid Surfaces*. *Journal of the American Chemical Society*, **1980**. 102(1): 92-98.
38. Murphy, M.R., et al., *Analysis of Photo-Initiated Polymerization in a Membrane Mimetic Film Using Raman Microscopy and Fourier Transform Infrared Spectroscopy*. Submitted to *Langmuir*, **2004**: Chapter III of dissertation.
39. Marra, K.G., et al., *Cytomimetic Biomaterials .I. In-Situ Polymerization of Phospholipids on an Alkylated Surface*. *Macromolecules*, **1997**. 30(21): 6483-88.
40. Winger, T.M., et al., *Formation and Stability of Complex Membrane-Mimetic Monolayers on Solid Supports*. *Langmuir*, **1999**. 15(11): 3866-74.
41. Belfield, K.D. and Crivello, J.V., eds. *Photoinitiated Polymerization*. *Acs Symposium Series*. 2003, Oxford University Press: Washington D.C.
42. Decker, C., *The Use of Irradiation in Uv Polymerization*. *Polymer International*, **1998**. 45(2): 133-41.
43. Decker, C., *Photoinitiated Crosslinking Polymerisation*. *Progress in Polymer Science*, **1996**. 21(4): 593-650.

44. Buhler, N. and Bellus, D., *Photopolymers as a Powerful Tool in Modern Technology*. PURE AND APPLIED CHEMISTRY, **1995**. 67(1): 25-31.
45. Andrzejewska, E., *Photopolymerization Kinetics of Multifunctional Monomers*. Progress in Polymer Science, **2001**. 26(4): 605-65.
46. Cumpston, B., et al., *Two-Photon Polymerization Initiators for Three-Dimensional Optical Data Storage and Microfabrication*. Nature, **1999**. 398(6722): 51-54.

CHAPTER III

**ANALYSIS OF PHOTO-INITIATED POLYMERIZATION IN A MEMBRANE
MIMETIC FILM USING RAMAN MICROSCOPY AND FOURIER TRANSFORM
INFRARED SPECTROSCOPY¹**

¹ Murphy, M. R.; Faucher, K. M.; Chaikof, E. L.; and Dluhy, R. A. submitted to *Langmuir*

ABSTRACT

A stable, substrate-supported phospholipid film created by in-situ photopolymerization was investigated with Raman microscopy and Fourier Transform Infrared spectroscopy. The lipid film was manufactured on a polyelectrolyte multilayer by in-situ photopolymerization of an acrylate functionalized phospholipid assembly, at a solid-liquid interface. Photopolymerization was carried out by white light and 514.5nm wavelength irradiation from an Argon ion continuous wave laser. Ratios of the integrated area of the C=C vibration to the ester carbonyl vibration from FTIR measurements were used to quantitate the degree cure and thus the amount of cross-linking occurring for a given period of irradiation. Although this is the accepted method for this type of analysis, we have proven that Raman Microscopy offers a significant advantage for this analysis in this system. This is due to Raman being a more sensitive technique for the analysis of stretching vibrations such as the C=C stretch than IR because of the mechanism on which each is based. Raman also offers the advantage of being able to analyze samples with higher water content since water is a weak Raman scatterer eliminating the problem of water masking the region of interest in the IR. Ratios of the integrated areas of the C=C and C-N vibrations collected via Raman microscopy were compared with those taken by FT-IR. The two measurements agreed very closely verifying the use of Raman microscopy as a legitimate measurement tool for this type of analysis. Further advancements were made by the use of 514.5nm wavelength light for irradiation. This greatly reduced irradiation times and eliminated several problems that had existed previously including sample drying and heating from prolonged irradiation times by the white light source.

INTRODUCTION

By incorporating physiologically relevant antithrombogenic mechanisms at the blood-material interface it is believed that a clinically viable artificial blood vessel may be constructed. For nearly two decades, investigators have noted that the phosphorylcholine headgroup seems to limit the induction of blood clot formation on synthetic surfaces.¹⁻³ Given this, there has been considerable interest in the use of supported lipid membranes for potential applications such as sensors or biofunctional coatings for artificial organs and other implanted medical devices.^{4, 5} The development of such devices holds particular significance to the fields of cardiac, plastic, and vascular surgery. Additional areas that could see enormous benefits from the development of these types of molecularly engineered surfaces are artificial organ and metabolic support systems implantation. The supported lipid membranes to be used for these coatings may be constructed by assembling a layer of closely packed hydrocarbon chains onto an underlying substrate followed by controlled dipping through an organic amphiphilic monolayer at an air-water interface or by exposure to a dilute solution of emulsified lipids or unilamellar vesicles.⁴ However, a significant barrier to the development of such a device has been limited stability outside of a laboratory environment.

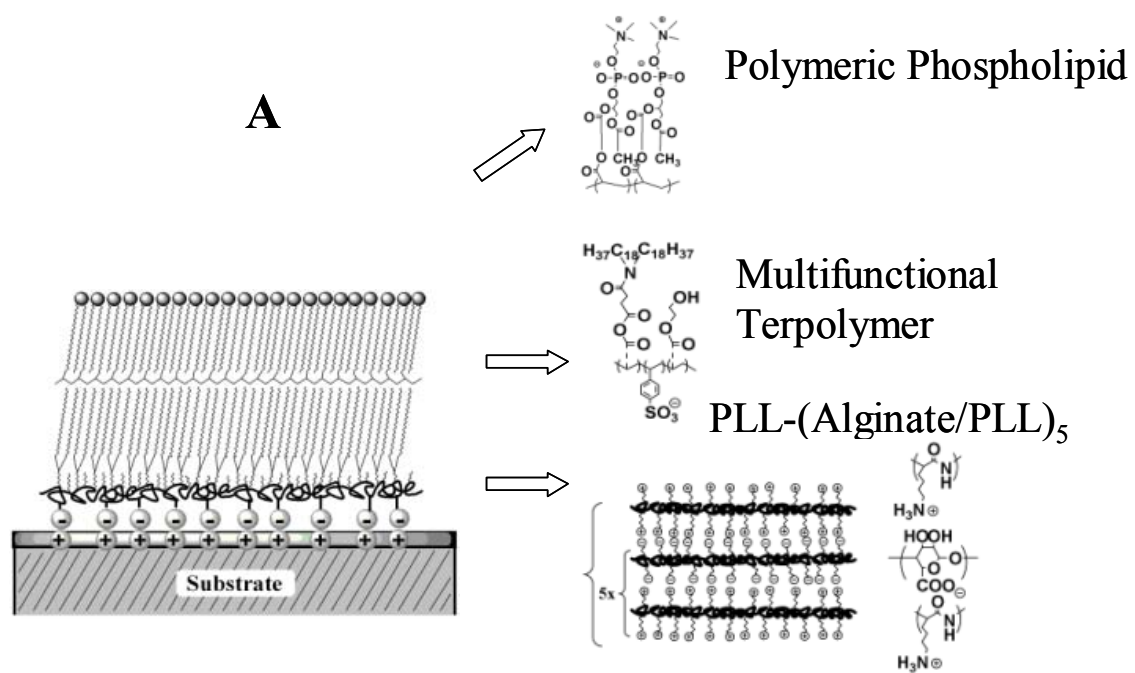
Noncovalently associated planar lipid assemblies, in and of themselves, are insufficiently robust for medical implant applications.⁶⁻⁸ One method that has been examined to increase membrane stability is *in-situ* photopolymerization of a planar lipid assembly at a liquid-solid interface. Photoinitiated polymerization has been shown to be preferential to heat initiated polymerization due to significant lipopeptide loss as the phase transition temperature is approached. The *in-situ* photopolymerization of these types of systems is initiated independent of

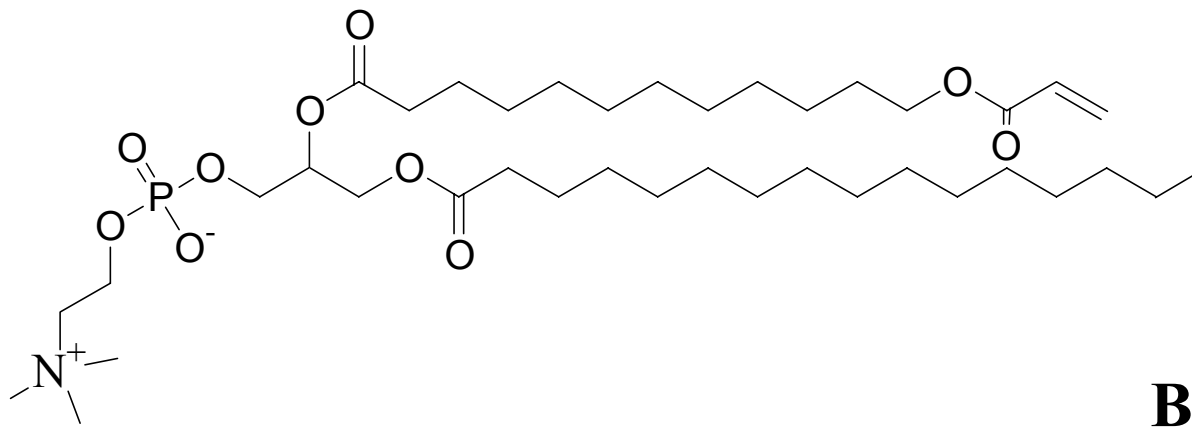
polymerization temperature, which allows the majority of lipopeptide to be available for cross-linking resulting in substantial increase in membrane stability.

It is believed that the formation of a stabilized lipid membrane on a polyelectrolyte multi-layer (PEM) will greatly enhance the versatility of the system by offering an additional mechanism for modulating both the surface physiochemical properties and the biological activity of the film. Recently, polyelectrolyte multilayers have been studied as bioinert films to reduce cell and protein adhesion. This work, conducted by Liu *et al*⁹ describes a new approach for generating a robust, membrane-mimetic coating on a polyelectrolyte monolayer. Their design utilizes an amphiphilic polymer with anionic surface anchoring groups. This provides a convenient means for alkylation with an intervening polymer cushion, this is illustrated in Figure III-1 and Figure III-2. After the formation of the mono-acrylated lipid assembly, photoinitiated polymerization was performed to stabilize the membrane. In-situ polymerization of phospholipids has also been carried out successfully on self-assembled monolayers of octadecyl trichlorosilane on glass,^{5, 10} octadecyl mercaptan bound to gold¹¹, as well as on an amphiphilic polymer cushion.¹²

A great deal of effort has been made to fully characterize supported lipid membranes. Much of this effort has focused on determination of layer thickness and coverage of the substrate. A question of considerable importance concerns the robustness of the PEM and stability of the lipid coating. A large number of instrumental analyses have been performed on the system to answer these questions. Some of the techniques utilized include: ellipsometry, high-resolution scanning electron microscopy, ¹H and ¹³C NMR, size exclusion chromatography, contact angle measurements, ESCA, FT-IR, and Fluorescence microscopy. One measurement that is believed to be a good indicator of long-term stability is the percent polymerization that

Figure III-1. (A). Membrane-Mimetic Film. Polymeric Phospholipid Monolayer Supported by a Polyelectrolyte Multi-layer and Hydrated Cushion (B). Monoacrylate-PC Structure.

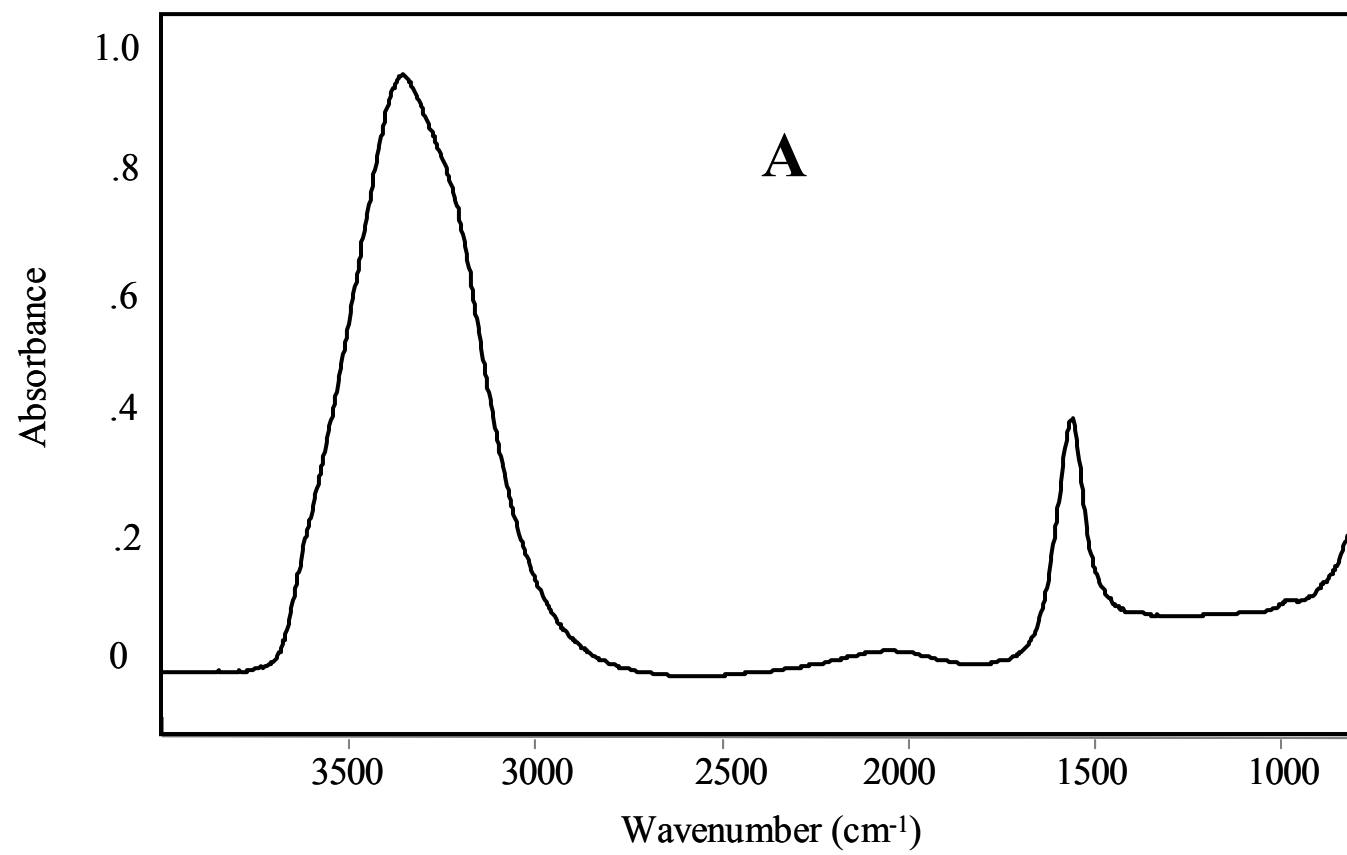


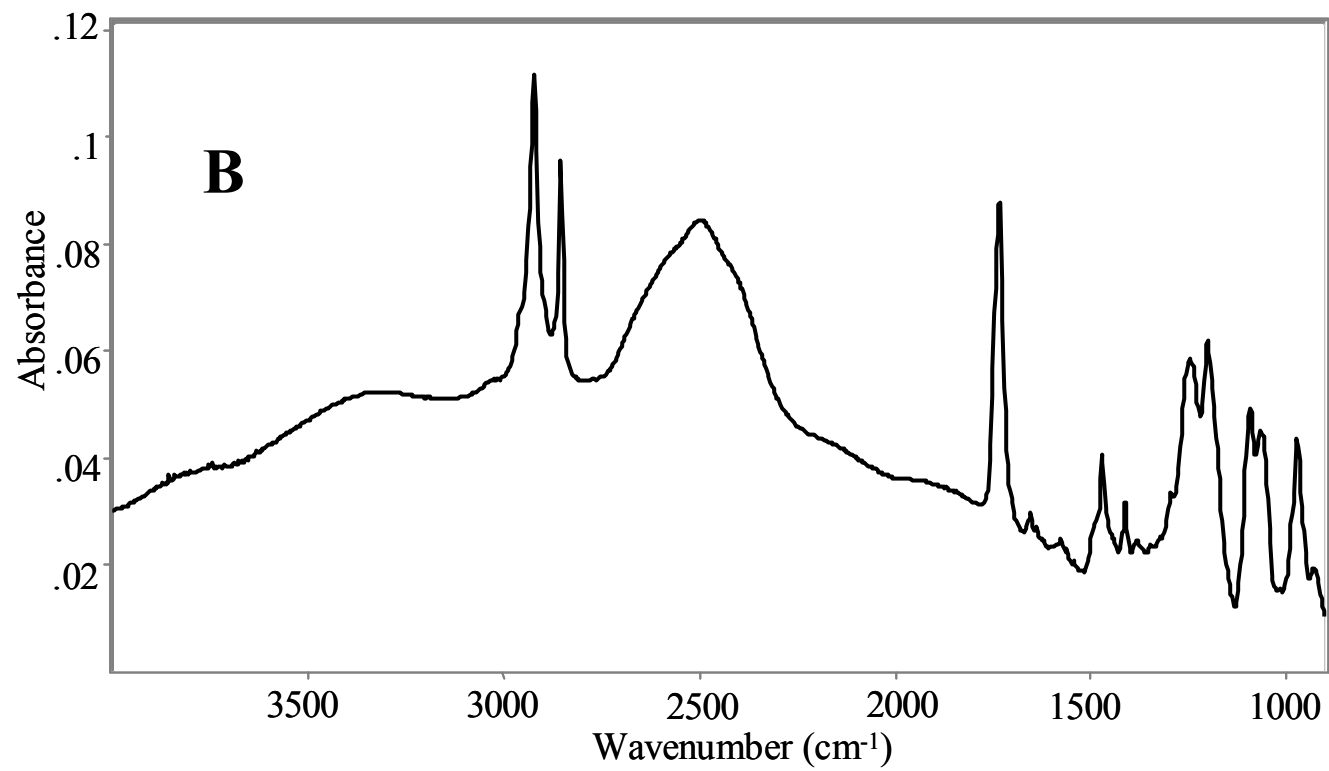


Acrylate-PC

1-palmitoyl-2-[1,2-(acryloyloxy)dodecyl]-sn-glycero-3-phosphocholine

Figure III-2. (A). FT-IR Spectrum of 12mM Monoacrylate-PC. Spectrum illustrates the effects of bulk water in the sample. The C=C and C=O bands are completely obscured. (B). FT-IR Spectrum of Deuterated 12mM Monoacrylate-PC. The shifted bulk water no longer interferes with analysis of the region in question.





occurs during the photopolymerization process. A simple method for determining the degree of cure or percent polymerization is by the ratio of the integrated area of the C=C stretch occurring at 1610 cm^{-1} and the integrated area of the ester carbonyl at 1765 cm^{-1} .

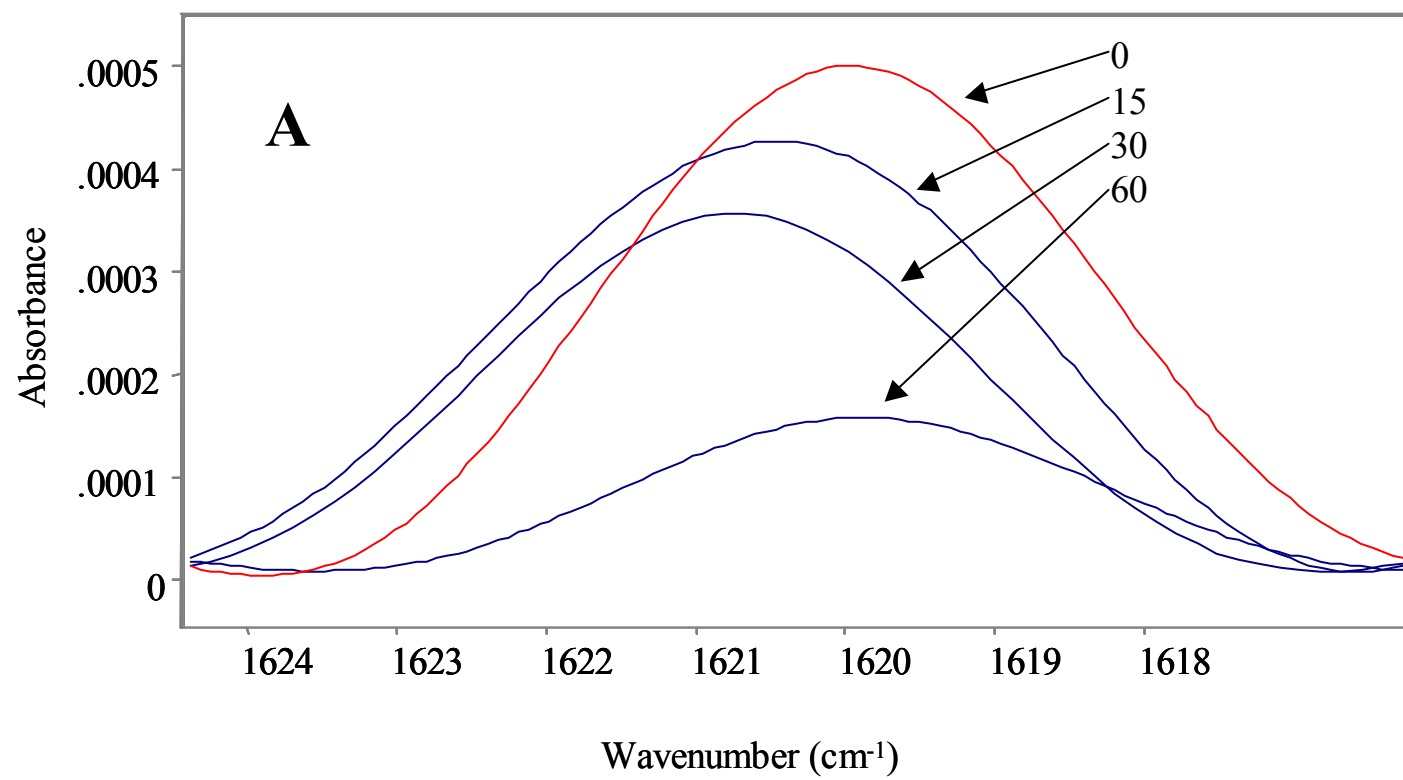
Due to the nature of the sample and the vibrations of interest in particular, Raman spectroscopy offers several advantages over the established FT-IR methodology for this analysis. Raman activity is based on a change in polarizability of a molecule, whereas IR activity is based on a net change in the dipole moment of a molecule. Raman is therefore a much more sensitive technique for the analysis of stretching vibrations such as the C=C stretch that is used for the analysis of percent polymerization. Raman can also be used to study aqueous samples because water is a weak Raman scatterer. In the IR, the vibrations of water are very IR-active and mask or interfere with the vibrational bands of interest, as illustrated in Figure III-2a. For these reasons, we want to utilize Raman microscopy for the quantitation of photo-induced polymerization in the membrane mimetic films being studied. Similarly, the use of a minimally hydrated lipid solution prepared with deuterium oxide provided a shift in the bulk water bands allowing for further ease of analysis as shown in Figure III-3.

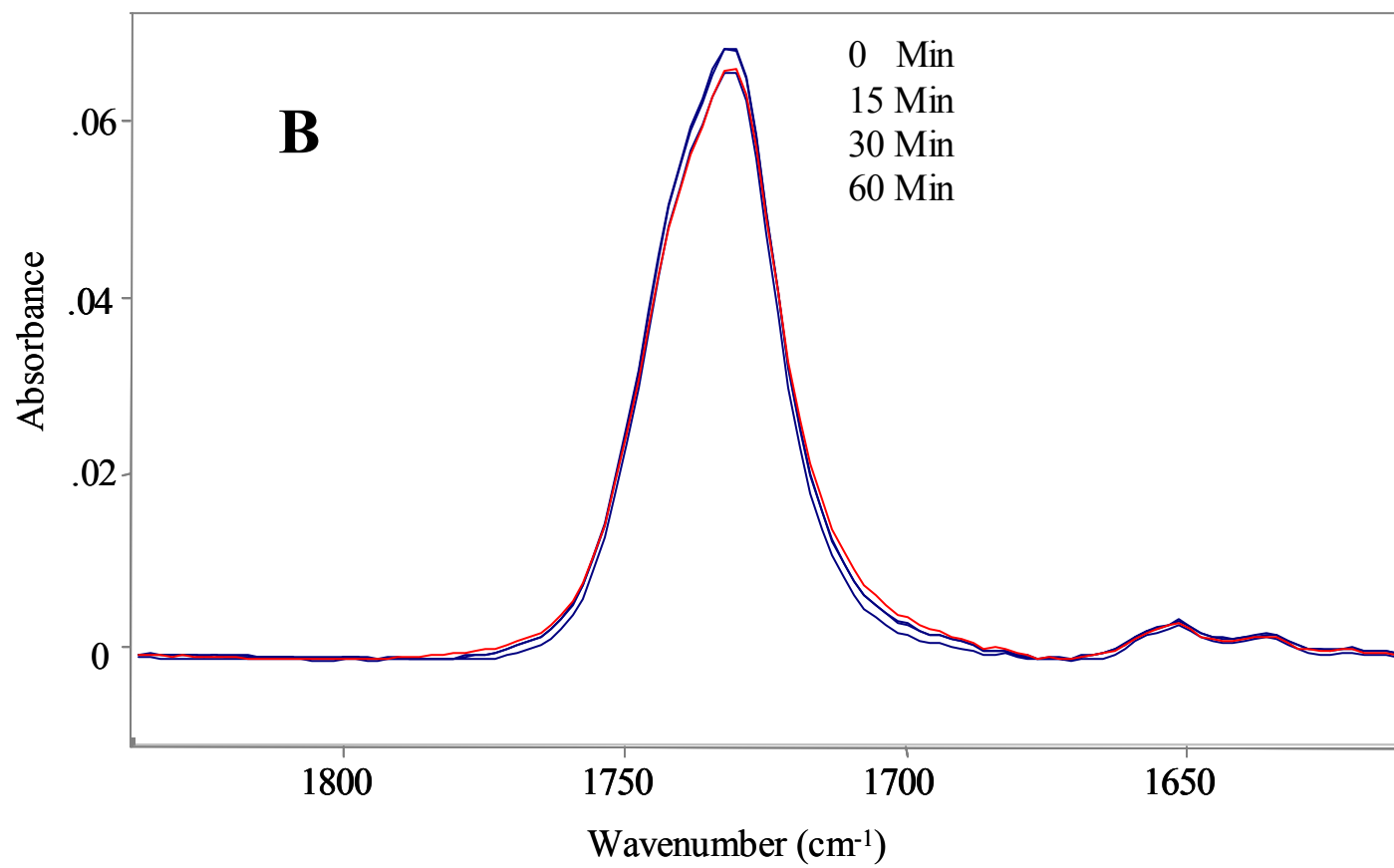
MATERIALS AND METHODS

REAGENTS. Deuterium oxide was obtained from Sigma Aldrich (St. Louis, Mo.). Monoacrylate-PC (1-palmitoyl-2-[1,2-(acryloyloxy)dodecanoyl]-*sn*-glycero-3-phosphocholine) (ARPC) and PTFE graft samples were provided by Emory University School of Medicine (Atlanta, Ga) and were synthesized as previously described.^{5,9}

INSTRUMENTATION. Irradiation. White light irradiation was carried out using a Dyna-Lite (Scientific Instruments, Inc., Skokie, IL) with an intensity of $\sim 10\text{ mW}$ at the sample. A Coherent

Figure III-3. (A). Decrease in C=C Band measured by HATR (B). Decrease in Ester Carbonyl Band measured by HATR





Innova 90 Series Ar⁺ laser (Coherent, Santa Clara, CA) provided excitation at 514.5 nm. Typical intensity for photoinitiation was ~ 100 mW at the sample. Light intensity was measured with a Coherent model 10 power meter (Coherent, Santa Clara, CA).

Infrared Spectroscopy. Spectra were acquired using a Digilab/BioRad FTS-60 Fourier Transform infrared (FT-IR) spectrometer (Randolf, MA) equipped with a narrow-band HgCdTe. Spectra were collected under the following conditions: 512 background scans, triangular apodization, and 4 cm⁻¹ resolution. Sample solutions of ARPC were placed on trapezoidal shaped ZnSe ATR crystals (Spectral Systems, Hopewell Junction, NY) in a horizontal attenuated total reflectance (HATR) accessory (CIC Photonics, Albuquerque, NM) for irradiation and analysis.

Raman Microscopy. Raman spectra were acquired using a Kaiser Optical Systems confocal Raman microscope (Kaiser Optical Systems, Incorporated, Ann Arbor, MI) equipped with a liquid nitrogen cooled charge coupled device (CCD) camera (Princeton Instruments, Trenton, NJ). The spectrograph used was a HoloSpec f/1.8-NIR spectrometer equipped with a HoloPlex grating that simultaneously measures the range of 100 to 3450 cm⁻¹ at an excitation wavelength of 785 nm. Spectra were collected with a 50x Carl Zeiss objective with 785nm illumination supplied by a Coherent Radiation 899 Ti:Sapphire Ring Laser (Coherent, Santa Clara, CA) pumped by a Coherent Radiation Innova 300 Series Ar⁺ laser (Coherent, Santa Clara, CA).

Software. All spectra were collected using software supplied by the manufacturer, for IR. Post processing of all collected spectra was conducted using *Grams32/AI* spectral software package (Galactic Industries (Nashua, NH). Center of gravity calculations were made using a Grams 32 based program written in our laboratory (R.A. Dluhy, unpublished). All spectra were baseline corrected for clarity. Spreadsheets and graphs were produced using Excel (Microsoft Corporation, Redmond, WA).

Preparation of ARPC for Photoinitiation. Monoacrylate-PC (1-palmitoyl-2-[1,2-(acryloyloxy)dodecanoyl]-sn-glycero-3-phosphocholine) (ARPC) samples were prepared for photopolymerization as a minimally hydrated lipid solution. A volume of 3.19×10^{-3} mL of deuterium oxide was added to 7.48mg of ARPC and heated to a temperature of 40 °C and then vortexed, in three cycles, to form multilamellar vesicles. The photoinitiator, consisting of 1 μ L of Eosin Y (EY), 225mM triethanolamine (TEA), and 37 mM VP in water, was added to the vesicle solution. This was placed on a 45-degree trapezoidal shaped germanium horizontal ATR crystal that was cleaned by sonicating for 15 minutes in a 6:3:1 mixture of chloroform, methanol, and water followed by a further 15 minutes in distilled deionized water.

Preparation of a Membrane-Mimetic Film on an ePTFE Graft. A gelatin base layer was coated to the luminal surface of an ePTFE graft to facilitate adhesion of the biomimetic film. A 6 % porcine gelatin solution was warmed to 37 °C in a water bath and impregnated in the graft by clamping one end of the graft and forcing 3 ml of the gelatin through the open end using a Luerlok syringe accomplished this. This process continued until Gelatin was visibly seen excreting from the pores on the sides of the graft. The protocol was repeated for the opposite end of the graft and the entire graft was then immersed in a gelatin bath for 2 hours at 42 °C to insure uniform coating.

Following the 2-hr incubation, the graft was oriented vertically to allow the excess gelatin to drain for 5 min. During this process, the graft was rotated by 180 degrees every 30 sec to allow the gelatin to congeal evenly. After the excess gelatin was removed, the graft was immersed in a 1.5 % v/v glutaraldehyde solution at room temperature for 16-18 hours to cross-link the gelatin for thermal and aqueous stability. When the cross-linking was completed, the graft was rinsed with 20 ml of DI water for 10 minutes at a 2 ml/min flow rate.

To coat the PLL and ALG polyelectrolyte layers, a 3 ml syringe containing 0.1 w/v % PLL solution was flowed through the graft using a syringe pump at a 1 ml/min flow rate for ~2 min. This was followed by rinsing with 10 ml of DI water at a 2 ml/min flow rate for 5 min. ALG was then coated on top of the PLL layer following the same procedure as the PLL coating except using a 0.15 w/v % ALG solution. 11 alternating PLL-ALG solutions were coated onto the ePTFE vascular graft with the final layer being PLL. The terpolymer was then coated onto the graft luminal surface using a 0.1 mM terpolymer solution (in 1 % DMSO/20 mM NaH₂PO₄, pH = 7.4) and pumped through the graft at a 0.1 ml/min flow rate for 10 min. Afterwards, the graft was rinsed with 10 ml of DI water at a 2 ml/min flow rate.

Acrylate-PC was prepared for the next coating layer using standard freeze-thaw and extrusion methods. The freeze-thaw was accomplished by heating the lipid in a 70 °C water bath and then freezing the lipid in liquid nitrogen with vortexing. The freeze-thaw procedure was repeated at least 3 times. After the freeze-thaw, the lipid was extruded 21 times through an Avanti Polar Lipids Mini Extruder (Alabaster, AL) using two, 2.0-micron polycarbonate membrane filters. The extrusion was then repeated using 0.6-micron polycarbonate membrane filters. Immediately following lipid extrusion, the lipid was diluted to 1.2 mM using 20 mM NaH₂PO₄, pH = 7.4 and 750 mM NaCl.

Next, the graft was placed into a custom designed graft rotator using Luer-Lok connectors and moved into a 43 °C incubator in a dark room. Photoinitiator (10 microliters per ml of lipid, 10 ml of lipid total) was added to the diluted lipid solution and aspirated into a 10 ml Luer-Lok syringe. The syringe was connected to a two-way stop-cock outside the graft rotator and 2.5 ml of lipid fusion solution was hand pumped into the assembly to fill the graft. The syringe was then placed in a syringe pump and set to a 1 ml/hr flow rate. Finally, the graft

rotator power supply was turned on and the graft assembly rotated at 50 rev/min for a period of 5 hours.

After the fusion, the graft rotator assembly was removed from the dark room and moved into a darkened workspace. The graft was removed from the rotator assembly and clamped vertically onto an optics table. A 360°, 1.6 cm side-firing probe with an SMA connector at one end (Romack Inc., Williamsburg, Va.) was attached to a 200 mW argon ion laser (Melles Griot, Carlsbad, Ca.). The fiber was inserted into the graft, with the top portion of the graft being irradiated for 5 minutes with an intensity of 50-75 mW/cm². The probe was then carefully moved down the graft and polymerization was performed in 1.6 cm sections until the entire graft is polymerized. The process requires 20 minutes for a 6 cm graft.

Following photopolymerization, the graft was placed into a syringe pump where 20 ml of DI water was flowed through the graft at a 2 ml/min flow rate. Following the rinsing step, a piece of the graft is cut for analysis before placing the remaining portion of the graft in rigid plastic tubing to maintain a straight shape during flow conditioning. The plastic tubing containing the graft is then placed in a re-circulating water bath flow loop at 37 °C for 24 hrs (150 ml/min, or a sheer rate of 500 s⁻¹).

RESULTS

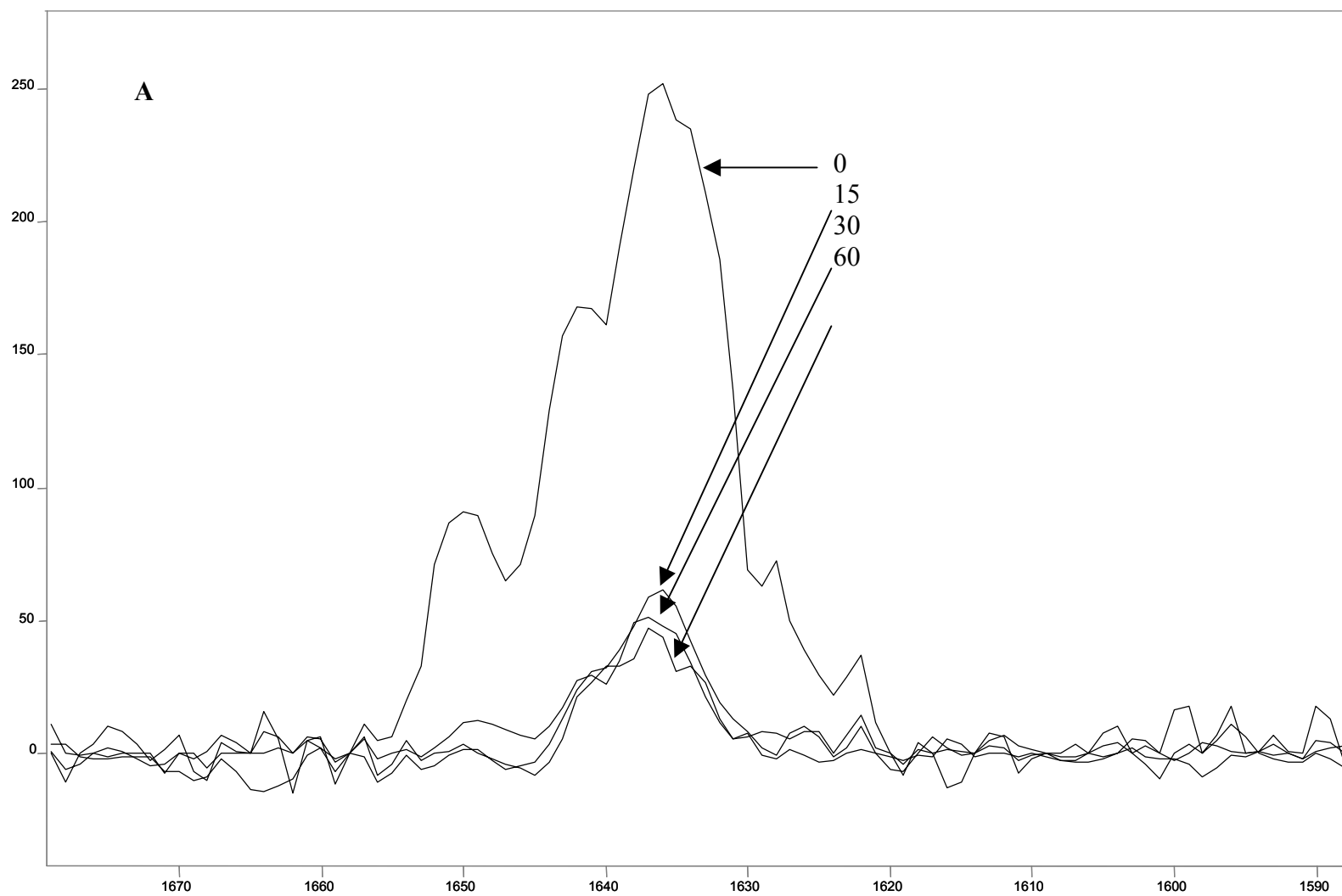
Quantitation of Photopolymerization in minimally hydrated lipid sample with white light irradiation by Infrared Spectroscopy. A spectrum of the lipid sample was taken prior to irradiation and is denoted as 0 minutes. The sample was then irradiated for times of 15, 30 and 60 minutes by a white light source at an intensity of ~ 60 mW at the sample. After each irradiation period, spectra were collected. The ratio of the integrated area of the C=C stretch at 1621 cm⁻¹ and the area of the ester carbonyl band centered at 1734 cm⁻¹ were measured for

changes during irradiation (Figure III-3a and III-3b). The ratio of the two bands corresponded to polymerization percentages of 0, 63, 77, and 86 for the respective irradiation periods. A detailed description of the analysis may be found in Appendix A.

Quantitation of Photopolymerization in minimally hydrated lipid sample with white light irradiation by Raman Microscopy. Incident irradiation for the Raman measurements was at 785 nm with approximately 60 mW of power at the sample position. A ratio of the integrated area of the C=C stretching vibration at 1638 cm^{-1} and the C-N stretch at 715 cm^{-1} was used for determining percent polymerization. The results compared favorably with those obtained from HATR FT-IR measurements. The raw C=C stretch data was normalized to the C-N band in order so that the visually observed decreases in the area of the C=C band correlate to the percent polymerization being reported (Figure III-4a). Normalizing the data against an internal standard provides a relative reference for intensity changes when comparing different data sets acquired on different days or different times. The intensity variations are common in Raman spectroscopy and the normalization of data allows for easy comparison of different data sets. More information on this procedure may be found in Appendix A. The C-N band that is used for normalization and to ratio the C=C stretch against is shown in Figure III-4b. It is important to remember that these changes may be substantial when compared to a band such as the C=C which may only have an intensity of 150 – 200 counts.

The polymerization percentages for the minimally hydrated lipid solution measured via Raman microscopy for 0, 15, 30, and 60 minute irradiation times were as follows: 0, 73, 77, and 86 percent polymerization for the respective irradiation times. The differences between the IR and Raman measurements varied according to data point with the greatest difference of 10% occurring at 15 minutes irradiation (Figure III-5). See Appendix A for detailed analysis.

Figure III-4. (A). Decrease in C=C Band measured by Raman Microscopy (B). C-N Stretch measured by Raman Microscopy



Counts / Raman Shift (cm-1)

Overlay Y-Zoom CURSOR

File # 1 : 1218D2O0

Res=None

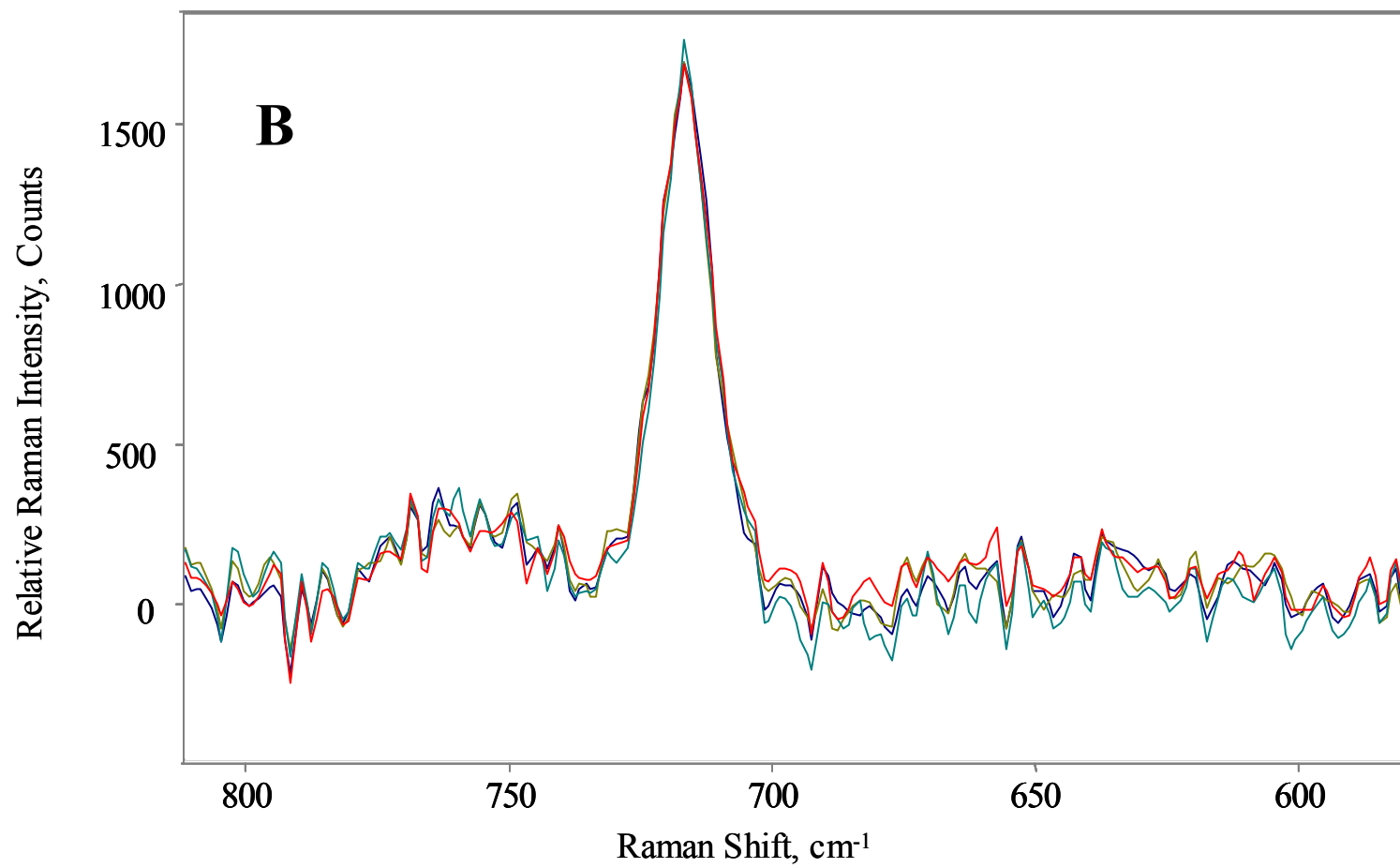
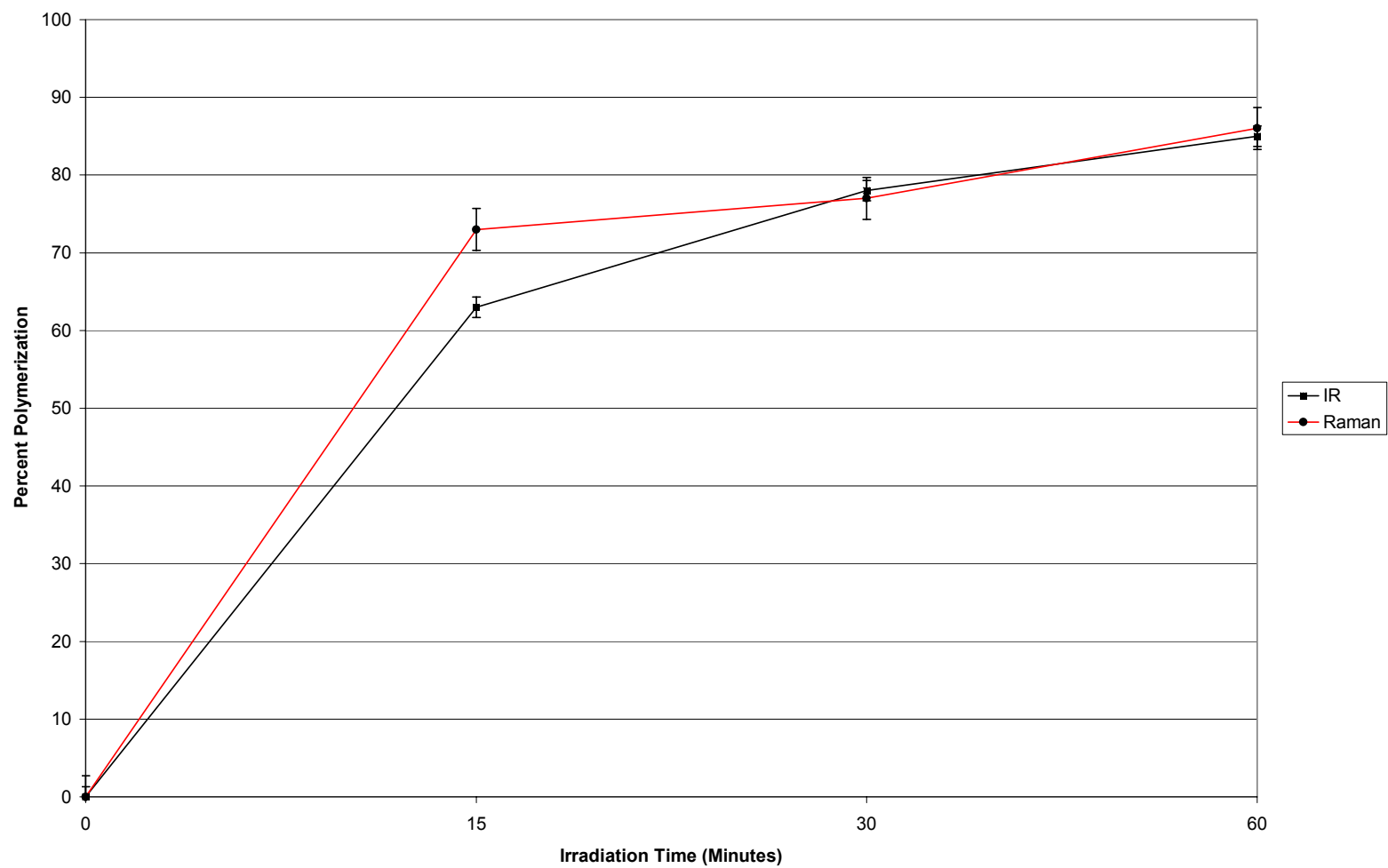


Figure III-5. Raman vs. ATR Measurement. Percent polymerization of monoacrylate-PC samples for a given irradiation period using both Raman microscopy (red) and Infrared Horizontal ATR (black) measurement methods with white light irradiation at $\sim 6\text{mW}$ power.

Percent Polymerization in minimally hydrated Lipid



Quantitation of Photopolymerization in minimally hydrated lipid sample with 514.5 nm irradiation by Raman Microscopy. The minimally hydrated lipid sample was irradiated for 0, 30, 90, 150, and 240 seconds. These irradiation times produced results that were achieved on the hour time scale with white light irradiation. The polymerization for each irradiation period was: 0, 12, 46, 59, 90, and 100 percent (Figure III-6). A discussion of the measurements and presentation of raw data is contained in Appendix A.

Quantitation of Photopolymerization in PTFE graft sample with 514.5 nm irradiation by Raman Microscopy. Samples of the PTFE graft were supplied by Emory University School of Medicine. The samples included a non-irradiated sample (Figure III-7a), a sample that was irradiated for a period of sixty seconds (Figure III-7b), a sample irradiated for 3.5 minutes, and a sample irradiated for 5 minutes using 514.5 nm wavelength light.. These values correspond to 0, 38, 76, and 100 percent polymerization respectively. Details of the subtraction, raw data, and a discussion concerning the possible error present in these measurements are contained in Appendix A.

Discussion

The widely accepted method for the analysis of degree cure, or percent polymerization, in polymer films is through real-time infrared spectroscopy.¹³⁻¹⁵ This method relies on the use of the ratio of the integrated intensity of the C=C and C=O vibrations to determine the percent polymerization occurring or a given irradiation period. Although this method utilizes the C=O vibration, any band that remains constant during irradiation may be used to compare changes in the C=C band to. However, for the membrane mimetic film that we were interested in, this approach was impractical. In trying to analyze the entire multilayer assembly via horizontal

Figure III-6. Percent Polymerization of Monoacrylate-PC measured by Raman Microscopy.

Polymerization of monoacrylate-PC

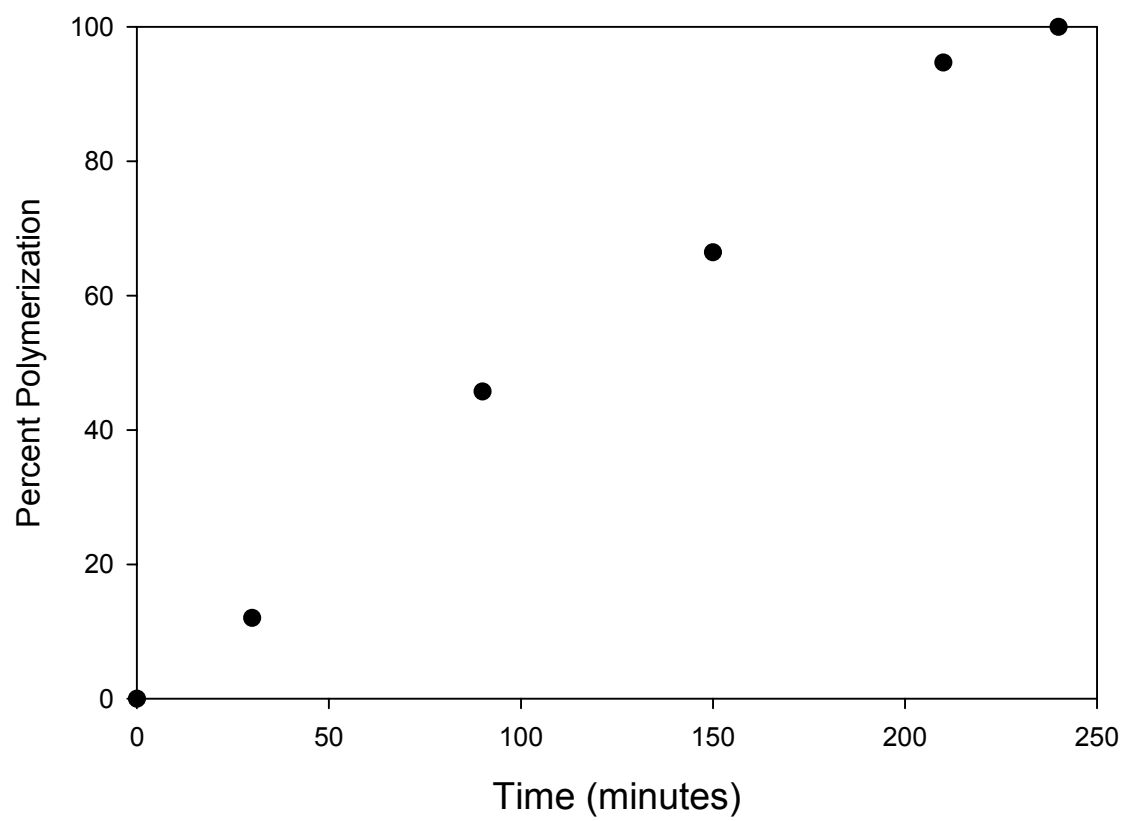
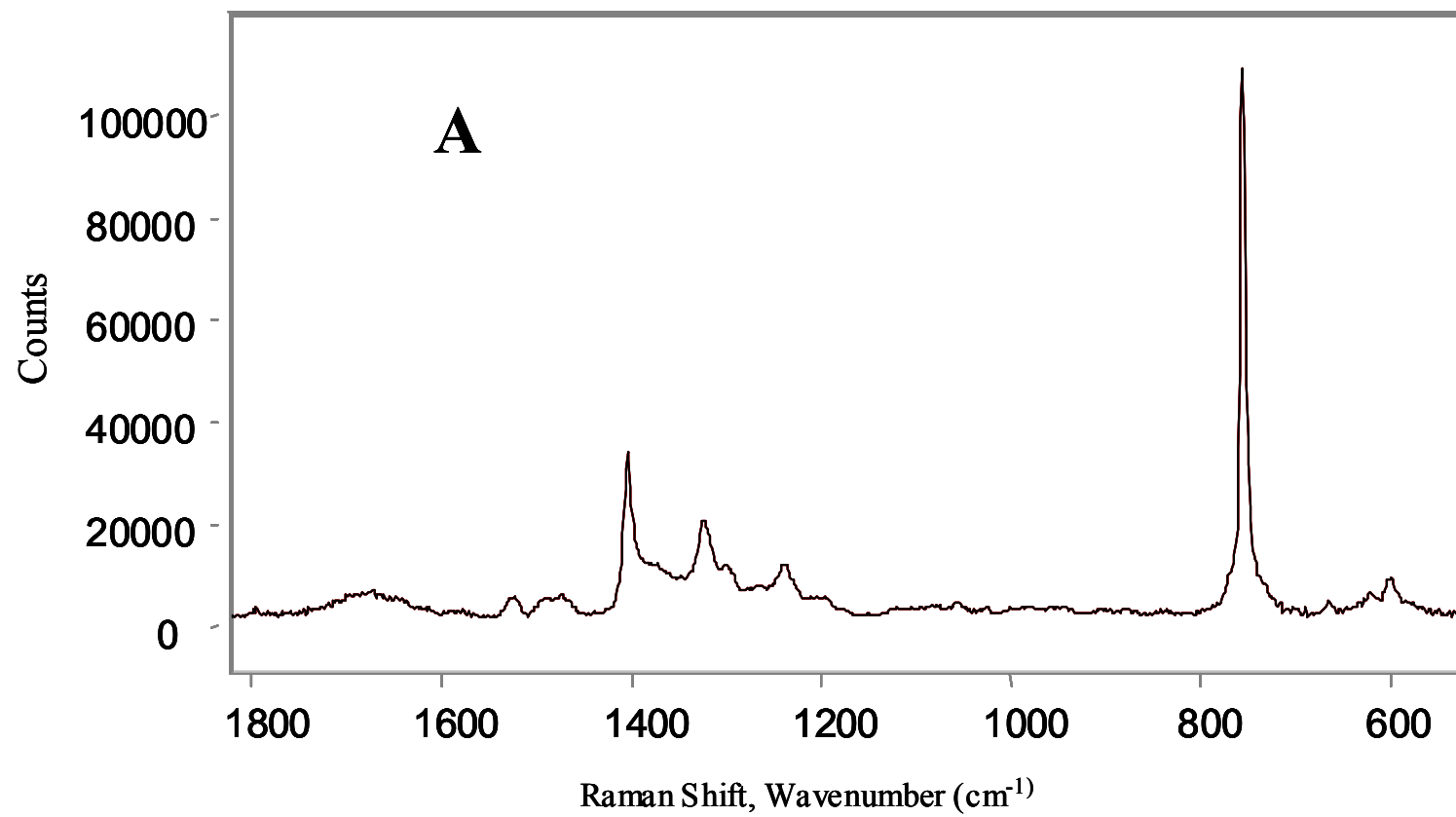
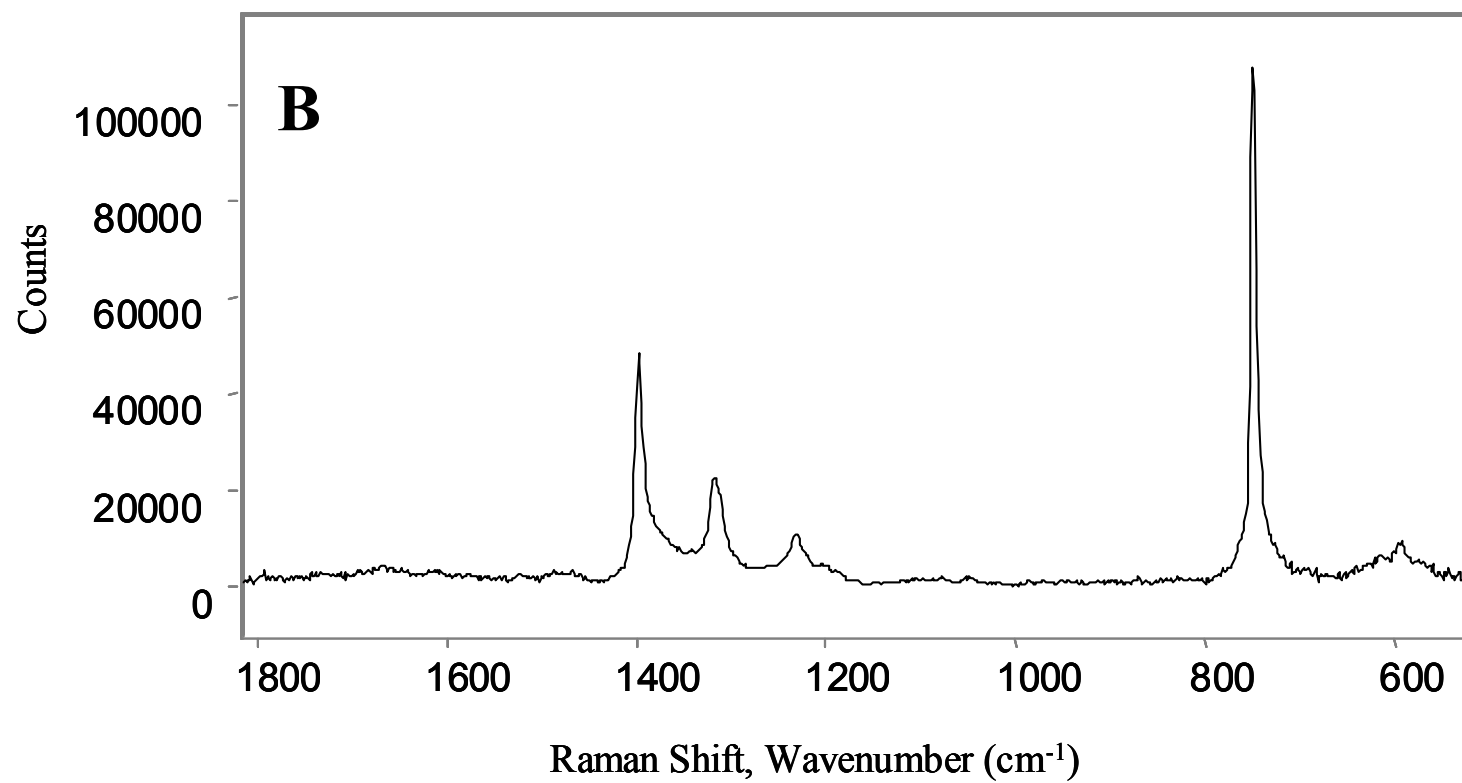


Figure III-7. (A). Raman spectrum of PTFE graft prior to irradiation. (B). Raman Spectrum of Graft after Irradiation.





attenuated total reflectance (HATR) infrared spectroscopy, the weak C=C stretch that is monitored to determine percent polymerization could be seen only with great difficulty. An attractive alternative to this technique was to use Raman microscopy due to its greater sensitivity to this type of vibration and also its relative insensitivity to water present in the sample, which masked the regions of interest as illustrated in Figure III-2a.

Prior to examination of the multilayer system (*fig. 1a*), the desired instrumental method was verified against accepted methodology. To do this, we used a simplified system composed of a minimally hydrated ARPC (Figure III-1b) solution and eosin Y photoinitiator. This simplified system allowed direct analysis of the regions of interest and yielded results that could be compared to the proposed analysis method. By using a minimally hydrated solution, the lipid still behaves as if fully hydrated, yet allows for analysis without interference from bulk water.¹⁶ Two different irradiation methods were utilized. The first was with a white light source to duplicate previous work⁵⁻¹² and also using visible light at 514.5 nm wavelength to more closely match the maximum absorption of the EY/triethanolamine photoinitiator. For samples irradiated with white light, the same sample was analyzed with both HATR FT-IR and also Raman microscopy. Irradiation of the PTFE graft sample with 514.5 nm wavelength light was accomplished through the use of an optical fiber inserted into the center of the graft.

For determining percent polymerization that occurs after a given period of irradiation in the minimally hydrated lipid sample by HATR FT-IR, a ratio of the integrated area of the C=C peak and the ester carbonyl band was used. The formula for this calculation can be related by equation III-1.

$$\text{Degree of cure} = A_0 - A_t / A_0 \quad (\text{III-1})$$

Where A_0 is equal to the ratio of the area of the C=C peak at 1621 cm^{-1} and the area of the ester carbonyl band centered at 1734 cm^{-1} and A_t is equal to the ratio of the same two peaks at a time t . The C=C stretch was completely masked by bulk water in both the graft sample and also in the lipid sample (Figure III-2a). Deuterium oxide was used in place of water to shift remaining bulk water bands and allow analysis of the 1750 to 1600 cm^{-1} region of the spectrum (Figure III-2b). We observed a decrease in the integrated ratio of the C=C stretching vibration as irradiation times increased while the ester carbonyl remained relatively constant. Although a quartz cover slip was placed over the lipid solution to prevent drying caused by the dry air purge of the spectrometer, it is our belief that the slight changes in intensity witnessed in the ester carbonyl band were due to sample drying for the extended irradiation times. Sample irradiation was stopped at the one-hour point due to drying of the sample. This limited the cross-linking to approximately eighty-two percent.

Each of these samples was also measured using Raman microscopy. The Raman measurement was performed immediately after the FT-IR measurement was taken. Figure III-4a illustrates the decrease in intensity for the C=C stretch measured by Raman microscopy after given periods of irradiation. A ratio of the integrated areas of the C=C stretch and the C-N stretch at 715 cm^{-1} , shown in Figure III-4b, was used in determining percent polymerization by the method described previously. The C-N stretch was chosen to perform the ratio because it does not change during irradiation and provides a sharp well-defined peak for analysis. The slight differences in percent polymerization between the Raman and IR spectra shown in Figure III-5 are possibly due to residual cure after the cessation of irradiation. The collection of spectra via Raman microscopy was much easier for these samples than with FT-IR. This coupled with the

close agreement of results between the two methods serves to validate the use of Raman microscopy for this type of analysis.

To examine possible spectroscopic improvements to the experiment, we used 514.5nm wavelength irradiation at ~100 mW of power with the minimally hydrated lipid sample to more closely match the absorption of the EY/triethanolamine photoinitiator. After irradiation, the samples were analyzed using Raman microscopy with the results being shown in Figure III-6. Several differences were readily apparent, the most noticeable of which was the greatly reduced irradiation times necessary to achieve results comparable to previous measurements taken with white light irradiation. The greatly reduced irradiation times necessary to achieve these results are attributed to a combination of increased intensity in the light being used for irradiation as well as the change in wavelength. The maximum absorbance of EY occurs at ~517 nm and it is our belief that the sample was able to fully polymerize due to the close wavelength match between the irradiation wavelength and the maximum absorbance of the EY. The full polymerization was achieved in four minutes time, which is a great improvement over the eighty-two percent polymerization that occurred after one hour of irradiation. Another benefit directly linked to the reduction in irradiation times was the elimination of sample drying.

Dr. Elliot Chaikof's research group at the Emory University School of Medicine supplied the PTFE graft containing the membrane-mimetic film of interest. The films provided were irradiated for 60, 210, and 300 seconds using 514.5 nm wavelength light at ~100 mW of power. In addition, a non-irradiated sample was provided as a baseline reference to determine zero percent polymerization. Analysis of these films was conducted in the manner described previously with the following modification. Due to several overlapping bands in the 1580 cm^{-1} to 1730 cm^{-1} region it was necessary to perform a spectral subtraction order to isolate the C=C

stretching vibration for analysis. This was accomplished by using a PTFE graft sample that included all of the layers of the membrane mimetic film with the exception of the monoacrylate-PC and photoinitiator as a background sample and subtracting this from samples of the membrane mimetic film irradiated for the given time periods. The percent polymerization values of 0, 38, 76, and 100 for the 0, 60, 210, and 300 second irradiation periods differ slightly from those of the minimally hydrated lipid solution (Figure III-8). We believe that this is due to the interaction with the other constituents present in the membrane mimetic film.

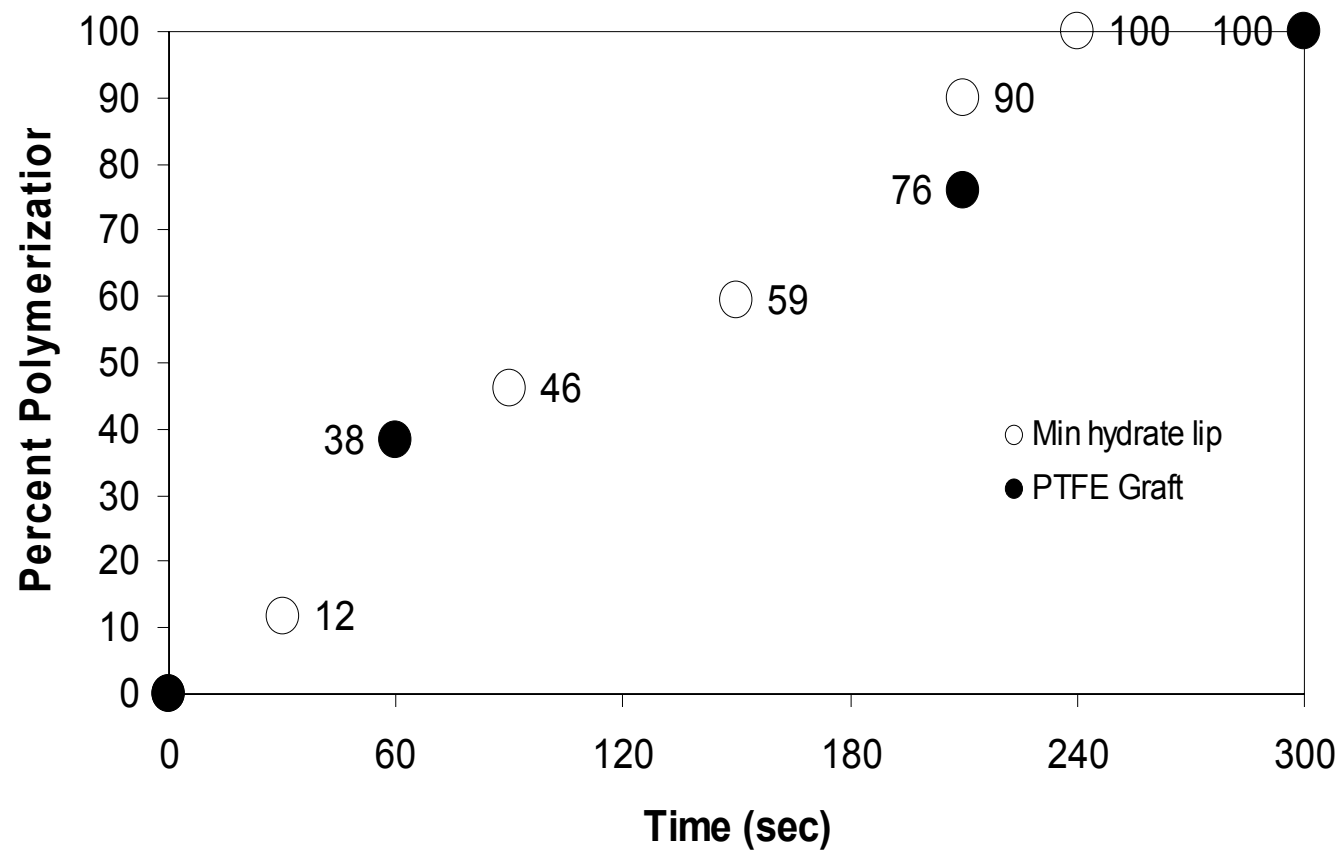
Conclusions

Raman microscopy has been shown to be a viable alternative to FT-IR spectroscopic techniques for the analysis of percent polymerization. Raman provides greater sensitivity to stretching modes such as the C=C stretch that is principle in this analysis. Due to the weak Raman scatter exhibited by water, Raman is also better suited to analysis of samples with higher water content. By closely matching the irradiation wavelength to the maximum absorbance of the EY photoinitiator, we were able to achieve complete polymerization of the membrane-mimetic film in a reasonably short time period eliminating several problems that existed with the previous irradiation method. Although the number of samples presented here are small, using the above methodology, we have been able to provide a rapid analysis technique for determining degree cure in graft samples which we hope will ultimately give the researcher a better idea of the long term stability in membrane-mimetic films immediately after fabrication. The accuracy of these measurements will be greatly improved as the pool of sample data becomes larger and the error inherent in small sample populations is decreased.

Acknowledgements

The research presented here was supported by grants from the National Institute of Health.

Figure III-8. Percent Polymerization for Graft measured by Raman Microscopy.



REFERENCES

1. Hayward, J.A. and Chapman, D., *Biomembrane Surfaces as Models for Polymer Design - the Potential for Hemocompatibility*. *Biomaterials*, **1984**. 5(3): 135-42.
2. Hall, B., et al., *Biomembranes as Models for Polymer Surfaces .5. Thromboelastographic Studies of Polymeric Lipids and Polyesters*. *Biomaterials*, **1989**. 10(4): 219-24.
3. Ishihara, K., et al., *Hemocompatibility on Graft-Copolymers Composed of Poly(2-Methacryloyloxyethyl Phosphorylcholine) Side-Chain and Poly(N- Butyl Methacrylate) Backbone*. *J. Biomed. Mater. Res.*, **1994**. 28(2): 225-32.
4. Sackmann, E., *Supported Membranes: Scientific and Practical Applications*. *Science*, **1996**. 271(5245): 43-48.
5. Marra, K.G., et al., *Cytomimetic Biomaterials .1. In-Situ Polymerization of Phospholipids on an Alkylated Surface*. *Macromolecules*, **1997**. 30(21): 6483-88.
6. Mauk, A.W., et al., *Structural Characterization of Self-Assembled Lipid Monolayers by N Pi T Simulation*. *Langmuir*, **1998**. 14(18): 5255-66.
7. Winger, T.M. and Chaikof, E.L., *Synthesis and Characterization of Supported Phospholipid Monolayers: A Correlative Investigation by Radiochemical Titration and Atomic Force Microscopy*. *Langmuir*, **1998**. 14(15): 4148-55.
8. Winger, T.M., et al., *Formation and Stability of Complex Membrane-Mimetic Monolayers on Solid Supports*. *Langmuir*, **1999**. 15(11): 3866-74.

9. Liu, H., et al., *A Membrane-Mimetic Barrier for Cell Encapsulation*. Langmuir, **2002**. 18(4): 1332-39.
10. Orban, J.M., et al., *Cytomimetic Biomaterials. 4. In-Situ Photopolymerization of Phospholipids on an Alkylated Surface*. Macromolecules, **2000**. 33(11): 4205-12.
11. Marra, K.G., et al., *Cytomimetic Biomaterials. 2. In-Situ Polymerization of Phospholipids on a Polymer Surface*. Langmuir, **1997**. 13(21): 5697 - 701.
12. Chon, J.H., et al., *Cytomimetic Biomaterials. 3. Preparation and Transport Studies of an Alginate Amphiphilic Copolymer Polymerized Phospholipid Film*. J. Biomat. Sci. Polymer Ed., **1999**. 10(1): 95-107.
13. Allen, N.S., et al., *Photopolymerization Activity of Perester Derivatives of Fluorenone and Benzophenone - a Real-Time Ftir and Differential Photocalorimetric Study*. Eur. Polym. J., **1990**. 26(9): 1041-47.
14. Allen, N.S., et al., *Photochemistry and Photopolymerization Activity of Perester Derivatives of Benzophenone*. J. Appl. Polym. Sci., **1991**. 42(5): 1169-78.
15. Yang, D.B., *Kinetic-Studies of Photopolymerization Using Real-Time Ft-Ir Spectroscopy*. J. Polym. Sci. Pol. Chem., **1993**. 31(1): 199-208.
16. Cevc, G. and Marsh, D., *Lipid Hydration*, in *Phospholipid Bilayers*. 1987, Wiley-Interscience: Toronto. p. 57-97.

CHAPTER IV

REAL-TIME FT-IR MEASUREMENTS OF PHOTO-INITIATED POLYMERIZATION²

²Murphy, M.R.; Sanderson, C.T.; Kutal, C.R.; and Dluhy, R.A. Work to be submitted for publication at a future date.

Abstract

Photoinitiation is one of the most efficient methods for achieving near instantaneous polymerization. In this work, we use Fourier transform infrared spectroscopy for the study of the kinetics involved in the transformation of the liquid monomer into a solid polymer material. Horizontal attenuated total reflectance (HATR) spectroscopy is used to monitor the polymerization process in real-time and provides us with quantitative data concerning the degree of cure and rate of reaction. In the search for more efficient photoinitiators, the use of ferrocene, ruthenocene, and benzoyl substituted metallocenes anionic photoinitiators is investigated. Each of these dissolves readily in neat ethyl 2-cyanoacrylate (CA) monomer and form a photosensitive donor-acceptor complex with CA. In contrast to previous work, very low concentrations of FeCp_2 , RuCp_2 , benzoylferrocene, 1,1'-dibenzoylferrocene, and 1,1'-dibenzoylruthenocene are sufficient for the photoinitiated polymerization of neat CA. The reaction mechanism and the relative rates of reaction are discussed for each photoinitiator. The work presented here demonstrates the effectiveness of the classical metallocenes as well as benzoyl substituted metallocenes as photoinitiators.

Introduction

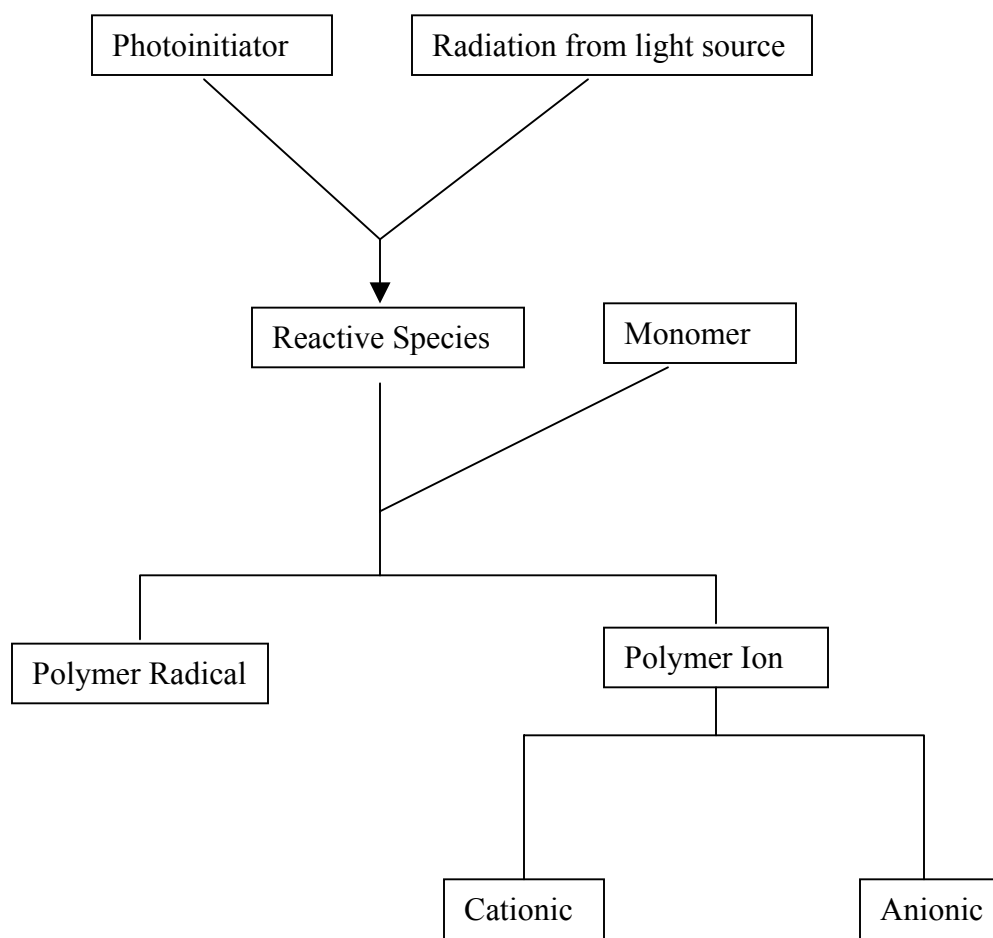
Photopolymerization is a light-induced process that transforms a lower molecular mass precursor into a polymeric substance by a chain reaction. The chain reaction is initiated by reactive species, which are formed by irradiation with ultraviolet (UV), visible, or infrared (IR) light. Most monomers do not produce initiating species with sufficiently high yields when they are exposed to light, so a photoinitiator must be added to the formulation. Once initiated, the chain reaction will develop very much like in a conventional thermal polymerization, except for the much larger rates of initiation that can be reached by intense illumination. The overall

process can be represented schematically as shown in figure IV-1. As shown, the polymerization may proceed by two different pathways, either radical or ionic. The most commonly used pathway in commercial application is the radical polymerization. Radical polymerization begins by adding a monomer to a radical that is produced from a suitable initiator compound. The added radical will be the tail of the ultimately formed polymer chain. However, its nature or the nature of the initiator have minor effects on the features such as propagation rate, the selectivity, or the stereochemistry of the ensuing propagation.¹⁻⁴ All of these characteristics of radical propagation are determined mainly by the nature of the monomer and by reaction conditions, although the importance of end-groups in polymer structure formed in initiation and termination is recognized in recent research.⁵

In contrast to radical polymerization, ionic polymerization begins with the interaction of the monomer with a species bearing an electronically charged or highly polar active group. Cationic polymerization refers to the process in which chain growth involves a positively charged or electrophilic active center at the chain ends. An analogous description holds for anionic polymerization. One noticeable feature of ionic polymerization is that as long as the electronically charged end-groups are formed, the corresponding counter ions have to be present in the polymerization system to maintain its electric neutrality. Therefore, the rate constant and the mode of ionic propagation are affected by the nature of the initiating species and its counter ion. This is due to the changeable character of the propagating groups and to the role of the counter ions that are associated with the growing active center throughout the course of the propagation.

Monomers demonstrate a varying extent of selectivity with respect to the types of active center (radical, cationic, or anionic) that brings about the polymerization. Although all three

Figure IV-1. Schematic of Photoinitiated Reaction.

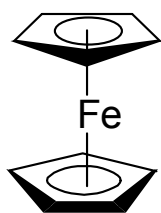


types of initiators are employed in chain growth polymerization reactions, their applicability towards monomers is not indiscriminate.⁶ While many monomers will undergo polymerization with a radical initiator, those used commercially are limited to the vinyl, vinylidene, and diene monomers. On the other hand, versatile monomers, such as aldehydes, ketones, vinyl ethers, and numerous heterocyclics are only polymerized by ionic procedures.² It is not surprising that some cationic initiators may not start the polymerization of some monomers while other monomers may be inert to anionic initiators if we keep in mind the selective feature of ionic initiating processes.

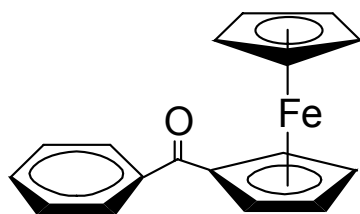
Due to the selective nature of monomers, new types of photoinitiators are constantly being sought. The majority of reported initiators are radicals or strong acids⁷⁻¹¹ These common photoinitiators are almost solely organic compounds. Work in the Kutal group in recent years has focused on increasing the number of organometallic compounds used as photoinitiators.¹² Of particular interest has been the use of classic metallocenes, ferrocene and ruthenocene, along with benzoylferrocene and dibenzoylferrocene (Figure IV-2). Both FeCp_2 and RuCp_2 (where Cp denotes $\eta^5\text{-C}_5\text{H}_5$) dissolve in a wide range of aqueous solvents and exhibit good thermal stability in solution.

In solvents such as methanol, acetone, and cyclohexane the compounds are photoinert.¹³ However, in CCl_4 and other electron-accepting media they form ground state donor-acceptor (D-A) complexes with the solvent and are characterized by a charge-transfer-to-solvent (CTTS) absorption band in the near UV region. Irradiation into this band causes the one electron oxidation of the metallocene to the corresponding metallocenium cation accompanied by a reduction to its radical anion.¹⁴⁻¹⁷ The CTTS interaction is shown in Figure IV-3. In our

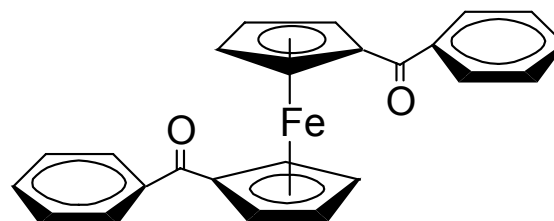
Figure IV-2. Metallocene Structure.



Ferrocene



Benzoylferrocene



1,1'-Dibenzoylferrocene

examination of the metallocenes as photoinitiators, one item of particular interest was the reaction kinetics of these types of photoinitiators.

The kinetics involved in photoinitiated polymerization have been studied extensively over the years.¹⁸⁻²⁷ This work has been conducted mainly by differential scanning calorimetry (DSC), a technique that is hampered by its poor time resolution, which may require up to ten seconds, and thus requires operation at low light intensities for real-time monitoring. This explains why only a few kinetic studies have been reported on photo-curing reactions performed under conditions similar to those commonly found in industrial applications, namely thin films exposed to intense UV radiation in the presence of air.²⁸⁻³⁰ Fourier Transform infrared (FT-IR) spectroscopy has provided a means by which the polymerization may be studied in real time.^{31, 32} With advances in technology, modern FT-IR spectrometers are capable of ten-millisecond time resolution per scan. The available speed of these instruments makes them suitable for measurement of all but the fastest polymerization reactions. The work presented here outlines the analysis and kinetic study of ferrocene, ruthenocene, benzoylferrocene, and 1,1'-dibenzoylferrocene as photoinitiators for the anionic polymerization of ethyl 2-cyanoacrylate by real time analysis with FT-IR horizontal attenuated total reflectance (HATR) spectroscopy.

Materials and Methods

Reagents. Ferrocene and ruthenocene (98% and 97%, respectively) were obtained from Sigma-Aldrich (St. Louis, MO.) and were further purified by vacuum sublimation. The monomer, high purity ethyl 2-cyanoacrylate (CA) (99.9%) was obtained from Loctite Corp. (Rocky Hill, CT) and used as received. The colorless liquid monomer contained hydroquinone as a scavenger for adventitious radicals and methanesulfonic acid for the removal of basic impurities. Ethyl 2-cyanopropionate (98.2%) was procured from TCI America (Portland, OR). Methanesulfonic

Figure IV-3. Charge-Transfer-To-Solvent of FeCp₂ and Electron Accepting Solution.



acid and reagent grade tetrahydrofuran (THF) were obtained from Fisher Chemicals (Fairlawn, NJ). Benzoylruthenocene and 1,1' Dibenzoylruthenocene were synthesized in-house using a modified literature procedure.³³ They were deemed pure by elemental analysis, and melting point.

Instrumentation. *Excitation.* An Illumination Industries 200 W high-pressure mercury-arc lamp was used for photoinitiation. Polychromatic light of wavelengths >290 nm was obtained by passing the full output of the lamp through Pyrex glass. Power at the sample position for ruthenocene was 33 mW/cm^2 . For ferrocene, benzoylferrocene, and 1,1' - dibenzoylferrocene the power at the sample was 110 mW/cm^2 . The light was steered to the sample compartment of the spectrometer using a broadband mirror (Newport Optics, Irvine, Ca.). Light was passed into the sample compartment of the spectrometer through a quartz window manufactured on site.

Infrared Analysis. Spectra of FeCp_2 and RuCp_2 were collected using a Bio-Rad Fourier Transform Infrared Spectrometer FTS-60 (Bio-Rad, Digilab Division, Cambridge, MA) equipped with a narrow-band, liquid nitrogen cooled HgCdTe detector (Infrared Associates, Orlando, FL). A horizontal attenuated total reflectance (HATR) sampling accessory (CIC Photonics Inc., Albuquerque, NM) was used with a germanium ATR crystal (Spectral Systems, Hopewell Junction, NY). Infrared absorbance spectra were collected every 1.5 seconds with 1 co-added scan, triangular apodization and one level of zero filling with 4 cm^{-1} resolution. Spectra of benzoylferrocene and 1,1' - dibenzoylferrocene were taken using a DigiLab FTS-7000 spectrometer equipped with a narrow band MCT detector. The HATR sampling accessory and Ge crystal used for these experiments are the same as previously indicated. Infrared absorbance spectra were taken every 0.8 seconds with 1 co-added scan, triangular apodization, 1 degree of

zero filling, and 4 cm^{-1} resolution. To ensure that an accurate comparison could be made, FeCp_2 was also analyzed using the FTS-7000 with excellent agreement between the two systems.

Software. Spectra collected on the FTS-60 spectrometer were acquired using WinIR software supplied by the manufacturer. Similarly, data acquired on the FTS-7000 were collected with an updated version of WinIR supplied by the manufacturer. All post collection processing of data contained in this paper was performed using *Grams32/AI* spectral software package (Galactic Industries (Nashua, NH)). Center of gravity calculations were made using a Grams 32 based program written in our laboratory (R.A. Dluhy, unpublished). This program calculates peak area and center peak position along with peak heights. Spreadsheets and graphs were produced using Excel (Microsoft Corporation, Redmond, WA).

Sample preparation. All spectral data were collected on freshly prepared samples of CA and the metallocene photoinitiators. The concentration of ruthenocene in CA was 10.0 mM while ferrocene was used at a concentration of 9.6 mM. The concentration of benzoylferrocene and 1,1' - dibenzoylferrocene in CA was 10.0 mM. For analysis, approximately $0.3\ \mu\text{L}$ of the sample solution was placed on a 45-degree trapezoidal shaped germanium horizontal ATR crystal that was cleaned by sonicating for 15 minutes in a solution of THF. Methanesulfonic acid was added as an inhibitor to the CA sample solutions in varying concentrations to illustrate the reaction proceeds via an anionic rather than radical polymerization mechanism.

Results and Discussion

Ferrocene as an anionic photoinitiator. The sample solution of CA containing ferrocene was placed on the germanium crystal inside the sample compartment of the spectrometer. A spectrum of the sample solution was taken prior to irradiation and monitored for a period of 15 minutes to

illustrate thermal stability of the compound. After acquisition of the dark scan, the sample was irradiated with the mercury arc lamp as shown in Figure IV-4. The infrared absorbance collection was begun one second prior to the beginning of irradiation in order to acquire a “dark” spectrum for reference purposes (Figure IV-5). Irradiation of the sample continued until no change in the collected spectra was observed (~2100 seconds). The final spectrum obtained from the set is shown in Figure IV-6.

Calculations based on the refractive index of CA being 1.5 and 4.0 for Germanium and a 45° angle for the trapezoidal crystal shape, yielded the depth of penetration into the sample on the crystal of ~3 μm.³⁴ The widely accepted method for the analysis of degree of cure, or percent polymerization, in polymer films relies on the use of the ratio of the integrated intensity of the C=C and C=O vibrations to determine the percent polymerization occurring for a given irradiation period.^{32, 35-37} Equation IV-1 is used in calculating the percent polymerization:

$$\text{PercentPolymerization} = \frac{A_0 - A_t}{A_0} \times 100 \quad (\text{IV-1})$$

where A_0 is equal to the initial ratio of the area of the C=C peak at 1616 cm^{-1} and the area of the ester carbonyl band centered at 1738 cm^{-1} and A_t is equal to the ratio of the area of the same two bands after irradiation for time t . Plots of percent polymerization versus time is shown in Figure IV-7 for samples of neat CA containing ferrocene and ferrocene plus methanesulfonic acid, an inhibitor. From the non-irradiated plot, it can be determined that the sample is thermally stable at room temperature. The irradiated plot shows us that the polymerization exhibits a slight induction period followed by rapid conversion which slows as it approaches a maximum conversion of ~ 86%. The initial induction period is attributed to the presence of 5-10 ppm methanesulfonic acid (MSA) in the commercial monomer, which serves as a scavenger for adventitious traces of basic impurities. The polymerization process is inhibited until a sufficient

Figure IV-4. Irradiation Assembly Components: A. High-pressure mercury lamp. B. Water filter
C. Angled mirror to direct polychromatic light into the spectrometer sample chamber, striking
sample solution. D. Quartz replacement window to maintain purge environment inside
instrument. E. Fourier Transform Infrared Spectrometer

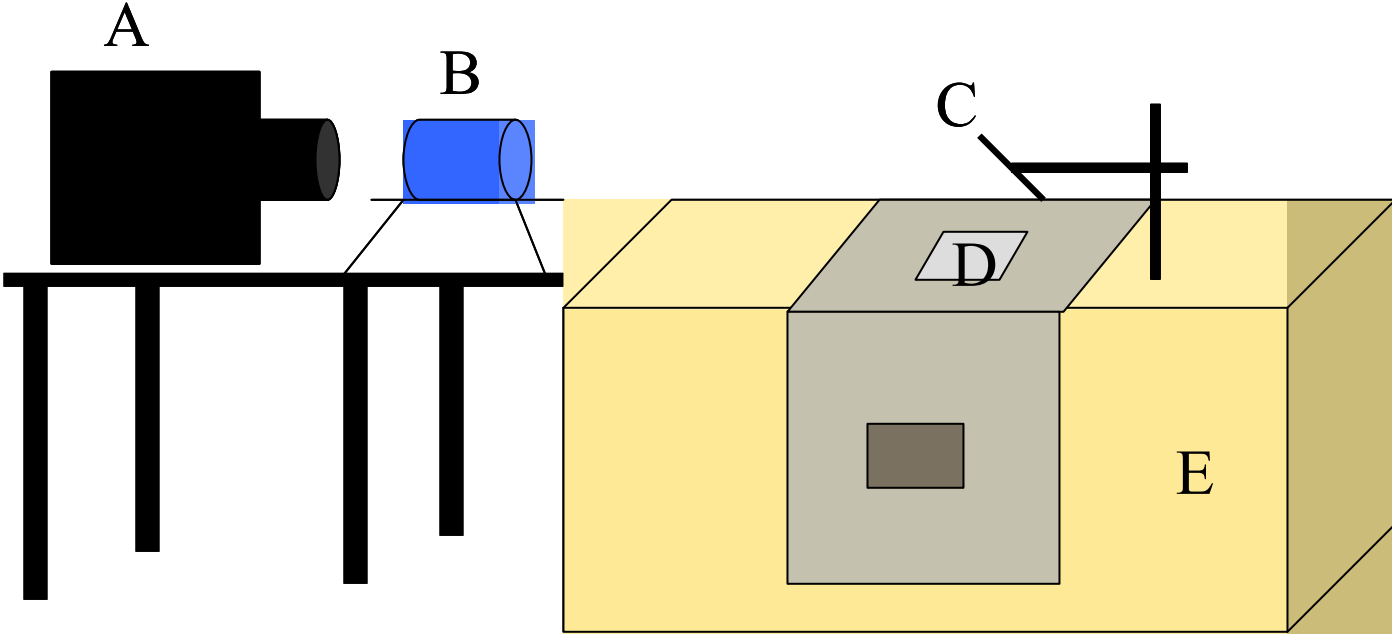
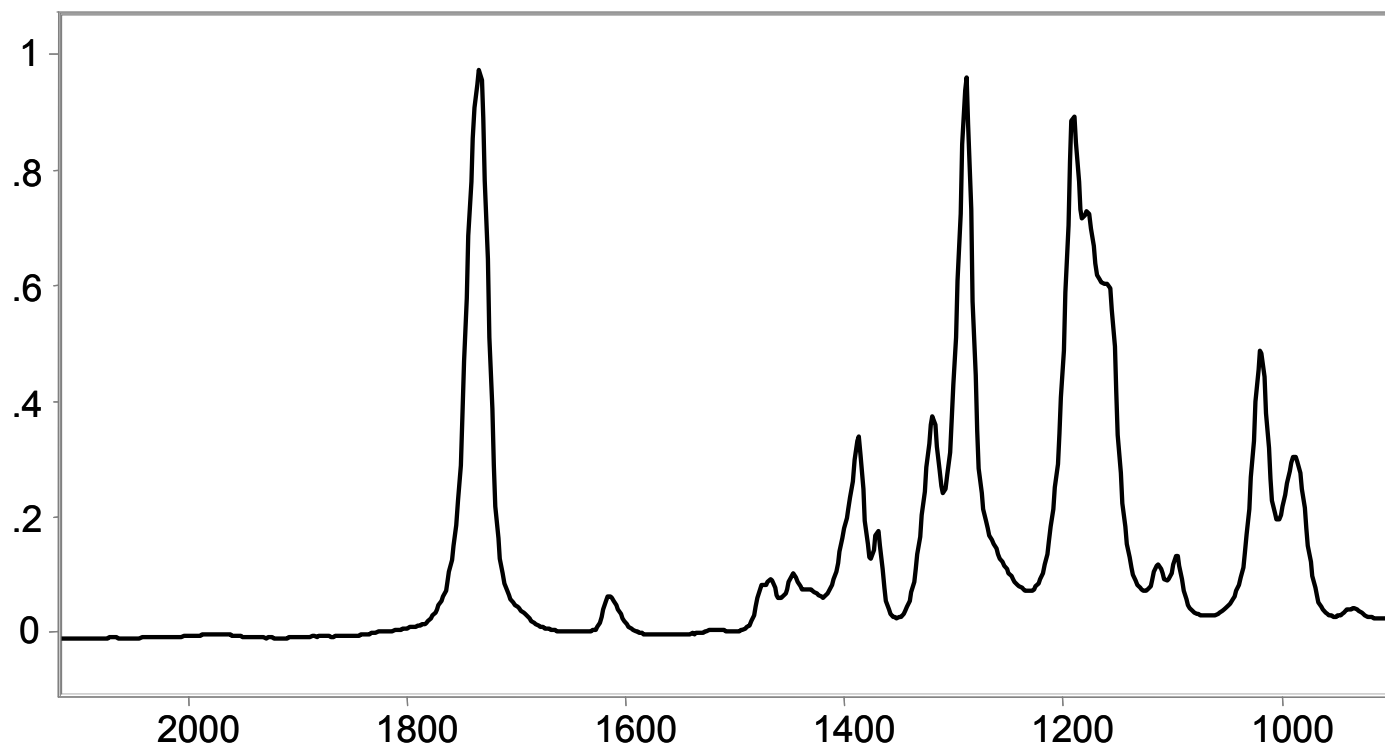


Figure IV-5. Spectrum of CA containing FeCp₂ before irradiation. Note the C=C band at 1616 cm⁻¹.



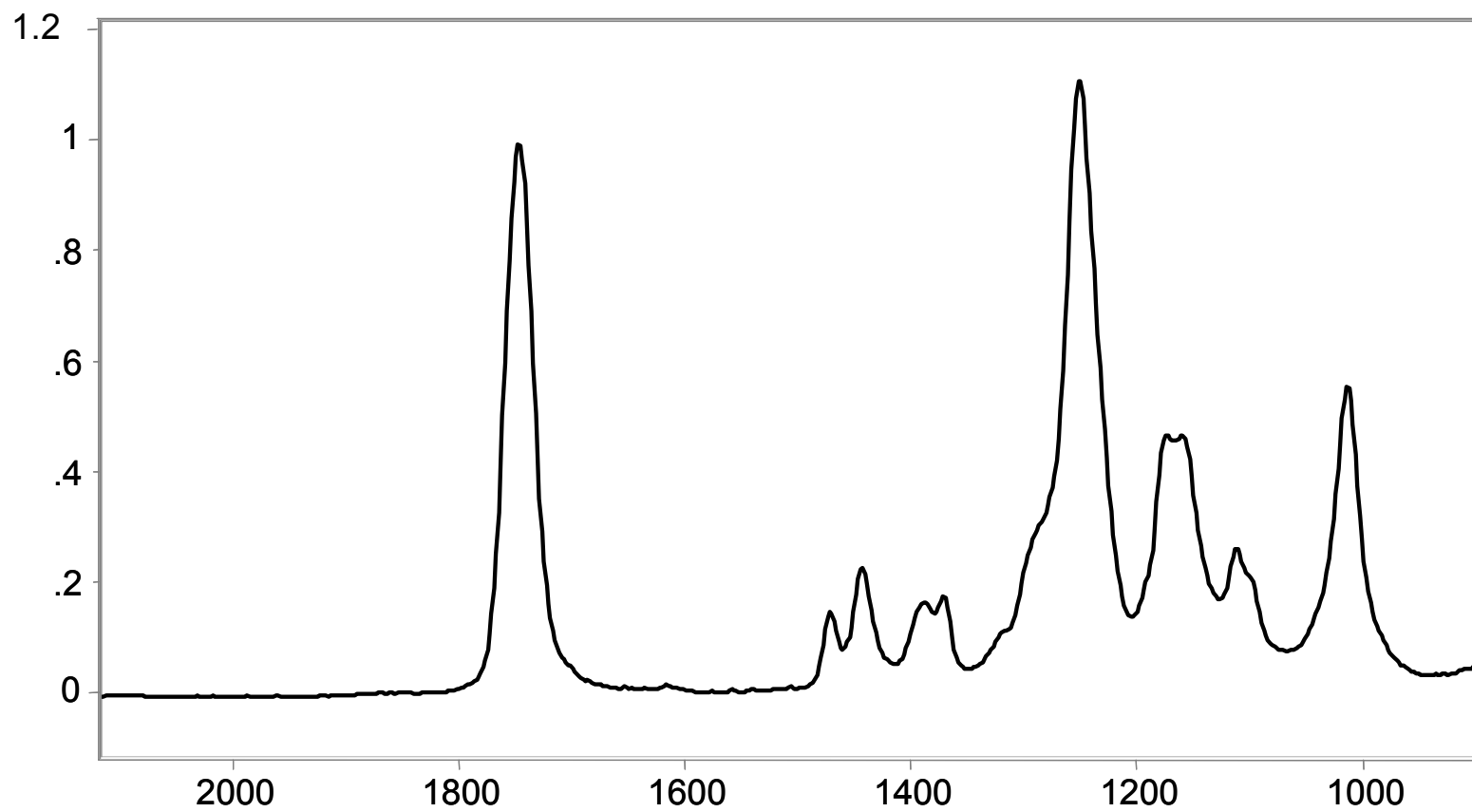
Absorbance / Wavenumber (cm-1)

File # 2 = FECPWILL#1 @0 Seconds

Paged X-Zoom CURSOR

10/18/2001 11:17 AM Res=4cm-1

Figure IV-6. Spectrum of CA containing FeCp₂ after irradiation. Note the disappearance of the C=C band at 1616 cm⁻¹.



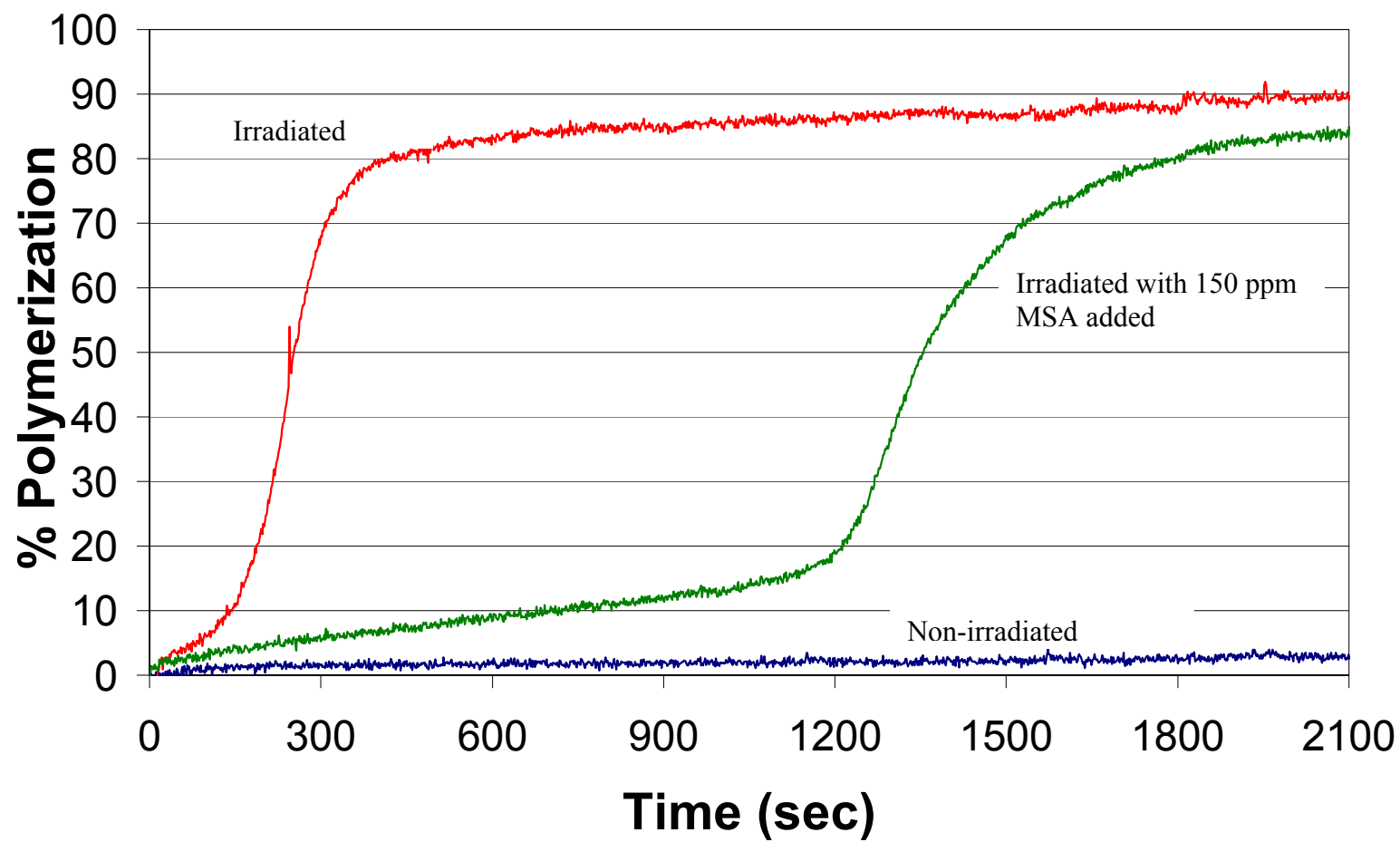
Absorbance / Wavenumber (cm-1)

Paged X-Zoom CURSOR

File # 1 = FECPWILL#1800 @2590.722 Seconds

10/18/2001 11:17 AM Res=4cm-1

Figure IV-7. Plot of Polymerization versus Time for CA containing FeCp₂. Irradiated samples were exposed to 110 mW/cm² of polychromatic light from a high-pressure mercury lamp. MSA is methanesulfonic acid, an inhibitor.



number of anionic species are photochemically generated to overcome the effects of the MSA. The anionic species is formed through a donor-acceptor complex between the FeCp_2 and CA as illustrated in Figure IV-8. After the effect of the inhibitor is overcome, rapid consumption of the monomer takes place.

The third plot in Figure IV-7 shows the effects of the addition of MSA at 150 ppm. Not surprisingly, a significant increase in the induction period witnessed previously occurs. The rate of polymerization, R_p , may be calculated using equation IV-2:

$$R_p = \frac{M(A_{t_1} - A_{t_2})}{A_0(t_2 - t_1)} \quad (\text{IV-2})$$

where A_{t_1} and A_{t_2} represent the areas of the 1616 cm^{-1} band at the indicated times and M is the molar concentration of the vinyl groups in the monomer. Using the data shown in Figure IV-7, a maximum rate of 0.060 M s^{-1} is obtained for the sample containing ferrocene with no added inhibitor. Another quantity of interest is the polymerization chain length or number of monomer units reacted per photogenerated initiating species. Conservatively assuming that each ferrocene molecule photochemically produces one anionic initiator, it is estimated that a chain length of greater than 700 units is formed.

Ruthenocene as an anionic photoinitiator. The sample solution of CA containing ruthenocene was placed on the germanium crystal inside the sample compartment of the spectrometer. A spectrum of the sample solution was taken prior to irradiation and monitored for a period of 10 minutes to illustrate thermal stability of the compound. After acquisition of the dark scan, the sample was irradiated with the mercury arc lamp. The infrared absorbance collection was begun one second prior to the beginning of irradiation in order to acquire a “dark” spectrum for reference purposes (Figure IV-9). Irradiation of the sample continued until no change in the collected spectra was observed (~600 seconds). The final spectrum obtained from the set is

Figure IV-8. Mechanism of D-A Complex Between Ferrocene and Solvent.

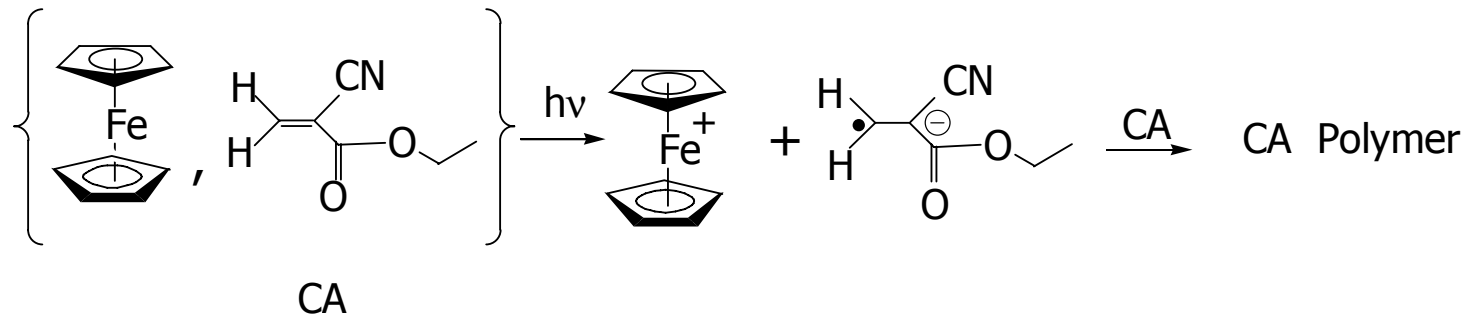
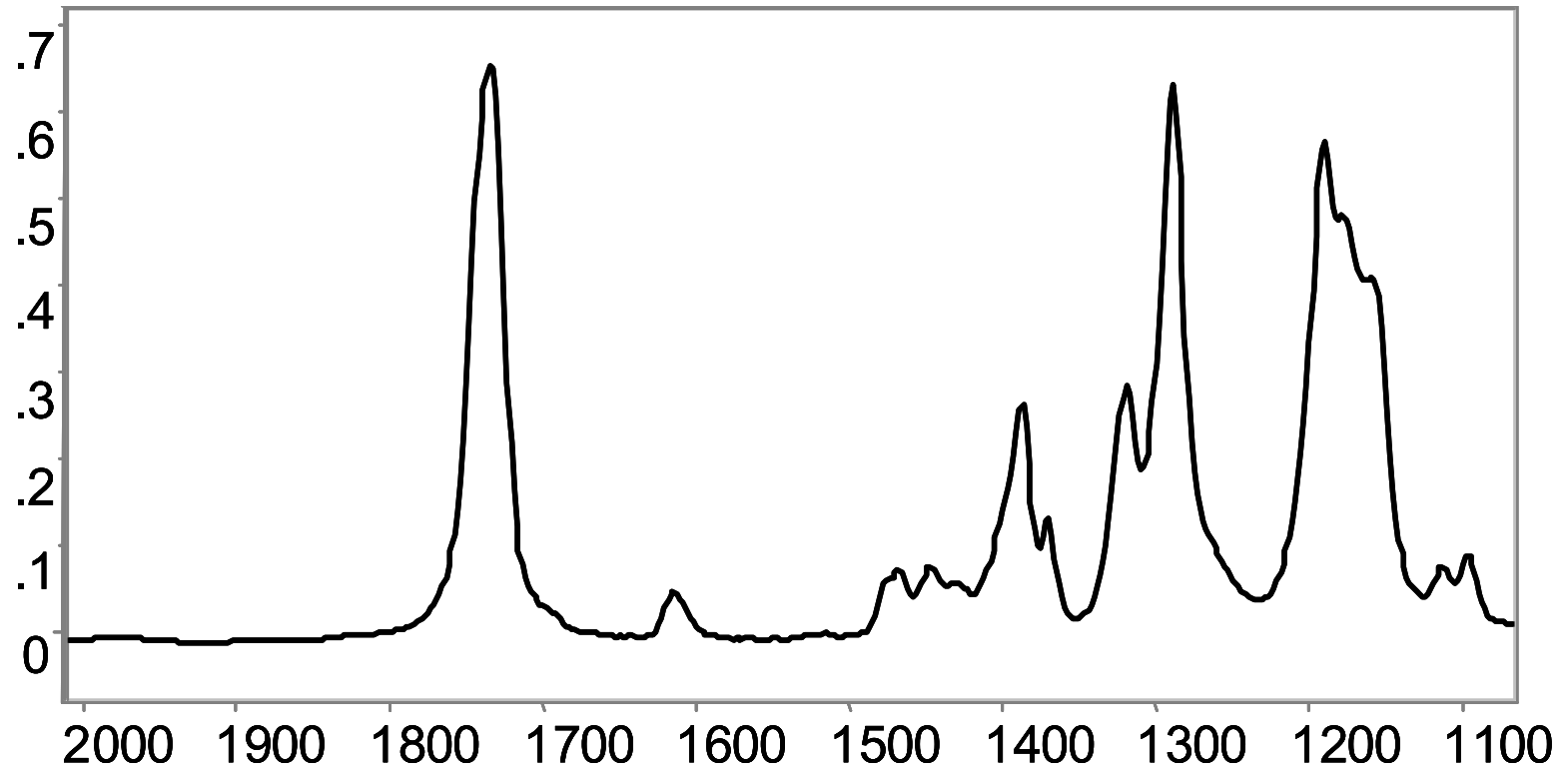


Figure IV-9. Spectrum of CA containing RuCp₂ before irradiation. Note the C=C band at 1616 cm⁻¹.



Absorbance / Wavenumber (cm-1)
File# 1 = 1021RU~1#1 @.0151188

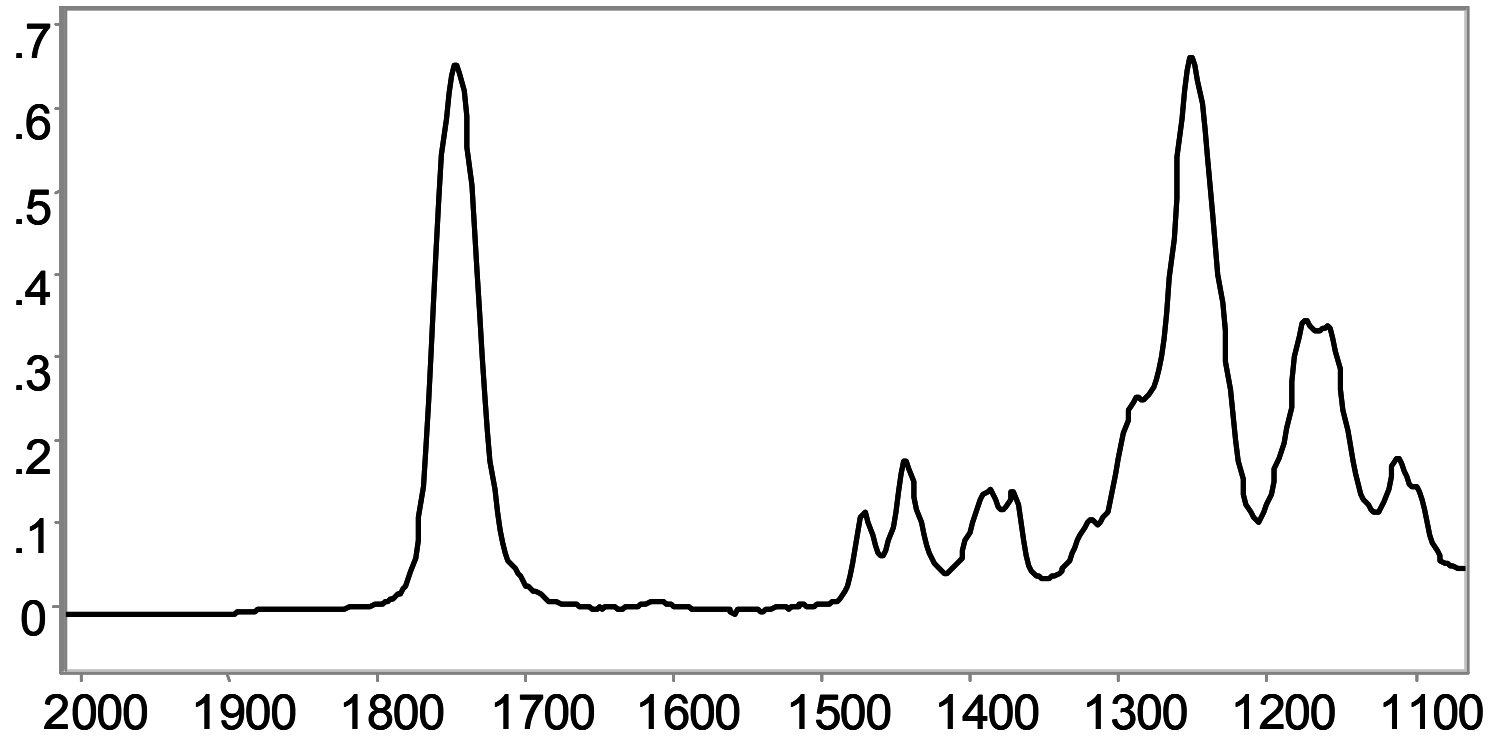
Paged X-Zoom CURSOR
10/21/2003 4:03 PM Res=4

shown in Figure IV-10. Plots of percent polymerization versus time are shown in Figure IV-11 for samples of neat CA containing ruthenocene and ruthenocene plus methanesulfonic acid.

As with the ferrocene sample discussed previously, we see an induction period for the ruthenocene as well. Using ruthenocene as a photoinitiator, we see a much quicker rate of polymerization than when using ferrocene. The R_p for the sample containing ruthenocene and no inhibitor is 0.5 M s^{-1} , a substantial increase. For the ruthenocene sample, the reaction is nearly complete at the 50-second mark, reaching a maximum polymerization of $\sim 82\%$. Ruthenocene exhibits nearly a tenfold increase in the rate of reaction as compared to ferrocene. In reviewing the electronic absorption spectrum of the two species, ruthenocene exhibits a much higher absorbance value than does ferrocene, which accounts for the faster rate of polymerization in its presence. The mechanism of the reaction is the same by which ferrocene reacts. In this case, ruthenocene is more photosensitive.

Benzoylferrocene and 1,1' - Dibenzoylferrocene as anionic photoinitiators. In solvents such as methanol, ferrocene is photoinert. However, 1,1'-dibenzoylferrocene (DFc) (figure IV-2) readily undergoes heterolytic metal-ring bond cleavage in this solvent to yield the benzoyl-substituted cyclopentadienide ion and the corresponding half-sandwich cationic complex (figure IV-12). This change in photochemical behavior reflects the metal-to-ligand-charge-transfer (MLCT) character of the low energy excited states of the benzoyl-containing derivative. The resonance structure shown in figure IV-13 illustrates the reduced hapticity of a cyclopentadienyl ring and enhanced susceptibility of the metal center to nucleophilic attack.³⁸ This provides an efficient route for the photogeneration of anions. Previous work has established DBF as an effective photoinitiator for the anionic polymerization of ethyl α -cyanoacrylate,³⁹ here we confirm those findings.

Figure IV-10. Spectrum of CA containing RuCp₂ after irradiation. Note the disappearance of the C=C band at 1616 cm⁻¹.



Absorbance / Wavenumber (cm-1)
File # 1 = 1021RU~1#674 @10.1143

Paged X-Zoom CURSOR
10/21/2003 4:03 PM Res=4

Figure IV-11. Plot of Polymerization versus Time for CA containing RuCp₂. Irradiated samples were exposed to 33 mW/cm² of polychromatic light from a high-pressure mercury lamp. MSA is methanesulfonic acid, an inhibitor.

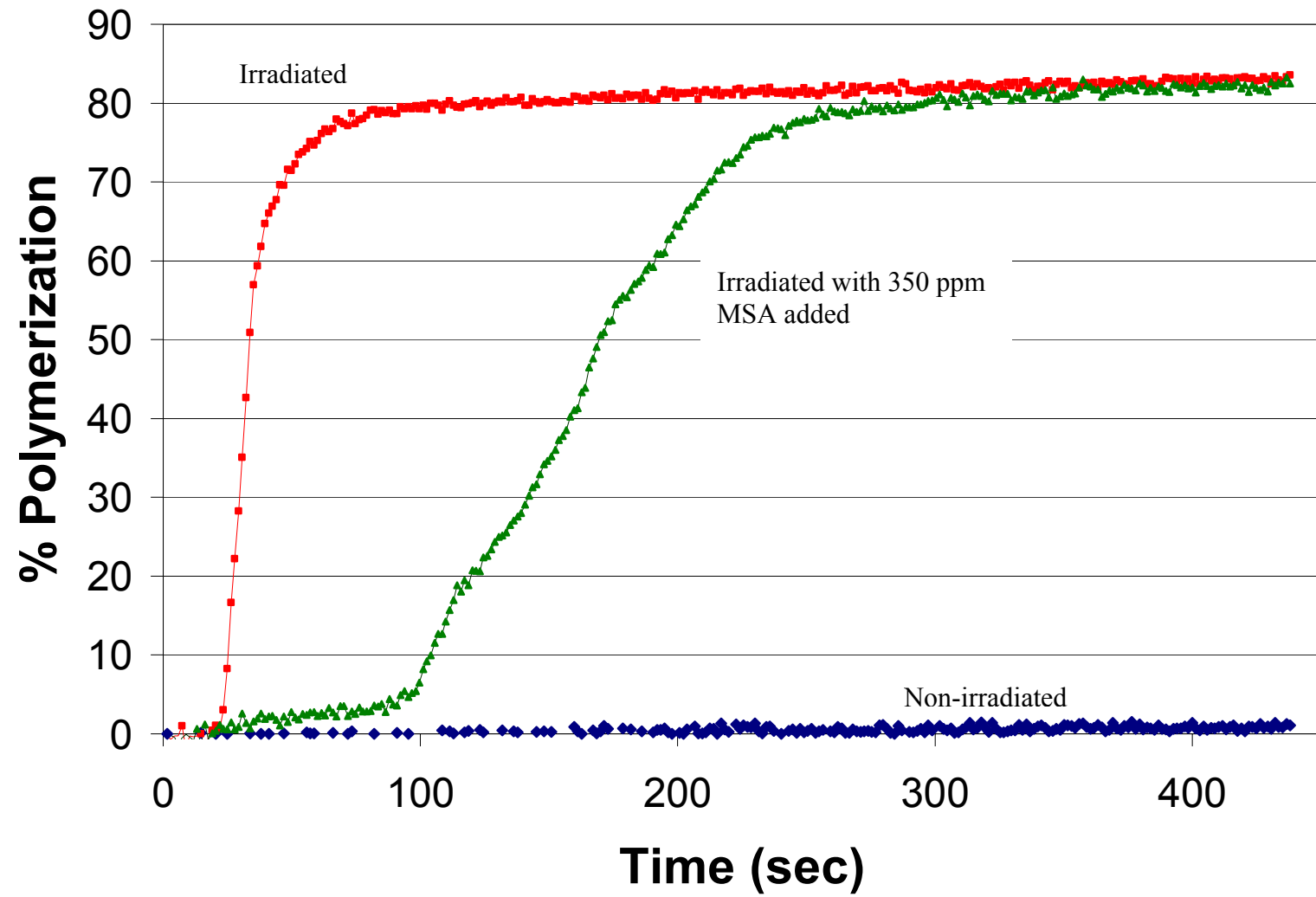


Figure IV-12. Mechanism of Metal-Ring Bond Cleavage of DFc. Illustration showing that ferrocene is photoinert in methanol while 1,1'-dibenzoylferrocene undergoes heterolytic metal-ring bond cleavage in this solvent to yield the benzoyl-substituted cyclopentadienide ion and the corresponding half-sandwich cationic complex.

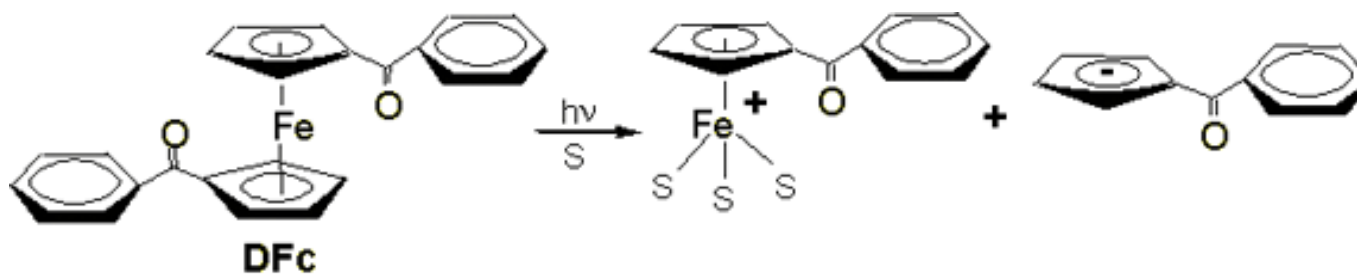
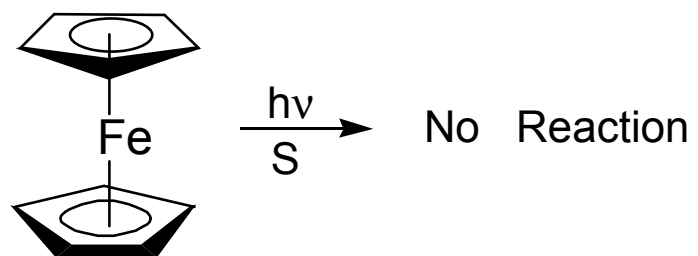
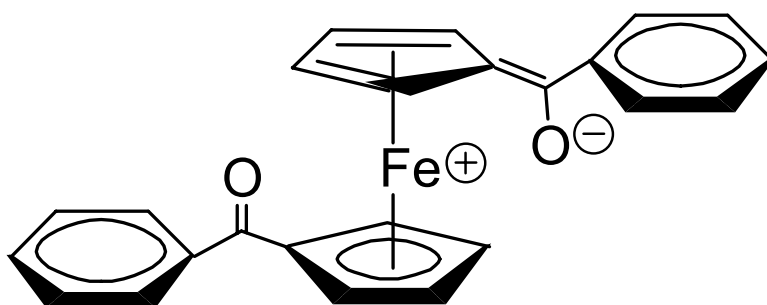


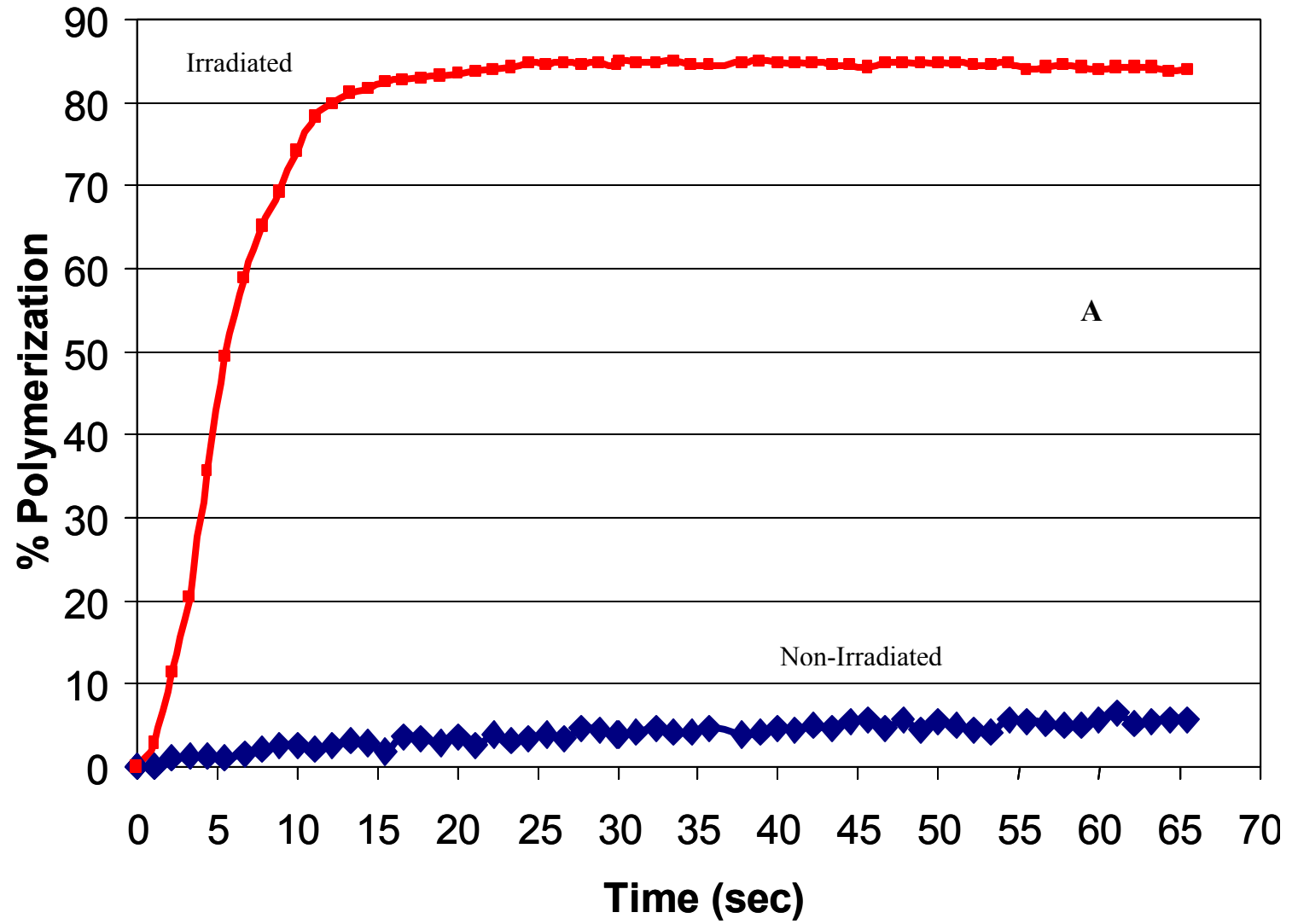
Figure IV-13. Resonance Structure of DFc. Resonance structure representing the charge transfer character that results from conjugation between the cyclopentadienide ring and the carbonyl group of the electronically excited DFc.

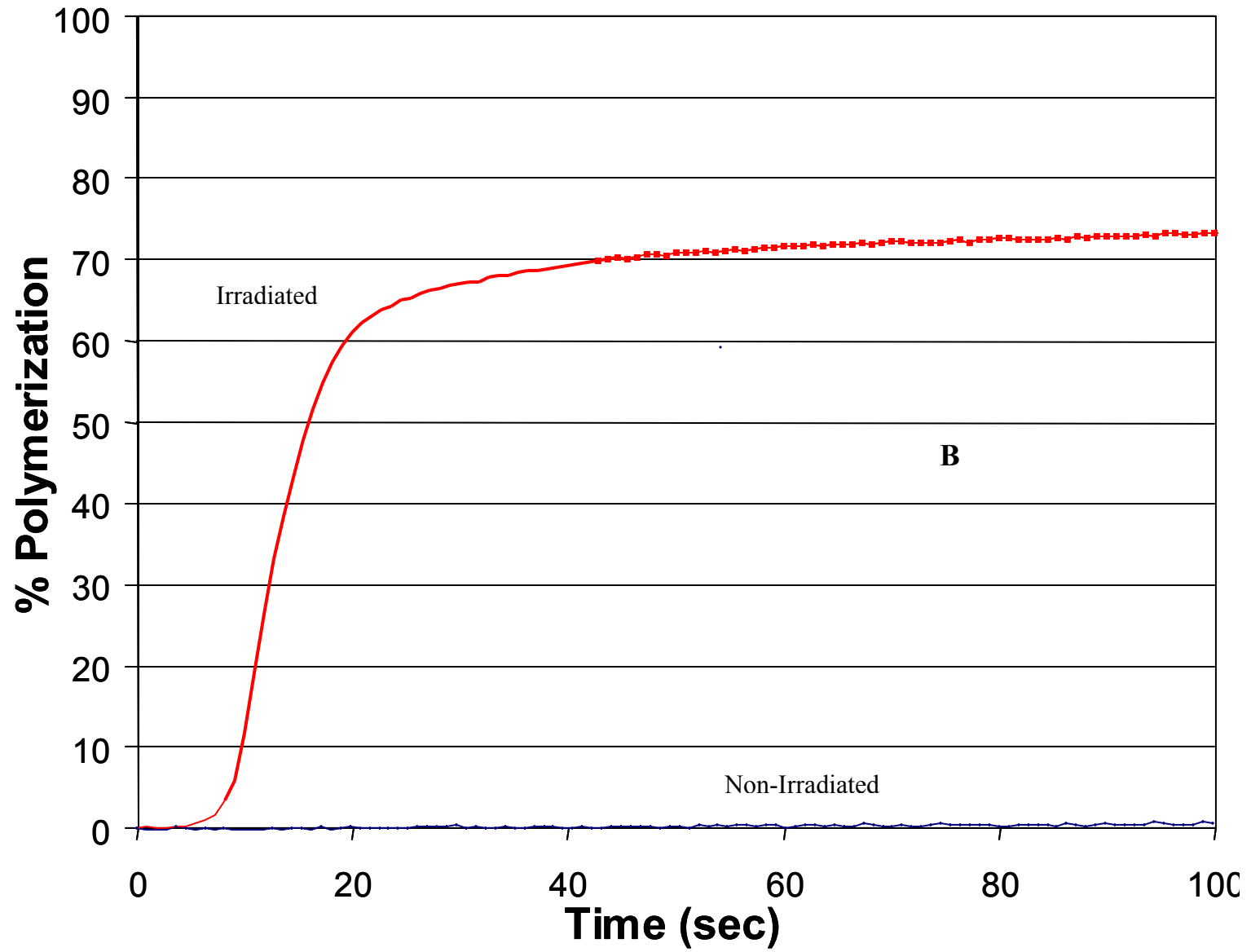


The sample solution of CA containing BFc was placed on the germanium crystal inside the sample compartment of the spectrometer. A spectrum of the sample solution was taken prior to irradiation and monitored for a period of 2 minutes. After acquisition of the dark scan, the sample was irradiated with the mercury arc lamp. The infrared absorbance collection was begun one second prior to the beginning of irradiation in order to acquire a “dark” spectrum for reference purposes. The benzoylferrocene (BFc) was treated in a similar manner, with the dark observation period being 180 seconds. Spectral behavior for the two samples were consistent with that witnessed previously for FeCp₂. However, a much faster polymerization time for both BFc and DFc was observed. Plots of polymerization versus time for BFc (figure IV-14A) and DFc (figure IV-14B) also exhibit a very short induction period followed by rapid polymerization of the sample. BFc reached a maximum polymerization percentage of ~73% in a period of 45 seconds, after this point the polymerization plateaus. DFc reached a maximum polymerization percentage of ~ 85% in a period of 20 seconds. The benzoyl substituted ferrocene samples proved to be much better photoinitiators than either FeCp₂ or RuCp₂. This is due to the cleavage of the ligand, as previously discussed. Having two substituted rings rather than the single substituted ring of the BFc enhances the performance of the DFc as a photoinitiator. Previous work by Yamaguchi and Kutal³⁹ support these findings.

Benzoyl substituted Ruthenocene as anionic photoinitiators. In comparing the increased performance of RuCp₂ versus FeCp₂ as an anionic photoinitiator, it was decided to investigate benzoylruthenocene (BRc) for similar performance characteristics compared to BFc. Using the same conditions described previously, samples of CA containing 10.5 mM BRc were placed on the germanium crystal and a monitored for a period of 10 minutes prior to irradiation. After acquisition of the dark scan, the sample was irradiated with the mercury arc lamp. Absorbance

Figure IV-14. (A). Plot of Polymerization versus Time for CA containing BFC. (B). Plot of Polymerization versus Time for CA containing DFC. Irradiated samples were exposed to 110 mW/cm² of polychromatic light from a high-pressure mercury lamp.





spectra were collected until no change in the collected spectra was observed (~600 seconds). Absorbance spectra were similar to those illustrated previously, with the disappearance of the C=C peak during the irradiation period. Figure IV-15 shows the plot of polymerization versus time for the BRc. As seen in all of the previous data, there is a slight induction period followed by rapid polymerization. The polymerization reaches a plateau at ~ 65 % polymerization at the 350 second time. However, the majority of the reaction proceeds to ~ 53% polymerization in 20 seconds with the remaining 10% polymerization occurring over the next 6-7 minutes. In this particular instance, BRc did not reach the same percent polymerization as BFc although the reaction proceeded in the same time frame.

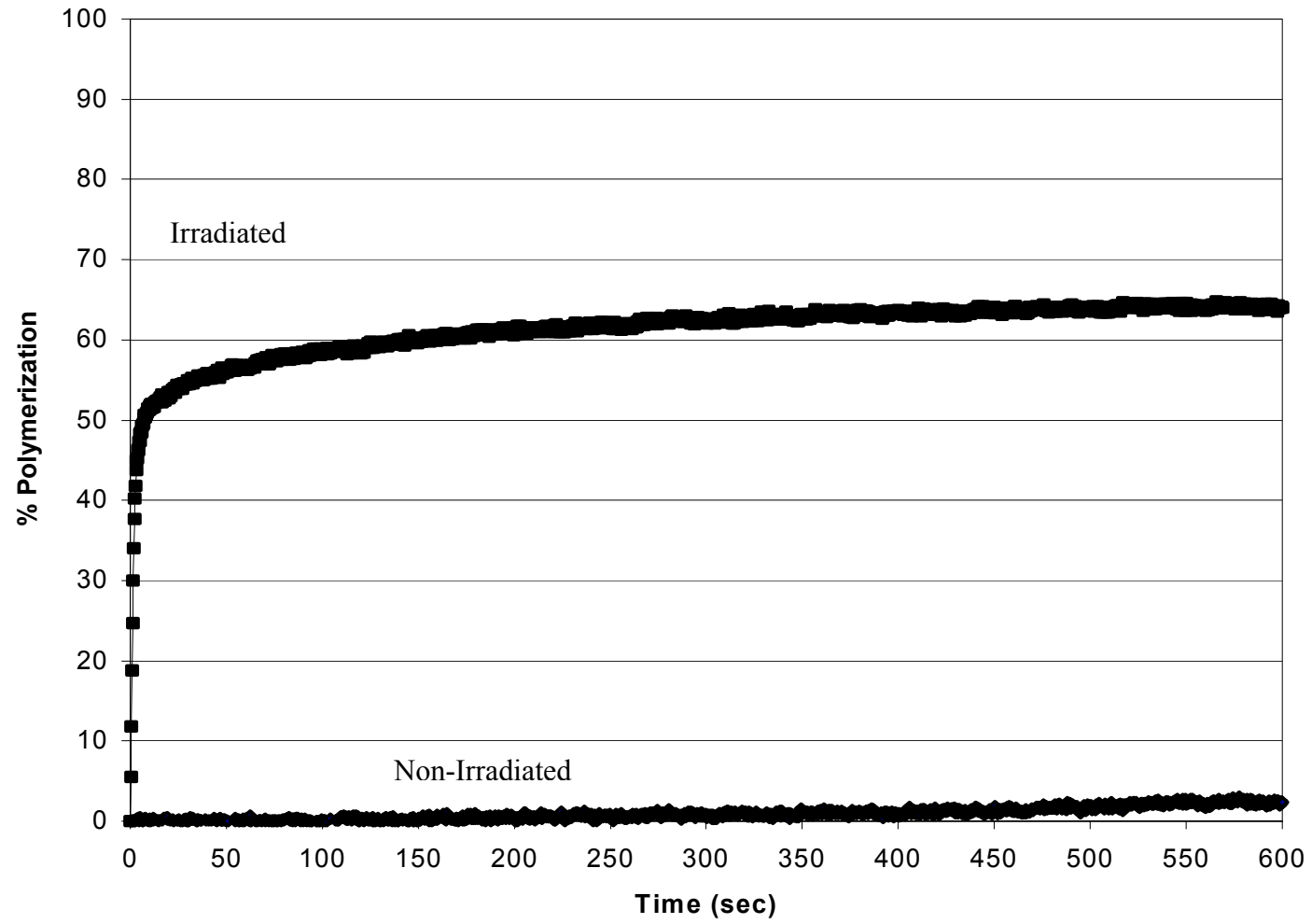
Conclusions

The results presented here demonstrate the effectiveness of metallocenes as anionic photoinitiators. Millimolar concentrations of the FeCp₂, RuCp₂, DFc, BFc, and BRc were sufficient for the photoinitiated polymerization of neat CA. This is a vast improvement over early ionic polymerization studies where a photosensitive D-A complex was formed.⁴⁰ In earlier work, the solvent served as the donor and was present in large excess, leading to a great deal of waste. The rapid polymerization with relatively low light levels makes the use of the metallocenes particularly appealing for industrial applications. They are particularly well suited for applications in the coatings and adhesives industries where solvent-free photosensitive formulations are required. The results presented here also demonstrate the advantages of real-time monitoring with HATR spectroscopy.

Acknowledgements.

Grateful thanks are extended to Cynthia Sanderson for the sample preparation.

Figure IV-15. Plot of Polymerization versus Time for CA containing BRC. Irradiated samples were exposed to 110 mW/cm^2 of polychromatic light from a high-pressure mercury lamp.



REFERENCES

1. Lai, Y.-C. and Quinn, E.T., *The Effects of Initiator and Diluent on the Photopolymerization of 2-Hydroxyethyl Methacrylate and on Properties of Hydrogels Obtained*, in *Photopolymerization Fundamentals and Applications*, A.B. Scranton, et al., Editors. 1997, American Chemical Society: Washington, DC. p. 242.
2. Szwarc, M. and Beylen, M.v., *Ionic Polymerization and Living Polymers*. 1993, New York: Chapman & Hall. 380.
3. Stevens, M.P., *Polymer Chemistry : An Introduction*. 3rd ed. 1999, New York: Oxford University Press. 551.
4. Hageman, H.J., *Photopolymerisation and Photoimaging Science and Technology*, in *Photopolymerisation and Photoimaging Science and Technology*, N.S. Allen, Editor. 1989, Elsevier Applied Science: London. p. 1-53.
5. Moad, G. and Solomon, D.H., *The Chemistry of Free Radical Polymerization*. 1st ed. 1995, New York: Tarrytown. 408.
6. Ding, W., *Mechanistic Study of Cationic Iron(III) Sandwich Complexes as Photoinitiators for Polymerization Reactions*, PhD. **2002**, Chemistry: University of Georgia, Athens
7. Reichmanis, E., et al., *Chemical Amplification Mechanisms for Microlithography*. *Chemistry of Materials*, **1991**. 3(3): 394-407.
8. Monroe, B.M. and Weed, G.C., *Photoinitiators for Free-Radical-Initiated Photoimaging Systems*. *Chemical Reviews*, **1993**. 93(1): 435-48.

9. Davidson, R.S., *The Chemistry of Photoinitiators - Some Recent Developments*. Journal of Photochemistry and Photobiology a-Chemistry, **1993**. 73(2): 81-96.
10. Belfield, K.D. and Crivello, J.V., eds. *Photoinitiated Polymerization*. Acs Symposium Series. 2003, Oxford University Press: Washington D.C.
11. Decker, C., *Photoinitiated Crosslinking Polymerisation*. Progress in Polymer Science, **1996**. 21(4): 593-650.
12. Kutal, C., *Generation of Bases and Anions from Inorganic and Organometallic Photoinitiators*. Coordination Chemistry Reviews, **2001**. 211: 353-68.
13. Geoffroy, G.L. and Wrighton, M.S., *Chapter 5*, in *Organometallic Photochemistry*. 1979, Academic Press: New York. p. 335.
14. Akiyama, T., et al., *Photochemical Substitution of Ferrocene in Halogenated Hydrocarbon-Ethanol Solutions*. Bulletin of the Chemical Society of Japan, **1973**. 46(6): 1851-54.
15. Traverso, O., et al., *Role of Excited-States in Photochemical Behavior of Ruthenocene in Halocarbon Solvents*. Inorganica Chimica Acta, **1974**. 11(3): 237-41.
16. Borrell, P. and Henderson, E., *Photochemistry of Charge-Transfer Complex between Ruthenocene and Carbon-Tetrachloride*. Journal of the Chemical Society-Dalton Transactions, **1975**(5): 432-38.
17. Bergamini, P., et al., *Radical-Forming Electron-Transfer - Photoreactions Involving Iron Group Metallocenes*. Journal of Organometallic Chemistry, **1989**. 365(3): 341-46.
18. Wight, F.R., *Oxygen Inhibition of Acrylic Photo-Polymerization*. Journal of Polymer Science Part C-Polymer Letters, **1978**. 16(3): 121-27.
19. Crivello, J.V. and Lam, J.H.W., *Dye-Sensitized Photoinitiated Cationic Polymerization*. J. Polym. Sci. Pol. Chem., **1978**. 16(10): 2441-51.

20. Crivello, J.V. and Lam, J.H.W., *Dye-Sensitized Photoinitiated Cationic Polymerization - System - Perylene-Triarylsulfonium Salts*. J. Polym. Sci. Pol. Chem., **1979**. 17(4): 1059-65.
21. Tryson, G.R. and Shultz, A.R., *Calorimetric Study of Acrylate Photo-Polymerization*. Journal of Polymer Science Part B-Polymer Physics, **1979**. 17(12): 2059-75.
22. Decker, C. and Fizet, M., *Laser-Nephelometry Investigation of Fast Proceeding Photopolymerizations*. Makromolekulare Chemie-Rapid Communications, **1980**. 1(10): 637-42.
23. Kloosterboer, J.G., et al., *The Effects of Volume Relaxation and Thermal Mobilization of Trapped Radicals on the Final Conversion of Photopolymerized Diacrylates*. Polymer Communications, **1984**. 25(11): 322-25.
24. Kloosterboer, J.G. and Lijten, G., *Deuterium-Isotope and Oxygen Effects on the Rate of Photopolymerization of a Diacrylate*. Polymer Communications, **1987**. 28(1): 2-5.
25. Hoyle, C.E. and Trapp, M.A., *Low Pulsing Frequency Laser-Initiated Polymerization of Multifunctional Acrylates*. Journal of Imaging Science, **1989**. 33(5): 188-91.
26. Kloosterboer, J.G. and Lijten, G., *Photopolymers Exhibiting a Large Difference between Glass-Transition and Curing Temperatures*. Polymer, **1990**. 31(1): 95-101.
27. Crivello, J.V. and Lee, J.L., *The Synthesis, Characterization, and Photoinitiated Cationic Polymerization of Silicon-Containing Epoxy-Resins*. J. Polym. Sci. Pol. Chem., **1990**. 28(3): 479-503.
28. Decker, C. and Moussa, K., *Photopolymerization of Multifunctional Monomers in Condensed Phase*. J. Appl. Polym. Sci., **1987**. 34(4): 1603-18.
29. Decker, C., *Ultrafast Polymerization of Epoxy-Acrylate Resins by Pulsed Laser Irradiation*. J. Polym. Sci. Pol. Chem., **1983**. 21(8): 2451-61.

30. Collins, G.L. and Costanza, J.R., *Reactions of Uv Curable Resin Formulations and Neat Multifunctional Acrylates .2. Photoinitiated Polymerization of Neat 1,6-Hexanediol Diacrylate*. Journal of Coatings Technology, **1979**. 51(648): 57-63.
31. Sanderson, C.T., et al., *Classical Metallocenes as Photoinitiators for the Anionic Polymerization of an Alkyl 2-Cyanoacrylate*. Macromolecules, **2002**. 35(26): 9648-52.
32. Yang, D.B., *Kinetic-Studies of Photopolymerization Using Real-Time Ft-Ir Spectroscopy*. J. Polym. Sci. Pol. Chem., **1993**. 31(1): 199-208.
33. Rausch, M.D., et al., *The Aromatic Reactivity of Ferrocene, Ruthenocene and Osmocene*. Journal of the American Chemical Society, **1960**. 82(1): 76-82.
34. Harrick, N.J., *Internal Reflection Spectroscopy*. 1967, New York: John Wiley & Sons, Inc. 327.
35. Allen, N.S., et al., *Photopolymerization Activity of Perester Derivatives of Fluorenone and Benzophenone - a Real-Time Ftir and Differential Photocalorimetric Study*. Eur. Polym. J., **1990**. 26(9): 1041-47.
36. Allen, N.S., et al., *Photochemistry and Photopolymerization Activity of Perester Derivatives of Benzophenone*. J. Appl. Polym. Sci., **1991**. 42(5): 1169-78.
37. Murphy, M.R., et al., *Analysis of Photo-Initiated Polymerization in a Membrane Mimetic Film Using Raman Microscopy and Fourier Transform Infrared Spectroscopy*. Submitted to Langmuir, **2004**: Chapter III of dissertation.
38. Kutal, C., et al., *Harvesting the Fields of Inorganic and Organometallic Photochemistry for New Photoinitiators*, in *Photoinitiated Polymerization*, K.D. Belfield and J.V. Crivello, Editors. 2003, American Chemical Society: Washington DC.

39. Yamaguchi, Y. and Kotal, C., *Benzoyl-Substituted Ferrocenes: An Attractive New Class of Anionic Photoinitiators*. *Macromolecules*, **2000**. 33(4): 1152-56.
40. Irie, M., et al., *Photoinduced Ionic Polymerization .4. Anionic Polymerization of Nitroethylene in Tetrahydrofuran*. *Journal of Polymer Science Part B-Polymer Letters*, **1972**. 10(9): 699-&.

CHAPTER V

DEVELOPMENT OF A CUSTOM SAMPLING ACCESSORY FOR THE INVESTIGATION OF MONOMOLECULAR FILMS AT THE AIR-WATER INTERFACE USING RAMAN SPECTROSCOPY³

³ Murphy, M.R.; Krueger, P.; Dluhy, R.A. Data to be submitted for publication at a later date

Abstract

Unenhanced Raman spectroscopy has rarely been applied to studies of monolayers at the air-water interface due to the difficulties associated with the experiment. We have developed a novel sampling accessory to aid in the investigation of monomolecular films at the Air-Water interface using Raman Spectroscopy. This sampling accessory is comprised of a Delrin® trough fitted with a moveable barrier system to allow changes in surface pressure during collection of spectra. Optical lenses are incorporated into the design of the trough to allow for either total internal reflection (TIR) or external reflection sampling geometry. Surface pressure monitoring is accomplished through the use of the Wilhelmy technique with a microbalance mounted to the side of the trough and a Wilhelmy plate suspended slightly into the subphase inside the trough. The microbalance is interfaced to a controller unit that displays current pressure. The controller assembly is interfaced to a personal computer (PC) to allow changes in surface pressure as a function of trough area to be recorded. An automated water-leveling device consisting of a diode laser, feedback plates, a peristaltic pump, and water reservoir is used to maintain a constant subphase level. Channels cut into the trough allow for the addition of water without perturbing the film on its surface. The ability to maintain a constant subphase level ensures that the focal point for the collection optics remains the same throughout the duration of the experiment. To facilitate alignment of the trough, it is mounted to x,y,z positioning stages fitted with micrometers for precise adjustment. This custom designed accessory has enabled us to use a unique collection method for the analysis of monolayers at the Air-Water interface. While additional work needs to be completed, a spectrum of arachidic acid in the C-H stretching region is provided as proof of concept.

Introduction

A main objective of the Dluhy Research Group is to gain insight into the structure and function of pulmonary surfactant using a combination of spectroscopic and microscopic techniques. Historically, the group has studied Langmuir monolayer films as model systems.¹⁻⁷ The model systems are mixtures of 1,2-dipalmitoyl-*sn*-glycero-3-phosphocholine (DPPC), other phospholipids, and surfactant proteins at the Air-Water (A/W) interface. The study of these systems at this interface allows for a wide choice in the composition and physical state of the monolayer that are more biologically relevant than, for example, a monolayer on a solid surface. In characterizing model systems at the A/W interface, structural information may be obtained by pressure versus area isotherms, by Brewster angle and fluorescence microscopies, and by reflection and diffraction of X-rays and neutrons.⁸ However, this information should be correlated and complemented with direct molecular information gained from vibrational spectroscopy. Over the past 15 years, a great deal of effort has been made to enhance monolayer sensitivity of these vibrational techniques and reduce their limitations.⁹⁻¹¹ Infrared spectroscopy has been used extensively for this type of analysis, despite the difficulty of extracting the very weak monolayer signal from the strong absorptions of the water vapor environment that surrounds the experiment. However, conventional infrared reflection absorption spectroscopy (IRRAS) requires long acquisition times and accurate subtraction of the water vapor spectrum.

Pioneering work in the area of IRRAS performed by Dluhy and coworkers^{1, 2, 12-16} illustrates the potential of the technique to characterize a monolayer at the air-water interface. In addition to the use of IRRAS spectroscopy, sum frequency generation has also been used in the study of such monolayers.^{17, 18} Raman spectroscopy is especially promising for studying Langmuir films since it is sensitive to the internal and local molecular structure, as well as the

chemical nature of the molecule and its environment. Raman is also a desirable counterpart to SFG and IRRAS due to the complementary information that it provides, especially in the Amide III region. However, due to the intrinsically low scatter from the Raman phenomenon, the technique has not been widely applied to thin organic films. The majority of its applications have been through the use of enhancement techniques such as the addition of colloids to the subphase¹⁹⁻²²

Indeed, there have been few reported cases of the use of unenhanced Raman spectroscopy for the study of monolayer Langmuir-Blodgett films on various substrates.^{11, 23-25} There are even fewer groups who have met with success at the air-water interface using unenhanced Raman spectroscopy. Limited success has been reported in the study of deuterated surfactants in the $\nu(\text{CD})$ region in studies by Kawai and co-workers²⁶ and by Castaings and co-workers.²⁷ In the work by Kawai and associates, Raman spectra were acquired on a custom-built quartz trough using internal reflection excitation geometry. In their work, virtually no change was detected in alkyl chain order with increasing/decreasing surface pressures, which is in sharp contrast to similar work.^{1, 2, 12-16} In the fifteen years since the research by Kawai et al. was first reported, no further studies using this approach have appeared in the literature. The work by Castaings and co-workers utilized a LN_2 cooled CCD detector, holographic notch filters, and a confocal microscopy collection assembly to obtain spectra in the $\nu(\text{CD})$ region. The work they presented agrees with previously published data concerning ordering of the monolayer.^{1, 2, 12-16} However, no further examples have appeared since Castaings et al published their findings in 1996.

To facilitate our study of monomolecular films at the A-W interface, we have designed a custom sampling accessory. The accessory detailed in this paper has been manufactured to allow for two different sampling geometries to be used, thus increasing the chance for success. An

internal reflection geometry similar to that used by Kawai²⁶ is accomplished by incorporating a channel through the center of the trough for the incident laser at an angle 60° from vertical. External reflection at low incident angles is achieved through the use of an optic that allows light to be refracted through the water and dumped to eliminate excitation of the Delrin®. The moveable barrier system provides the option of increasing or decreasing the surface pressure, which allows for the study of changes in conformation and order with changes in pressure.

Materials and Methods

Reagents. Arachidic Acid (Matreya, Inc., Pleasant Gap, Pa.) was dissolved in chloroform at a final concentration of 1 mg/mL. Monomolecular films of arachidic acid were formed by spreading the arachidic acid solution onto the air-water interface of the custom trough assembly. The film was allowed to equilibrate for 10 minutes prior to compression and acquisition of spectra was begun. The subphase consisted of 18.3 M Ω /cm distilled water from a Barnstead Nanopure system. The subphase was at room temperature ($\sim 22^\circ\text{C}$).

Instrumentation. Excitation. A Coherent Radiation Innova 305 Ar⁺ continuous wave laser (Coherent, Santa Clara, Ca.) provided the excitation radiation at 514.5nm. The laser radiation was filtered using a 514.5 nm holographic bandpass filter (Kaiser Optical Systems Inc., Ann Arbor, Mi.) to ensure beam quality. The beam was steered to the sample interface using zerodur laser mirrors (Newport Optics, Irvine, Ca.). Typical laser power at the sample was $\sim 1.5 - 2.0$ W/cm².

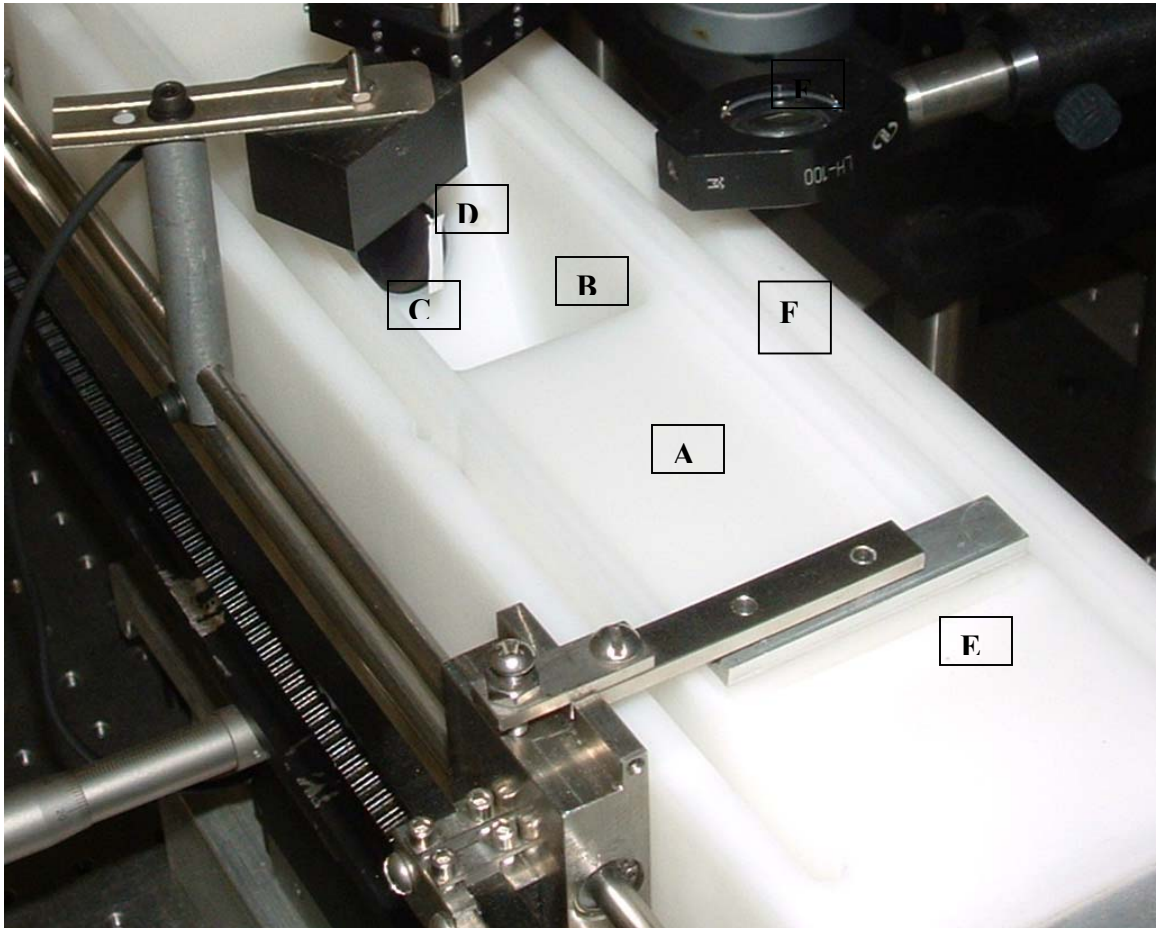
Raman Spectrometer. Raman Spectra were collected on an ISA 500M f/4 0.5-meter single spectrometer equipped with a Spectrum One CCD2000 charge-couple device detector

(Instruments SA, Edison, NJ). The CCD chip (SITE ST-005A) was 2000 x 800 pixels in size, back-illuminated, with an individual pixel size of 15 μm . The detector was liquid-nitrogen-cooled to a temperature of $-140\text{ }^{\circ}\text{C}$ and was backthinned giving a quantum efficiency of 85% at 550 nm. The grating used in the spectrometer had 1200 grooves/mm with a blaze wavelength of 750 nm; the slit width used in this experiment was 0.30 mm. Acquisition time for the arachidic acid film was 570 seconds with ten co-added scans. The collection optics used have been previously reported.¹¹

Software. All CCD spectral data were collected using the manufacturer-supplied SpectraMax for Windows software (Instruments SA, Edison, NJ). Post-processing of the Raman spectra was performed using *Grams32/AI* spectral software package (Galactic Industries (Nashua, NH). Baseline correction was performed on all spectra for clarity. Background water subtraction was performed using the spectral subtraction program contained within *Grams32/AI*.

Trough Assembly. The body and barriers of the trough were constructed of Delrin®. A maximum surface area of 14.61 cm^2 was available for film deposition. The maximum dimensions of the trough were 28.50 cm in length by 0.50 cm width. The minimum barrier position was 5.40 cm by 0.50 cm. The center portion of the compression area contains a V shaped well with a 60° slope on the walls and an open bottom, leading to channels along the sides of the trough. This sloping well allows for the placement of two focusing optics. The optics are positioned so that incoming radiation from the Ar^+ laser may be focused on the surface from an external 60° sampling geometry or by total internal reflection if steered from below the trough through the focusing optic on the sloping well. A photograph of the trough (Figure V-1) illustrates the sloping well and inset optics. When the external sampling geometry is used, the

Figure V-1. Photo of Custom Trough Assembly Showing Components **A.** Surface area of trough where sample is deposited to form monomolecular film. **B.** Sloping well area that works in conjunction with channels in the side of the trough for addition of water to the subphase without sample perturbation. **C.** Wilhelmy Plate, used in conjunction with microbalance to determine surface pressure of film. **D.** Focusing lens used for exit of beam from trough both in total internal reflection and in external sampling geometries. **E.** Moveable barriers that allow for compression of film to different surface pressures. **F.** Channels cut into side of trough and joined to center well area through an open channel at the bottom of the trough. This configuration allows for water leveling of the subphase without perturbing the film on the surface of the trough.

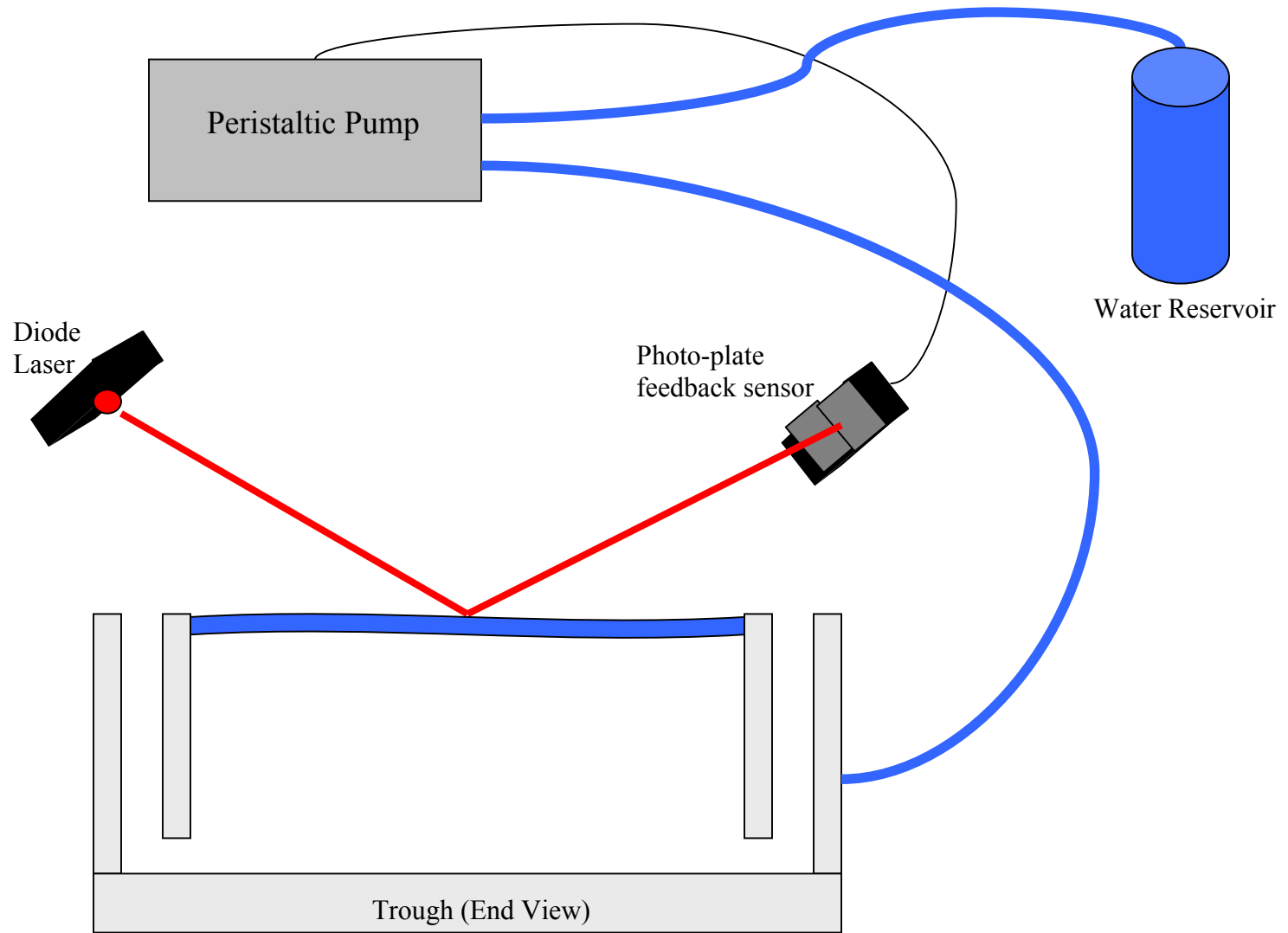


lens shown in the photo serves as a beam dump as the laser is refracted through the water and passes through the lens and out of the trough assembly.

The rail assembly used for barrier movement was manufactured of stainless steel while the motor mount itself was manufactured of brass. Attachment to the trough was accomplished through inset anchors and aluminum plates. The barriers, which were also made of Delrin®, utilized a stepping motor (Maxon Precision Motors Inc., Burlingame, Ca.) and planetary gearhead for smooth compression. To measure surface pressure changes as the barriers are expanded or compressed, the Wilhelmy technique is used. A microbalance is connected to an external controller, which displays the current surface pressure. A Wilhelmy plate is suspended from the microbalance with a portion of the plate submerged in the subphase. The plate is either buoyed upward or pulled downward as the surface pressure changes. This change in force exerted on the Wilhelmy plate is read by the microbalance and displayed by the controller.

To maintain the correct focal point throughout the duration of the experiment, a water-leveling device was constructed in-house. The device works by reflecting a diode laser beam off the water (subphase) surface onto two photo-plates. The two photo-plates are wired into a feedback circuit on a peristaltic pump. When the beam from the diode is centered between the two plates, the pump is off. If the beam is below center, the pump moves in the forward direction in order to add water until the subphase level is raised and the diode beam is positioned between the two plates again. If the beam is above center, the pump runs in reverse and water is removed. Although this device has not been tested to ascertain its exact accuracy, it is theoretically accurate to 1 μL . A diagram illustrating the leveling assembly can be seen in Figure V-2. To prevent perturbation of the film floating on the subphase, a separate channel area was incorporated into the trough for addition and removal of water. This channel is connected to the

Figure V-2. Cartoon of Water Leveling Device.



main area of the trough through an opening at the bottom of the V-shaped well. This allows for water leveling without a stream of water pushing against the surface film.

Internal Reflection Geometry. Based on work by Kawai, Castaings, and their respective co-workers,^{26, 27} we decided to use an internal reflection geometry for excitation and collection. Our trough assembly uses a unique approach to this sampling geometry. Rather than a window in the bottom of a flat trough, we incorporate a focusing optic into the V-shaped well of the trough and a window into the opposite wall to allow the beam reflected from the water surface to exit the trough (figure V-3). The angle of the wall is 60° , which allows the incident beam from the Ar^+ laser to strike the surface below the critical angle and be reflected off of the water surface and out of the window on the opposite angled wall without exciting the Delrin®. The resulting scattered radiation is collected by the fiber optic interface previously described.¹¹

Fatty Acid Monolayer spectrum. The initial sample used for study on the custom trough assembly was a model fatty acid system comprised of arachidic acid on water, in order to repeat previously published unenhanced Raman spectra²⁷ at the A-W interface. In this previous work deuterated arachidic acid was used because the strong OH stretching bands of water do not overlap with the $\nu(\text{C-D})$ stretching region. However, we chose to study the protonated acid as our intention was to progress to the study of readily available protonated phospholipids, and to subtract a background spectrum to remove the water contributions. An advantage to our approach is that the $\nu(\text{C-H})$ stretching region can yield up to twice the signal of the $\nu(\text{C-D})$ region.²⁸ An initial water spectrum was taken in the $\nu(\text{C-H})$ stretching region (figure V-4) to be used as a background for subtraction. After acquisition of the water background spectrum, a total

Figure V-3. Cutaway of Trough Assembly Showing TIR. View of trough assembly illustrating internal reflection sampling geometry and individual components: A. Moveable barriers B. Surface film area located between barriers C. Focusing optic to achieve maximum power density at sample position D. Channel in trough to allow incident laser beam to pass through E. Incident laser beam path for internal sampling geometry F. Channel at bottom of V-area to allow for smooth addition or removal of subphase without perturbation of surface film.

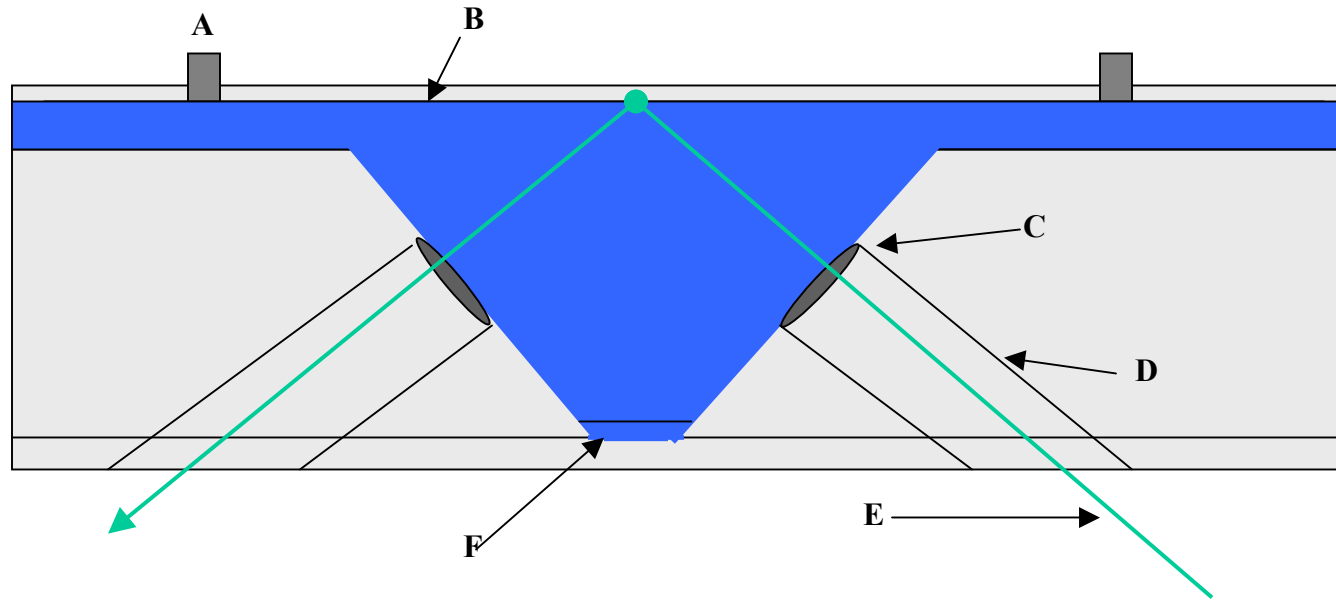
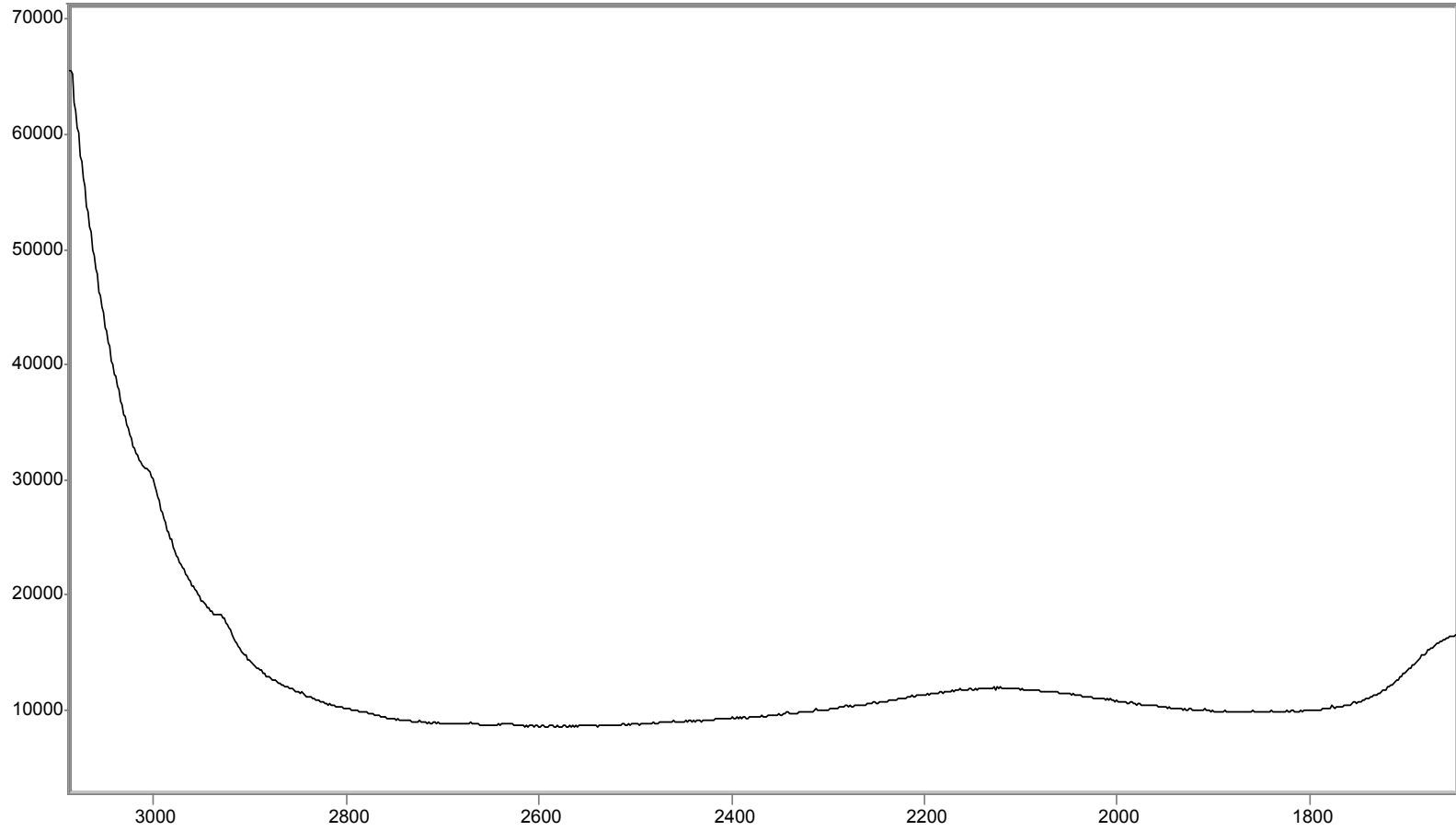


Figure V-4. Raman spectrum of water in the C-H stretching region. Used for background subtraction.



Counts / Raman Shift (cm-1)

File # 1 : 1202BK~1

Paged Y-Zoom CURSOR

Res=None

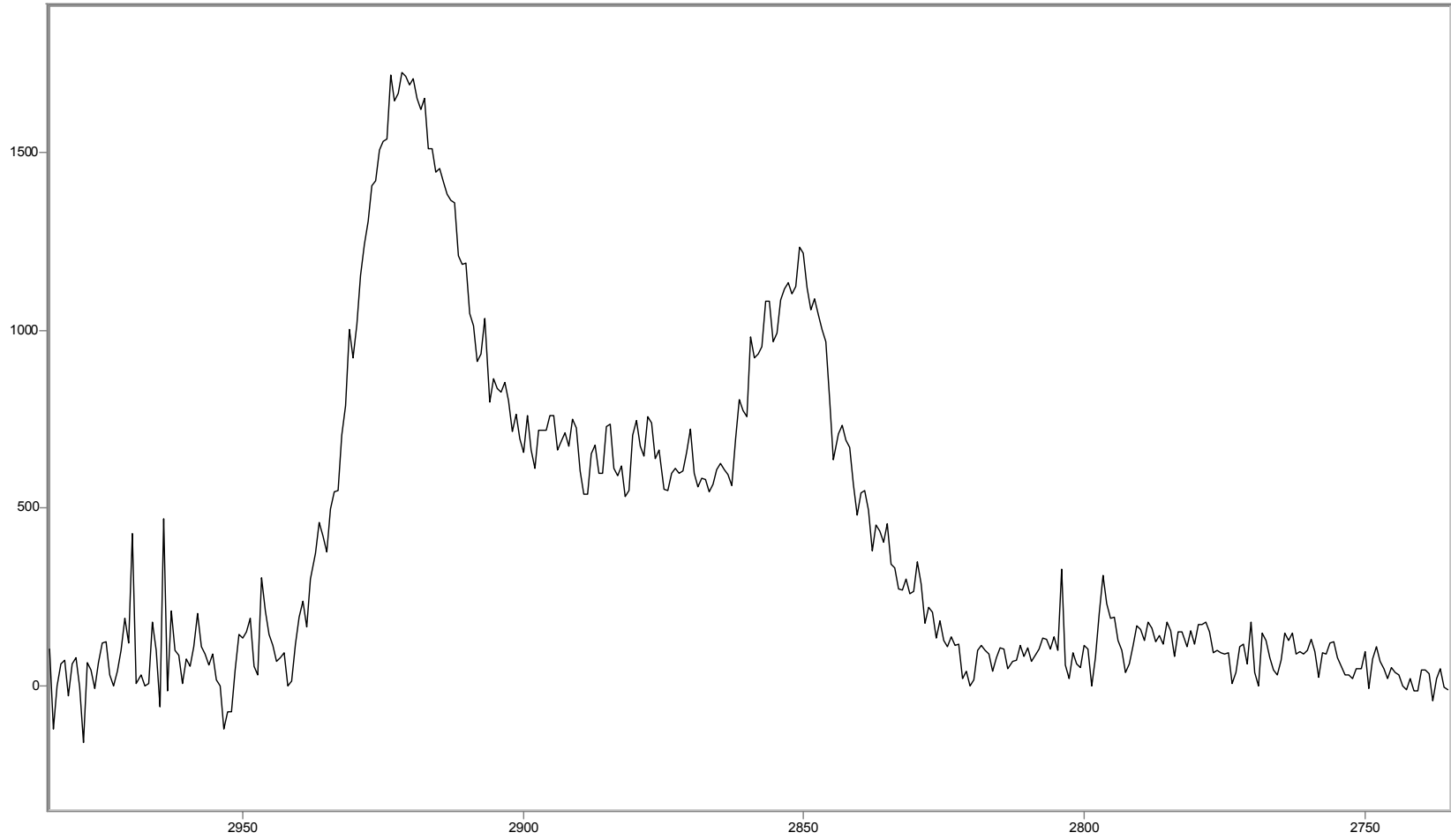
volume of 12 μL of 1mg/mL arachidic acid solution was added to reach a starting pressure of 11.2 mN/cm². The area of the trough was 14.61 cm² and this quantity of material corresponds to an approximate area per molecule of $\sim 6 \text{ \AA}^2$. The figure in the previously published work was 20 \AA^2 , which is the value of a closed-packed highly ordered film. The film was allowed to equilibrate for a period of 10 minutes and a spectrum was obtained. Using the spectral subtraction program located within the *Grams 32/AI* software, the spectrum of water was subtracted from the newly obtained spectrum.

The resulting spectrum of the $\nu(\text{C-H})$ region reveals peaks at 2930 cm⁻¹ and 2850 cm⁻¹ (figure V-5). These correspond to the Fermi resonance band $\nu_s(\text{CH}_2) + 2\delta(\text{CH}_2)$ and the d⁺ symmetric methylene $\nu_s(\text{CH}_2)$, respectively. The band intensities and peak positions of the vibrations present in the Raman $\nu(\text{C-H})$ stretching region are a complicated function of both interchain lateral packing and intrachain conformational order of the hydrocarbons.²⁹⁻³¹ A large enhancement of the Fermi resonance band is observed, which is indicative of a very conformationally disordered system, and which is mainly caused by the presence of gauche defects in the alkyl chains.²⁷ A Raman band parameter (R_1) may be defined that is the ratio of the integrated intensities of the 2930 cm⁻¹ band and the 2850 cm⁻¹ band. This ratio,

$$R_1 = \frac{I(\nu_s \text{CH}_2)}{I(\nu_s \text{CH}_2 + 2\delta \text{CH}_2)} \quad (\text{V-1})$$

should decrease with an increase in population of gauche structures.^{32, 33} A ratio of 0.63 was observed, which agrees with data found in previously published work based on system.²⁷ This value indicates a very unorganized film, which would be expected for monolayer coverage. However, the d⁻ antisymmetric methylene stretch at 2880 cm⁻¹ is not readily apparent in the spectra from our film. The overlapping peaks in this region are most likely obscuring this band.

Figure V-5. Arachidic Acid Monolayer. Resulting spectrum after subtraction of water background for arachidic acid in the $\nu(\text{C-H})$ region.



Counts / Raman Shift (cm-1)

Paged X-Zoom CURSOR

File # 1 : ARACHIDIC ACID MONO 1203ARF

Res=None

If a baseline is chosen between the bands at 2930 cm^{-1} and 2850 cm^{-1} , a relative measure of the d antisymmetric band at 2880 cm^{-1} may be taken and the ratio of the band at 2880 cm^{-1} to the band at 2850 cm^{-1} may be made. The value obtained for this ratio is .55, which also indicates a very disorganized chain. These measurements along with the mathematical calculations for monolayer coverage verify that the spectrum obtained is that of a monolayer film of arachidic acid.

A large amount of structural information is available in the $\nu(\text{C-C})$ region despite the low intensity of the vibrational bands found there. So, following the success in the C-H region, we decided to obtain spectra from the arachidic acid monolayer in this region. The proximity of the bulk water band located at $\sim 1600\text{ cm}^{-1}$ caused problems in this region, so a short pass filter was incorporated into the collection optics to effectively block all spectral data above $\sim 1600\text{ cm}^{-1}$. This allowed for an order of magnitude increase in the integration time to 900 seconds. Unfortunately, we were still unable to acquire the weak signal in this region despite the rather lengthy acquisition time of fifteen minutes. In order to acquire spectra in this region, as in the $\nu(\text{C-H})$ region, much longer integration times will be necessary. The need for longer integration times necessitates the reduction in background signal from the subphase.

Deuterated Phospholipid Analysis

To address the water background issue, it was decided to assess the viability of analysing deuterated compounds to avoid interference from the water subphase in the $\nu(\text{C-H})$ region. DPPC_{d62} at a concentration of 1mg/mL was used as a sample under the same conditions previously used for analysis of the $\nu(\text{C-H})$ stretching region. Despite being able to increase the integration times in this region to 700 seconds due to lower water background levels, it was not long enough to acquire any data with the current instrumental setup. A much longer integration time is required for deuterated samples than protonated samples, as the oscillating C-D bond is a

much weaker Raman scatterer than the C-H bond, and the gain from reducing the water background was more than offset by the loss in Raman signal. It was decided to return to protonated samples and move onto the work with varying surface pressures.

CHANGING SURFACE PRESSURES OF ARACHIDIC ACID FILMS

Since we had most success with our current set up when looking in the $\nu(\text{C-H})$ stretching region of spectra from protonated compounds, we decided to return to the model protonated fatty acid system in order to study the effects of varying surface pressures. Beginning with a pressure of 11 mN/cm^2 , the film was compressed at a rate of $0.025\text{-cm}^2 \text{ s}^{-1}$ to a final pressure of 33 mN/cm^2 . An immediate drop in surface pressure to 3 mN/cm^2 was observed when compression stopped. This is normally indicative of film collapse. However, such a sharp drop in pressure without a corresponding return to starting pressure upon expansion indicates that there was a loss of film material. Since arachidic acid is insoluble in water, we believe that the loss of material was due to spillover onto the rails of the trough.

One possible explanation for this is that the Delrin® material that the trough is manufactured from is hydrophilic in nature. Several companies use Delrin® as a material for the moveable barriers. The reason for using Delrin® as a barrier material at different surface pressures is illustrated in figure V-6A and B. In order to avoid film leakage over the edges of the trough, the surface level of the subphase should be kept as low as possible. At low surface pressures either hydrophilic or hydrophobic surface barriers may be used (figure V-6A). However, high pressures force the polar, hydrophilic ends of the molecules against the barrier, and if the barrier is made hydrophobic material the film starts to slide under the barrier. With a hydrophilic barrier the polar ends of the molecules stick to the barrier surface and no sliding will occur.

Figure V-6. **(A)**. Film behavior at low surface pressure with different barrier materials. **(B)**. Film behavior at high surface pressures with different barrier materials. High pressure forces the polar, hydrophilic ends of the molecules against the barrier and if the barrier is made of a hydrophobic material, the film starts to slide under the barrier. With a hydrophilic barrier the polar ends of the molecules stick to the barrier surface and no sliding will occur.

A.



Hydrophilic Barrier (Delrin®) Hydrophobic Barrier (Teflon®)

B.



Hydrophilic Barrier (Delrin®) Hydrophobic Barrier (Teflon®)

The barrier choice discussed above is contingent upon the remainder of the trough surface being manufactured from a hydrophobic material. Both our trough and our barriers are made from a hydrophilic material and it is our belief that as surface pressure increases and surface tension of the film decreases, the film escapes onto not only the barrier as seen in the illustration but also onto the edges of the trough. This results in loss of material and prevents us from using the moveable barriers to change surface area and pressure during spectral acquisition. One possible correction for this would be to make the lip area of the trough hydrophobic.

CONCLUSIONS

The data presented in this work shows that I have designed a suitable method of using unenhanced Raman spectroscopy for the analysis of monomolecular films at the A-W interface. The custom trough assembly with dual sampling geometries and incorporation of useful features such as a surface pressure measurement device, external controller, and moveable barrier system, provides us with a unique means of investigating such systems. With small modifications to the trough, I believe it will also be possible to obtain data whilst changing the surface pressure with the moveable barriers. Once these modifications have been made, surface pressure versus area isotherms can be obtained that will allow accurate calculation of area per molecule and surface coverage.

FUTURE WORK

The design of the trough assembly has aided in the acquisition of a monolayer spectrum at the air-water interface. However, as discussed previously, the hydrophilic nature of the trough has created problems with film manipulation. A great deal of expense would be incurred having a completely new trough manufactured. Indeed, only a small area of the trough need be

retrofitted with hydrophobic material. The rails of the trough and the upper surface area may be covered in Teflon®, while the V-shaped portion of the assembly containing the optics could remain in its present state. A short-term solution would be to cover the lip of the trough with a sheet of Teflon® film. A long-term solution would be to manufacture a semi rigid piece of Teflon® to cover the lip area of the trough. This would mean a slight narrowing of the trough, but would eliminate the possibility of a bubble forming underneath the sheeting or of accidental tearing during cleaning or adjustment. An experiment using changing surface pressures could then be carried out quite easily. Additional work must also go into reducing background signal so longer integration times can be used.

ACKNOWLEDGEMENTS

Grateful thanks are extended to Dr. Peter Krüeger for his assistance in the fabrication of the water leveling system and the barriers. The National Institutes of Health provided funding for this project.

REFERENCES

1. Dluhy, R.A. and Cornell, D.G., *In Situ Measurement of the Infrared Spectra of Insoluble Monolayers at the Air-Water Interface*. Journal of Physical Chemistry, **1985**. 89(15): 3195-97.
2. Dluhy, R.A., et al., *Infrared Spectroscopic Investigations of Pulmonary Surfactant - Surface-Film Transitions at the Air-Water-Interface and Bulk Phase Thermotropism*. Biophysical Journal, **1989**. 56(6): 1173-81.
3. Elmore, D.L. and Dluhy, R.A., *Pressure-Dependent Changes in the Infrared C-H Vibrations of Monolayer Films at the Air/Water Interface Revealed by Two-Dimensional Infrared Correlation Spectroscopy*. Applied Spectroscopy, **2000**. 54(7): 956-62.
4. Elmore, D.L. and Dluhy, R.A., *Application of 2d Ir Correlation Analysis to Phase Transitions in Langmuir Monolayer Films*. Colloids and Surfaces a-Physicochemical and Engineering Aspects, **2000**. 171(1-3): 225-39.
5. Elmore, D.L., et al., *A Study of Binary Phospholipid Mixtures at the Air-Water Interface Using Infrared Reflection-Absorption Spectroscopy and 2d Ir Beta V Correlation Analysis*. Journal of Physical Chemistry A, **2002**. 106(14): 3420-28.
6. Wilkin, J., et al., *Spectroscopy & Microscopy of Aqueous Lipid Monolayers with Applications to Pulmonary Surfactant: Ir and Fluorescence Studies*. Biophysical Journal, **1997**. 72(2): MP271-MP71.

7. Kruger, P., et al., *Effect of Hydrophobic Surfactant Peptides Sp-B and Sp-C on Binary Phospholipid Monolayers. I. Fluorescence and Dark-Field Microscopy*. Biophysical Journal, **1999**. 77(2): 903-14.
8. Blaudez, D., et al., *Infrared and Raman Spectroscopies of Monolayers at the Air-Water Interface*. Current Opinion in Colloid & Interface Science, **1999**. 4(4): 265-72.
9. Mendelsohn, R., et al., *External Infrared Reflection Absorption Spectrometry of Monolayer Films at the Air-Water Interface*. Annual Review of Physical Chemistry, **1995**. 46: 305-34.
10. Dluhy, R.A., et al., *Vibrational Spectroscopy of Biophysical Monolayers - Applications of Infrared and Raman-Spectroscopy to Biomembrane Model Systems at Interfaces*. Spectrochimica Acta Part A, **1995**. 51(8): 1413-47.
11. Leverette, C.L. and Dluhy, R.A., *A Novel Fiber-Optic Interface for Unenhanced External Reflection Raman Spectroscopy of Supported Monolayers*. Langmuir, **2000**. 16(8): 3977-83.
12. Dluhy, R.A., *Quantitative External Reflection Infrared Spectroscopic Analysis of Insoluble Monolayers Spread at the Air-Water Interface*. Journal of Physical Chemistry, **1986**. 90(7): 1373-79.
13. Dluhy, R.A., et al., *In Situ Measurement of the Ft-Ir Spectra of Phospholipid Monolayers at the Air Water Interface*. Applied Spectroscopy, **1988**. 42(1): 138-41.
14. Dluhy, R.A., et al., *Design and Interfacing of an Automated Langmuir-Type Film Balance to an Ft-Ir Spectrometer*. Applied Spectroscopy, **1988**. 42(7): 1289-93.
15. Mitchell, M.L. and Dluhy, R.A., *In Situ Ft-Ir Studies of Langmuir-Blodgett Monolayers*. Mikrochimica Acta, **1988**. 1(1-6): 349-52.
16. Hunt, R.D., et al., *The Interfacial Structure of Phospholipid Monolayer Films - an Infrared Reflectance Study*. Journal of Molecular Structure, **1989**. 214: 93-109.

17. Guyot-Sionnest, P., et al., *Sum-Frequency Vibrational Spectroscopy of a Langmuir Film - Study of Molecular-Orientation of a Two-Dimensional System*. Physical Review Letters, **1987**. 59(14): 1597-600.
18. Shen, Y.R., *Surface-Properties Probed by 2nd-Harmonic and Sum-Frequency Generation*. Nature, **1989**. 337(6207): 519-25.
19. Chamberlain, J.R. and Pemberton, J.E., *Raman Spectroscopy of Langmuir Monolayers at the Air-Water Interface*. Langmuir, **1997**. 13(12): 3074-79.
20. Hou, X.L., et al., *Self-Assembly and Langmuir-Blodgett (Lb) Film of a Novel Hydrogen-Bonded Complex: A Surface Enhanced Raman Scattering (Sers) Study*. Colloids and Surfaces a-Physicochemical and Engineering Aspects, **2002**. 198: 135-40.
21. Yui, H., et al., *Spectroscopic Analysis of Total-Internal-Reflection Stimulated Raman Scattering from the Air/Water Interface under the Strong Focusing Condition*. Chemical Physics Letters, **2002**. 360(1-2): 53-58.
22. Wu, S.X., et al., *Fourier Transform Surface-Enhanced Raman Scattering of Single-Layer Nucleolipid Langmuir-Blodgett Films on Silver Island Film Substrates*. Journal of Colloid and Interface Science, **2004**. 270(2): 309-14.
23. Choplin, F., et al., *Structural Characterization of Self-Assembled Monolayers by Unenhanced Raman Spectroscopy*. Journal of Raman Spectroscopy, **2003**. 34(11): 902-06.
24. Dierker, S.B., et al., *Characterization of Order in Langmuir-Blodgett Monolayers by Unenhanced Raman-Spectroscopy*. Chemical Physics Letters, **1987**. 137(5): 453-57.
25. Liu, Y.C. and McCreery, R.L., *Reactions of Organic Monolayers on Carbon Surfaces Observed with Unenhanced Raman-Spectroscopy*. Journal of the American Chemical Society, **1995**. 117(45): 11254-59.

26. Kawai, T., et al., *Non-Resonance Raman Studies on Spread Monolayers of Stearic Acid-D35 and Cadmium Stearate-D35 on Water Surfaces and Thin Lb Films*. Chemical Physics Letters, **1989**. 162(3): 243-47.
27. Castaings, N., et al., *Raman Spectroscopy of Lb Films and Monolayers at the Air-Water Interface*. Thin Solid Films, **1996**. 285: 631-35.
28. Haydock, S.A., *In Situ Vibrational Spectroscopy of Thin Organic Films Confined at the Solid-Solid Interface*, in *Physical Chemistry*. 2002, Oxford University: Oxford.
29. Snyder, R.G., et al., *Vibrational-Spectra in C-H Stretching Region and Structure of Polymethylene Chain*. Spectrochimica Acta Part a-Molecular and Biomolecular Spectroscopy, **1978**. 34(4): 395-406.
30. Snyder, R.G. and Scherer, J.R., *Band-Structure in the C-H Stretching Region of the Raman-Spectrum of the Extended Polymethylene Chain - Influence of Fermi Resonance*. Journal of Chemical Physics, **1979**. 71(8): 3221-28.
31. Snyder, R.G., et al., *C-H Stretching Modes and the Structure of Normal-Alkyl Chains .1. Long, Disordered Chains*. Journal of Physical Chemistry, **1982**. 86(26): 5145-50.
32. Zerbi, G. and Abbate, S., *Spectroscopic Determination of the Average Content of Gauche Structures in Organic-Molecules Containing Polymethylene Chains*. Chemical Physics Letters, **1981**. 80(3): 455-57.
33. Abbate, S., et al., *Fermi Resonances and Vibrational-Spectra of Crystalline and Amorphous Polymethylene Chains*. Journal of Physical Chemistry, **1982**. 86(16): 3140-49.
34. Okamura, E., et al., *High-Sensitivity Raman Spectroscopic Study on Surface-Pressure Dependence of the Structure in Thin Langmuir-Blodgett Films of Dipalmitoylphosphatidylcholine*. Journal of Raman Spectroscopy, **1991**. 22: 759-62.

CHAPTER VI

CONCLUSIONS

From the work presented in chapters III through V of this dissertation, the following conclusions are drawn:

1. The study of a membrane-mimetic film in Chapter III demonstrated Raman microscopy to be a viable alternative to FT-IR spectroscopic techniques for the analysis of percent polymerization. Raman offers the advantages of limited sensitivity to water interference and greater sensitivity to C=C stretching modes. We have verified this new methodology by comparing results obtained with Raman microscopy to those obtained with HATR FT-IR and achieving excellent agreement. This new method provides the researcher with an alternative technique for this type of analysis that may otherwise be impossible.
2. Chapter IV shows that the metallocenes, ferrocene and ruthenocene, along with their benzoyl-substituted counterparts are sensitive anionic photoinitiators. Due to the photoinduced cleavage of the ligand and having two substituted rings, DFc proved to be a superior photoinitiator compared to BFc. Both of these were superior photoinitiators to RuCp₂ and FeCp₂. Using real-time infrared analysis allows for quantitation of percent polymerization at any point during the process. Real-time analysis also allows for the determination of rate of reaction in the various samples.

3. A main objective of the Dluhy Research Group is to gain insight into the structure and function of pulmonary surfactant using a combination of spectroscopic and microscopic techniques. With the addition of the custom sampling accessory detailed in Chapter V, another method for the study of pulmonary surfactant has been made available. Raman spectroscopy of monomolecular films at the air-water interface has met with little success. The custom accessory, using total internal reflection and constant water level features has enabled us to acquire a monolayer spectrum of arachidic acid at the air-water interface. This is a significant accomplishment due to the information available through the Raman analysis of Amide III bands, which cannot be studied using current infrared techniques.

Through the work presented here and the work of others, Raman spectroscopy continues to find new applications and fulfill its potential as a powerful tool for the characterization of thin and monomolecular films. The continued success in implementing this technique provides researchers with an ever-expanding arsenal of weapons to use in thin film research.

Appendices

APPENDIX A

RAW DATA ANALYSIS METHODS FOR CHAPTER III

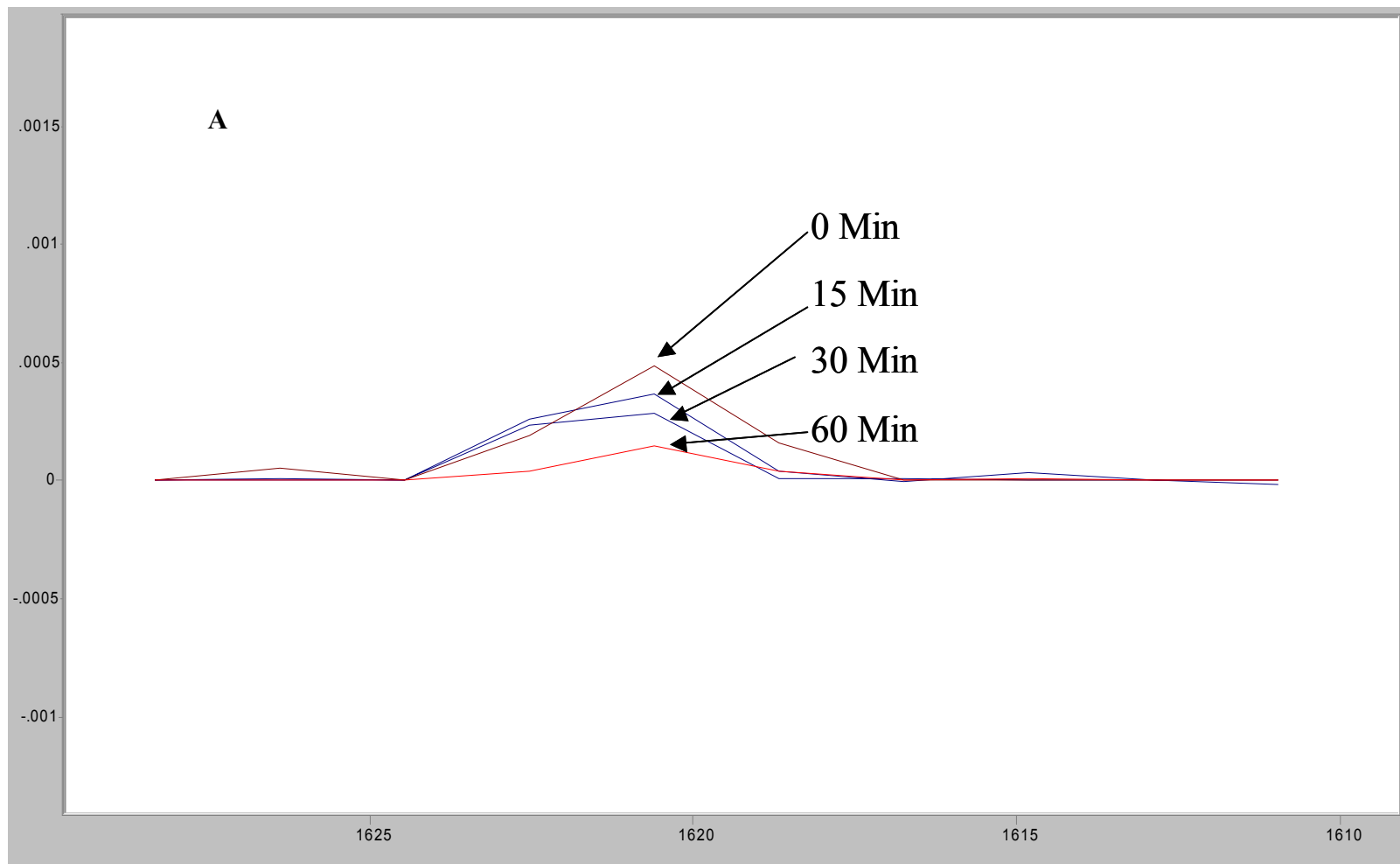
INTRODUCTION

To facilitate a better understanding of the analysis procedures undertaken in Chapter III, a discussion of the methods used and a presentation of the raw data follows. The data analysis is broken down into individual sections to follow the outline used in Chapter III. In some instances, it is necessary to combine the discussion of two or more sections for a comparison of the techniques and methodology used.

Quantitation of Photopolymerization in minimally hydrated lipid sample with white light irradiation by Infrared Spectroscopy. Sample analysis for the infrared spectra was conducted for both sets of data following baseline correction. For comparison purposes, the integrated area of the raw data (Figures A-1A,B and A-2A,B) and the integrated area of the same data after interpolation (Figure A-3A,B and A-4A,B) were determined. The area was determined using the center of gravity (COG) program written by David G. Cameron and outlined in *Applied Spectroscopy*, 36, 3, 245-250, **1982** and adapted for use in the Grams environment by R.A. Dluhy. The COG program operates in conjunction with the Grams32/AI software from Galactic industries. Interpolated data were obtained by using the FFT option in Grams32/AI and by choosing a 4x factor. However, in interpolating the data, the peak shape, center peak position, integrated area of the peak were changed substantially. For comparison purposes, the results of the analysis are displayed in Table A-1 and Table A-2. The average percent polymerization for

Figure A-1. (A) Sample 1 HATR data decrease in C=C band during irradiation. (B)

Sample 1 HATR data Ester Carbonyl Band during irradiation



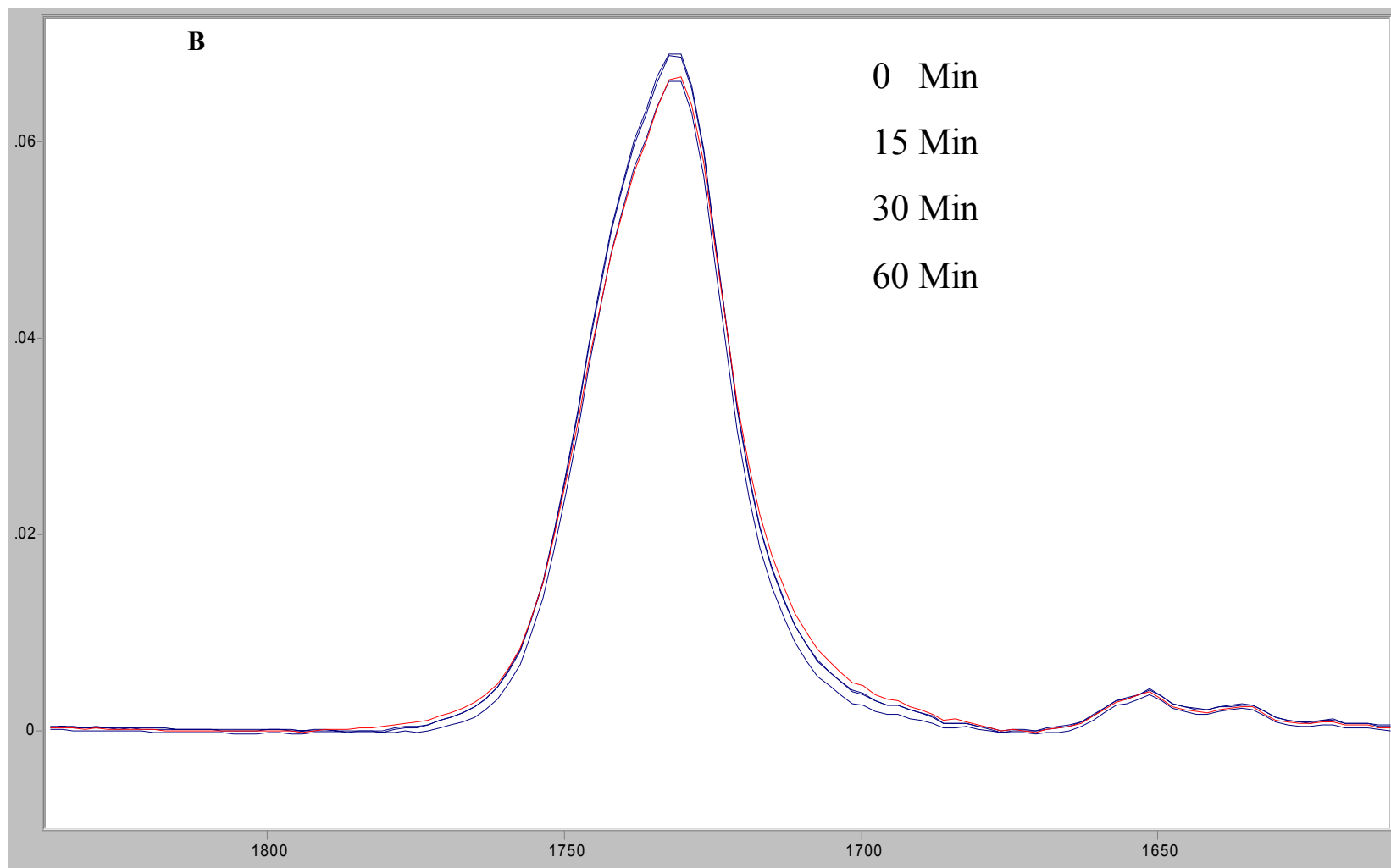
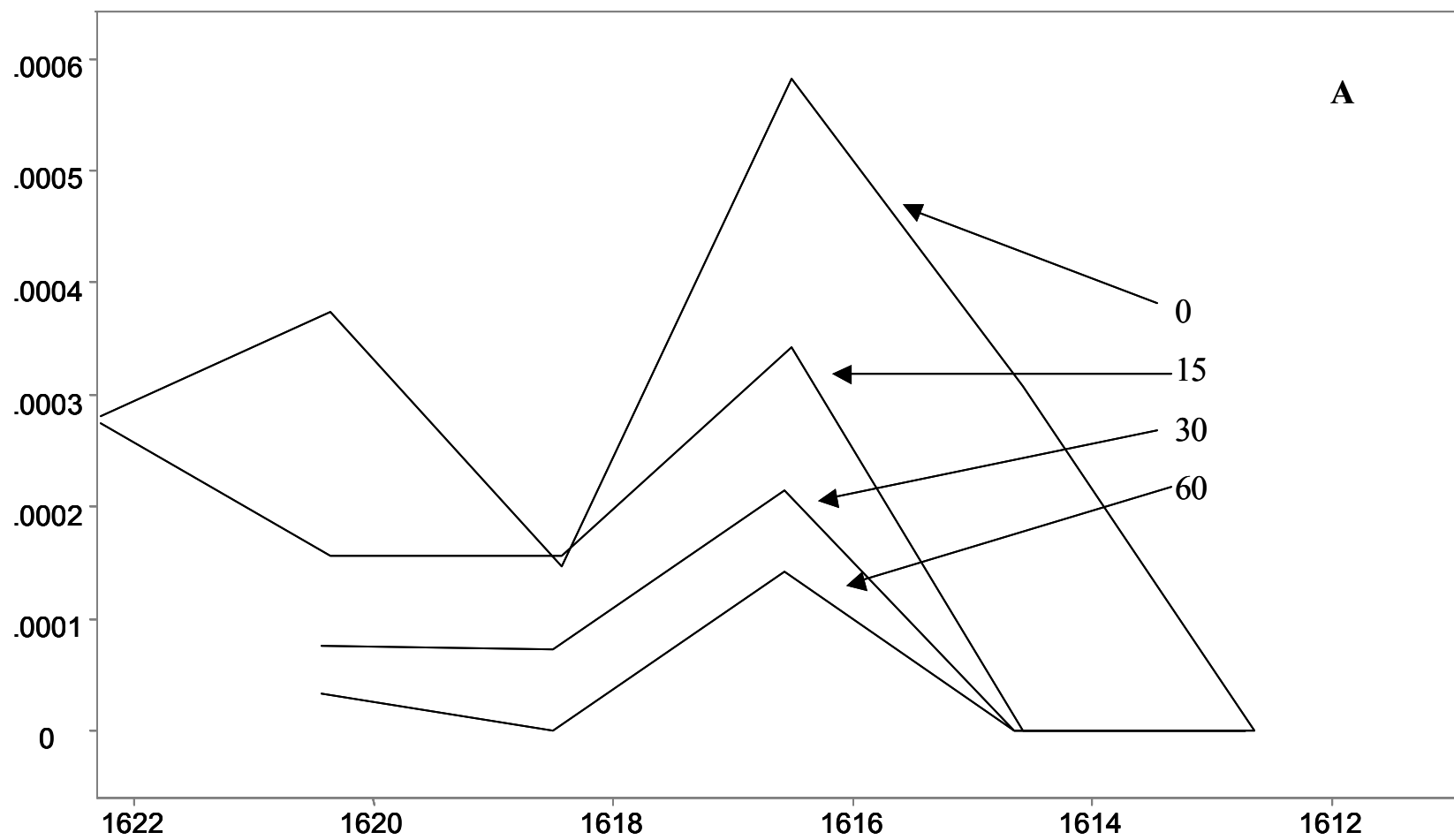


Figure A-2. (A) Sample 2 HATR decrease in C=C band during irradiation (B) Sample 2 HATR Ester Carbonyl Band during irradiation



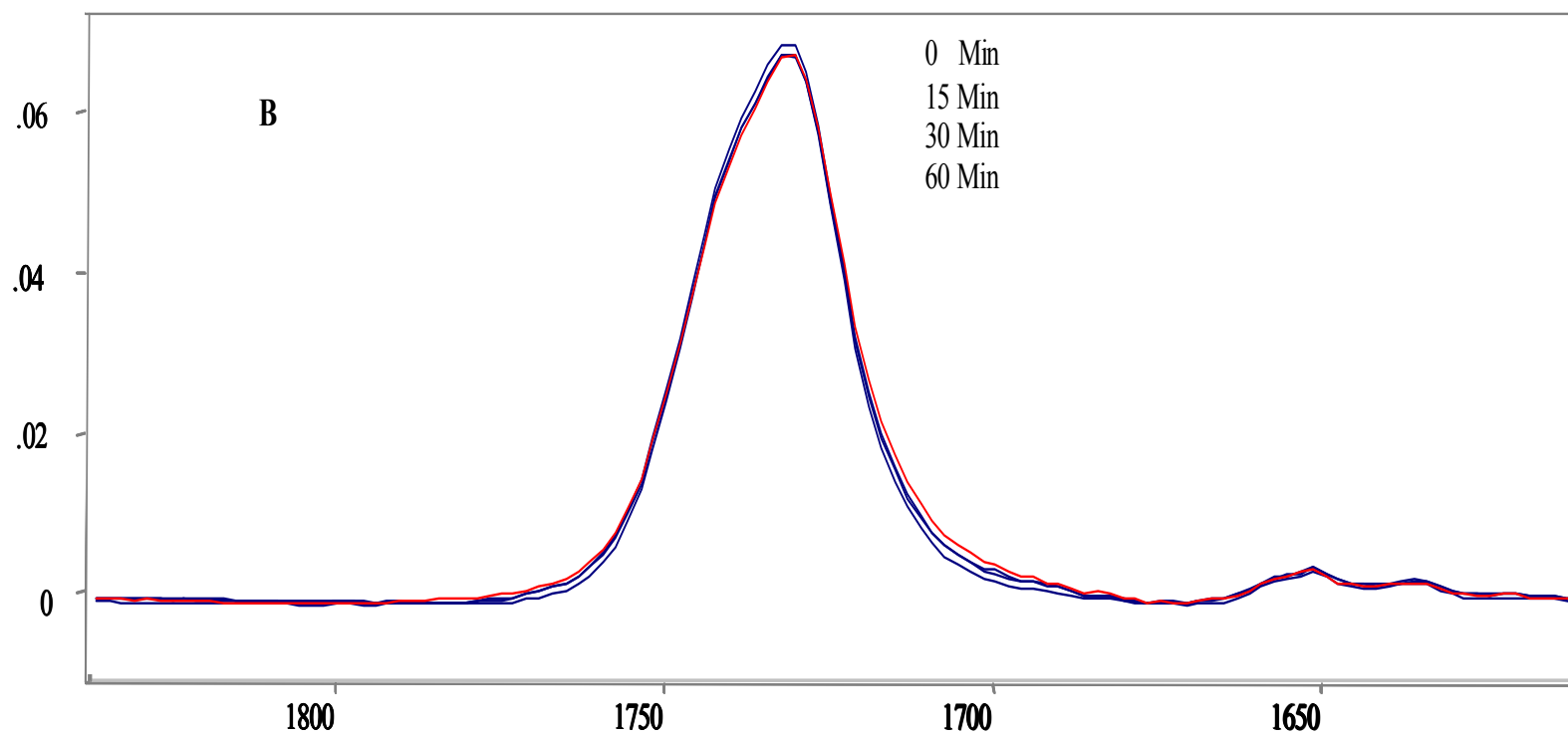
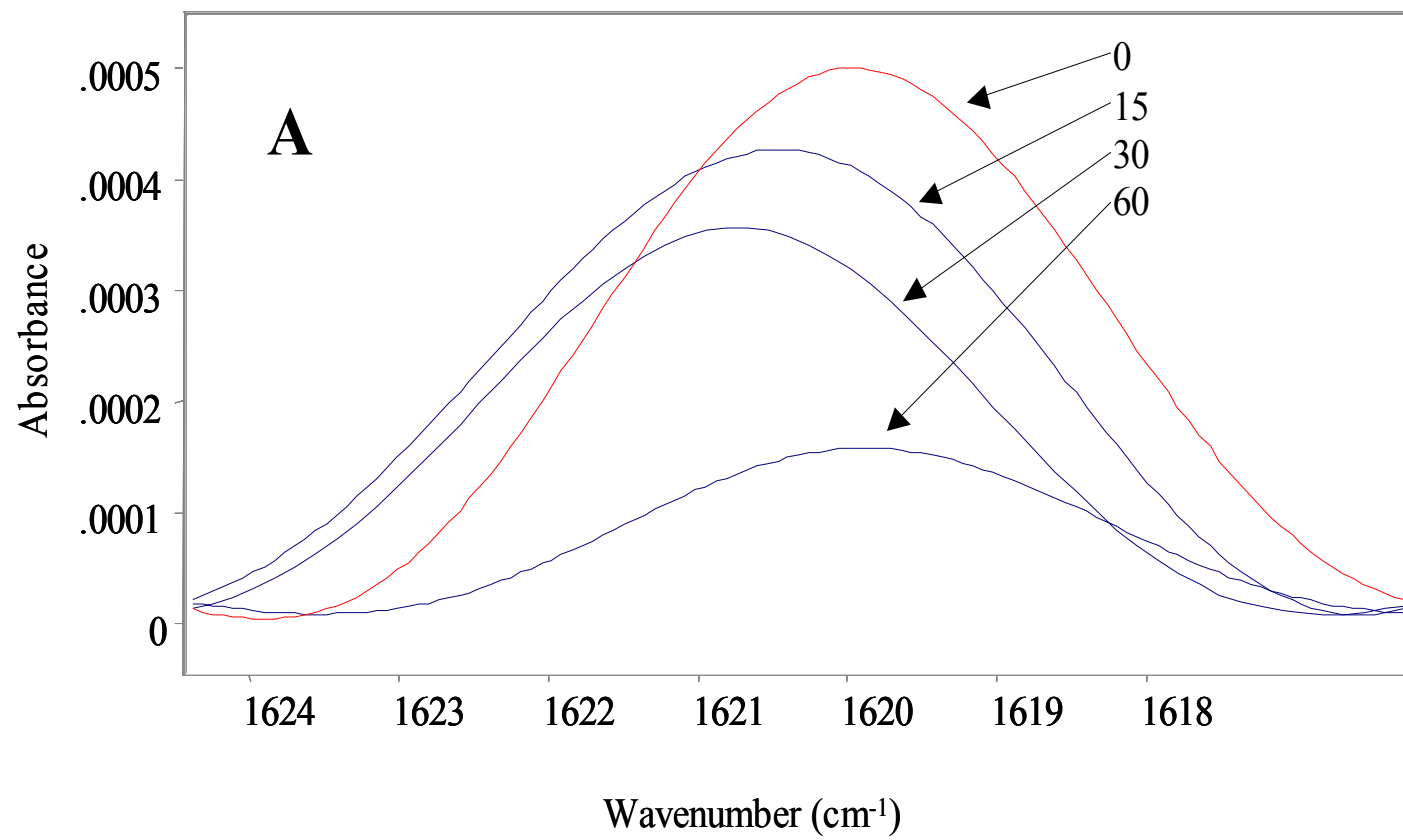


Figure A-3. (A) Sample 1 decrease in C=C band during irradiation for interpolated data. (B)
Ester Carbonyl Band during irradiation for interpolated data



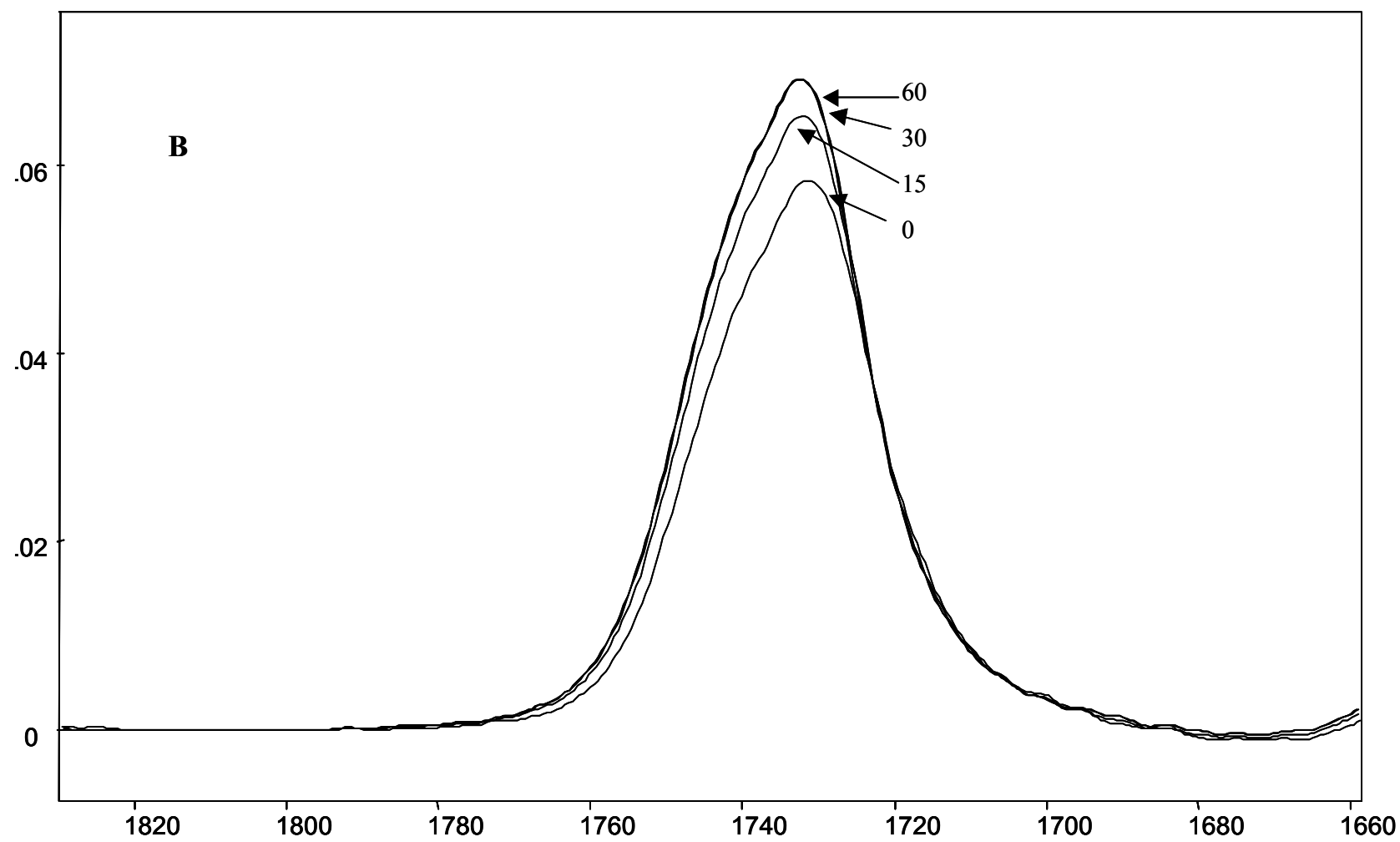
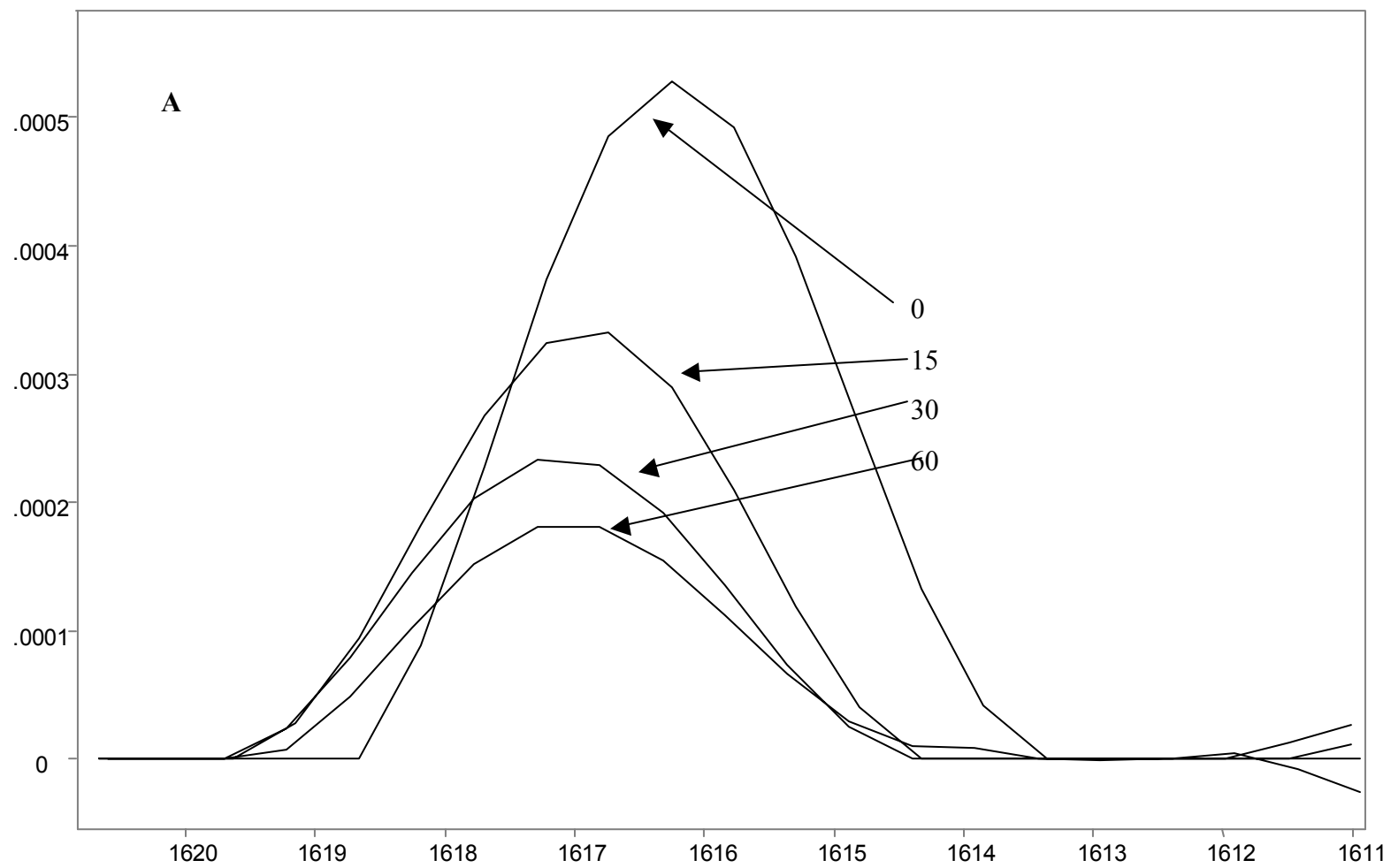


Figure A-4. (A) Sample 2 decrease in C=C band during irradiation for interpolated data. (B)
Ester Carbonyl Band during irradiation for interpolated data



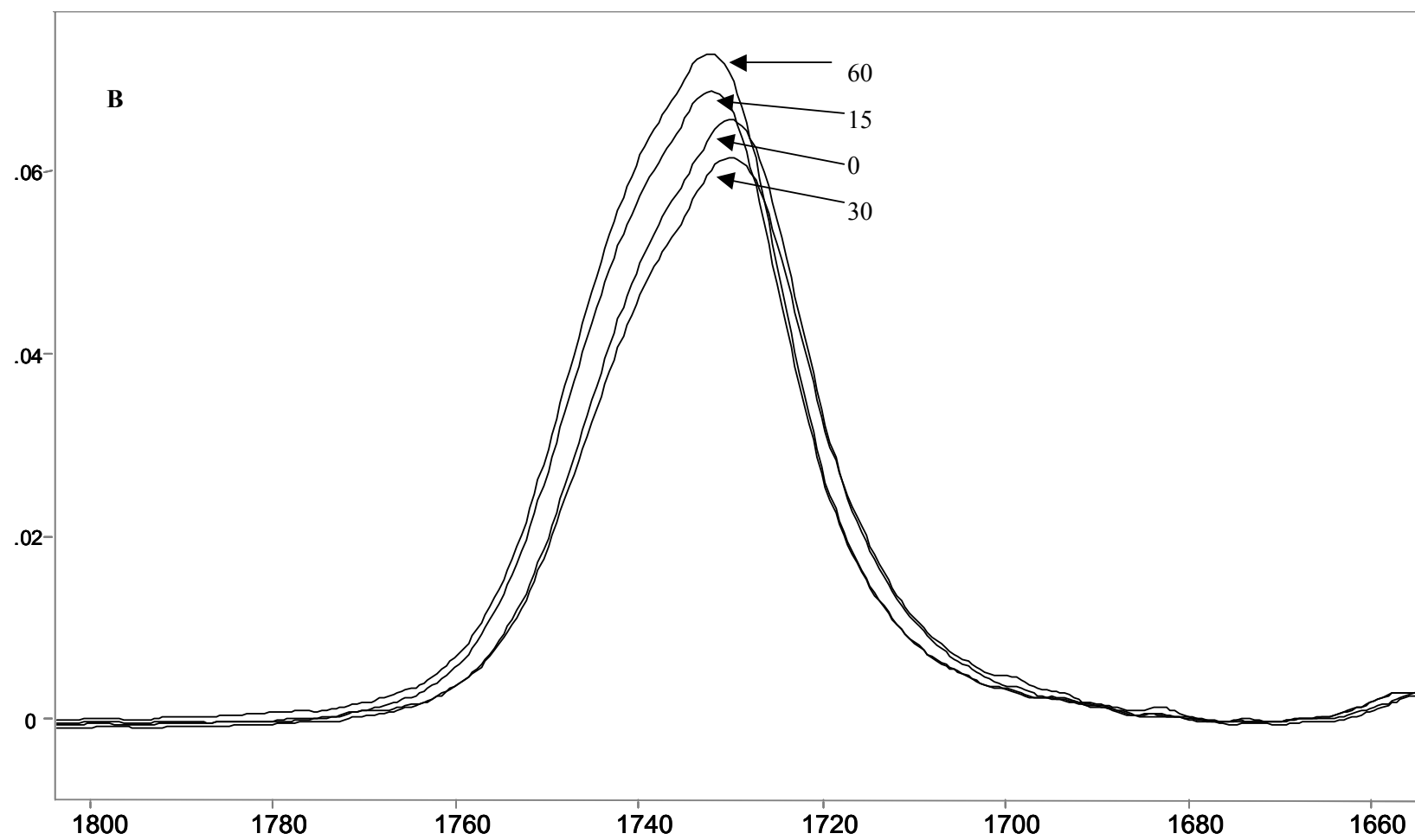


Table A-1. Numerical Values for Raw IR Data.

| Sample | Irradiation Time (Minutes) | C=C Area | C=O Area | A_0-A_t/A_0 | Percent |
|----------|----------------------------------|----------|----------|---------------|----------------|
| | | | | Ratio | Polymerization |
| Sample 1 | 0 | 0.00067 | 0.86619 | 0.000776 | 0 |
| | 15 | 0.00027 | 1.00247 | 0.000271 | 65 |
| | 30 | 0.00017 | 0.97417 | 0.000174 | 78 |
| | 60 | 0.00014 | 1.53112 | 0.000093 | 88 |
| Sample 2 | 0 | 0.00074 | 1.00019 | 0.000743 | 0 |
| | 15 | 0.00026 | 0.91229 | 0.000289 | 61 |
| | 30 | 0.00018 | 1.04590 | 0.000169 | 77 |
| | 60 | 0.00014 | 1.10881 | 0.000128 | 83 |

Table A-2. Numerical values for Interpolated IR data.

| Sample | Irradiation Time (Minutes) | C=C Area | C=O Area | Ratio | Percent |
|--------------|----------------------------------|----------|----------|---------|----------------|
| | | | | | Polymerization |
| Sample 1 FFT | 0 | 0.00387 | 3.67806 | 0.00105 | 0 |
| | 15 | 0.00118 | 4.03783 | 0.00029 | 72 |
| | 30 | 0.00106 | 4.21577 | 0.00025 | 76 |
| | 60 | 0.00086 | 4.20575 | 0.00021 | 81 |
| Sample 2 FFT | 0 | 0.00302 | 3.99988 | 0.00075 | 0 |
| | 15 | 0.00189 | 3.64723 | 0.00052 | 31 |
| | 30 | 0.00135 | 4.19619 | 0.00032 | 57 |
| | 60 | 0.00100 | 4.42627 | 0.00023 | 70 |

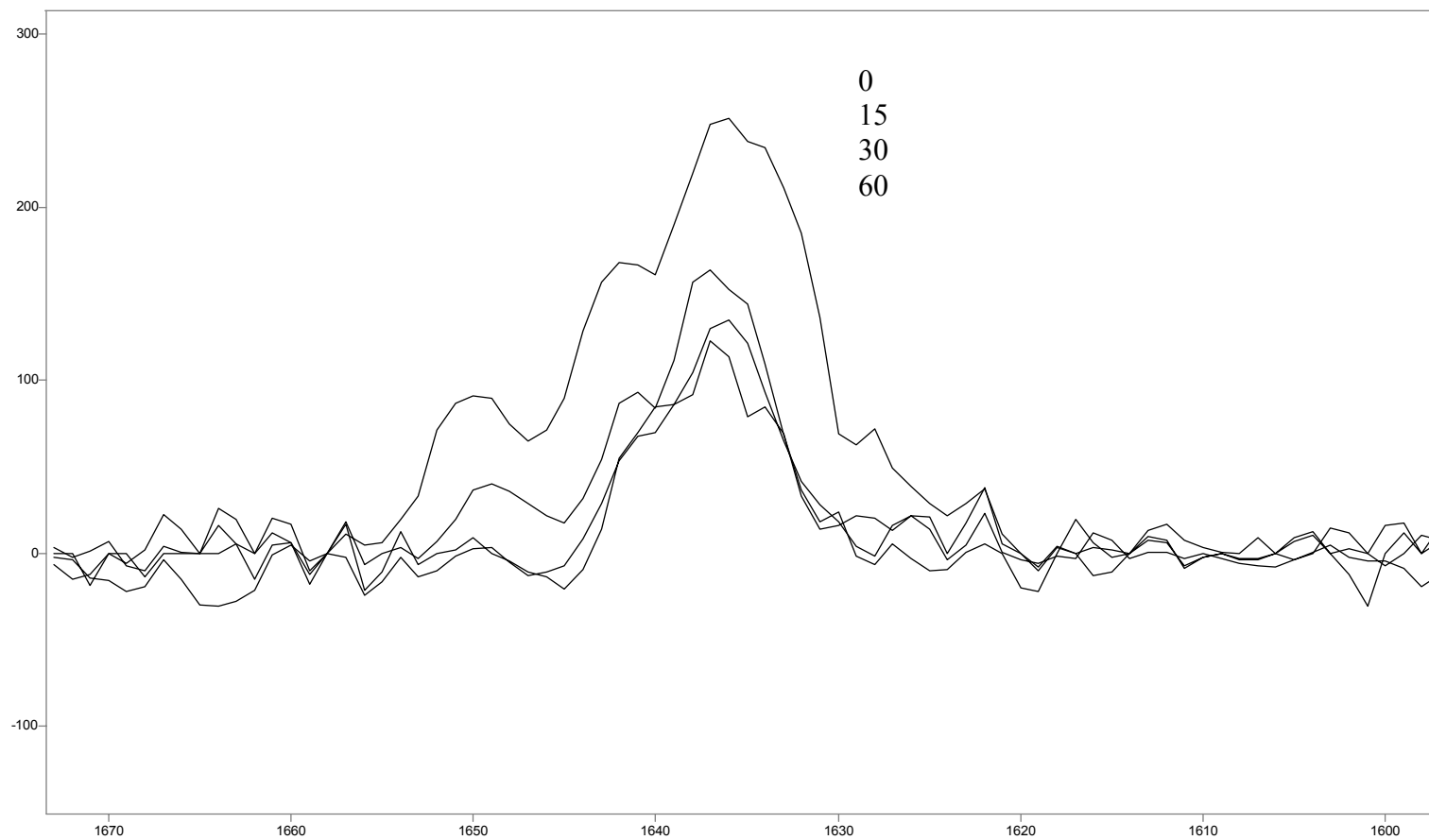
large difference in the integrated peak areas, and thus, a large difference in the percent polymerization when compared to the raw data. Due to this large difference, we chose to use the raw data for comparison purposes. Without a known value for the percent polymerization and using a small sample set, the most consistent data was chosen. Although the relative absorbance changes slightly in the interpolated data, the band more than doubles its width. In comparing the two methods, there is close agreement between the two data sets collected from the raw data. However, there is a large disparity between the interpolated data results. Based on these values, it was decided to use the raw data for subsequent comparison to the Raman microscopy results.

Quantitation of Photopolymerization in minimally hydrated lipid sample with white light irradiation by Raman microscopy. Two significant issues must be addressed prior to beginning the discussion of the Raman analysis. The first of these issues is the noise present in the spectra. In some of the sample data, there is only a 3:1 SNR. This provides for a level of uncertainty in choosing the correct baseline to use for area calculations on the peak and also introduces concern about true peak shape and error. In order to minimize the effects of the noise on the analysis, a baseline was chosen that passed through the center of the noise. The second issue deals with the fundamental differences between the two techniques that are being compared. In infrared analysis, there is a set path length and extinction coefficient, so the absorbance value that we see for the C=C stretch is based only on the change of concentration for the double bond. This concentration, and thus the absorbance value, changes, as the double bond is broken during polymerization. In Raman analysis, the intensity of a given peak is based on the Raman scatter and the collection of that scatter. There are a large number of variables that can affect this, as discussed in Chapter II of this dissertation, and it is not uncommon to see a variation in peak intensity for the same sample in back to back runs. It is for this reason that Raman spectroscopy

cannot be used for quantitative analysis based solely on peak intensities. However, Raman may be used for quantitation through the use of an internal standard. The internal standard allows for comparison between different measurements because it provides a scale to judge any change in intensity by. For the analysis discussed here, the C-N stretch provides an internal standard to measure run to run intensity changes against as well as providing an unchanging band by which the ratio of A_0-A_t/A_0 may be calculated. Simply stated, it is not possible to visually inspect a single band and determine the percent polymerization of a given sample based solely on the intensity of that band when the measurement is taken using Raman spectroscopy. To facilitate visual identification of relative percent polymerization, normalization to the C-N stretch may be performed. This will provide a visual reference similar to the decrease in absorbance seen in infrared measurements. Normalized C=C spectra are displayed for each data set, allowing the reader to visually gauge percent polymerization rather than relying on tabulated numerical data.

The results presented in this section were obtained by analysis of the raw data after baseline correction and by analysis of the raw data after baseline correction and smoothing. Interpolating the data in this case contributed to the noise making analysis more difficult and introducing more uncertainty into the measurement. Smoothing was accomplished using the smoothing program contained within the Grams32/AI software. A two point binomial smoothing was selected as a balance between noise reduction and change in peak shape. The raw Raman data is shown in Figures A-5A,B and A-6A,B and the smoothed data is shown in Figures A-7A,B and Figures A-8A,B. The normalized Raman data is displayed in figure A-9A-D. The results of the analysis are shown in tabulated format in Table A-3 and A-4. A second method of analysis was performed on the raw data where a peak centered at 1636 cm^{-1} was fitted to the data

Figure A-5. (A). Sample 1 change in C=C stretch during irradiation (B) Sample 1 change in C-N stretch during irradiation

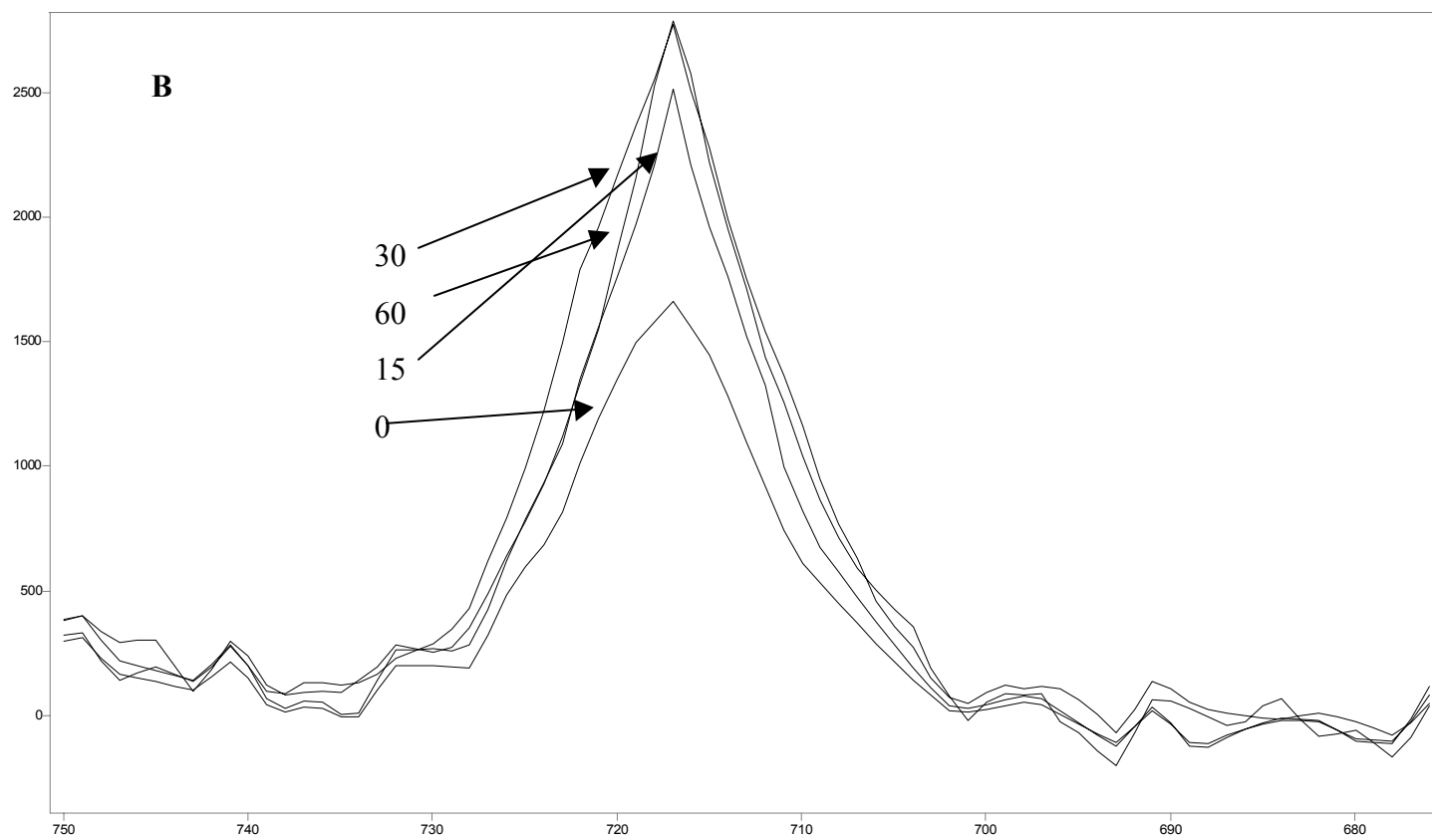


Counts / Raman Shift (cm-1)

Overlay X-Zoom CURSOR

File # 1 : 1218D2O60

Res=None



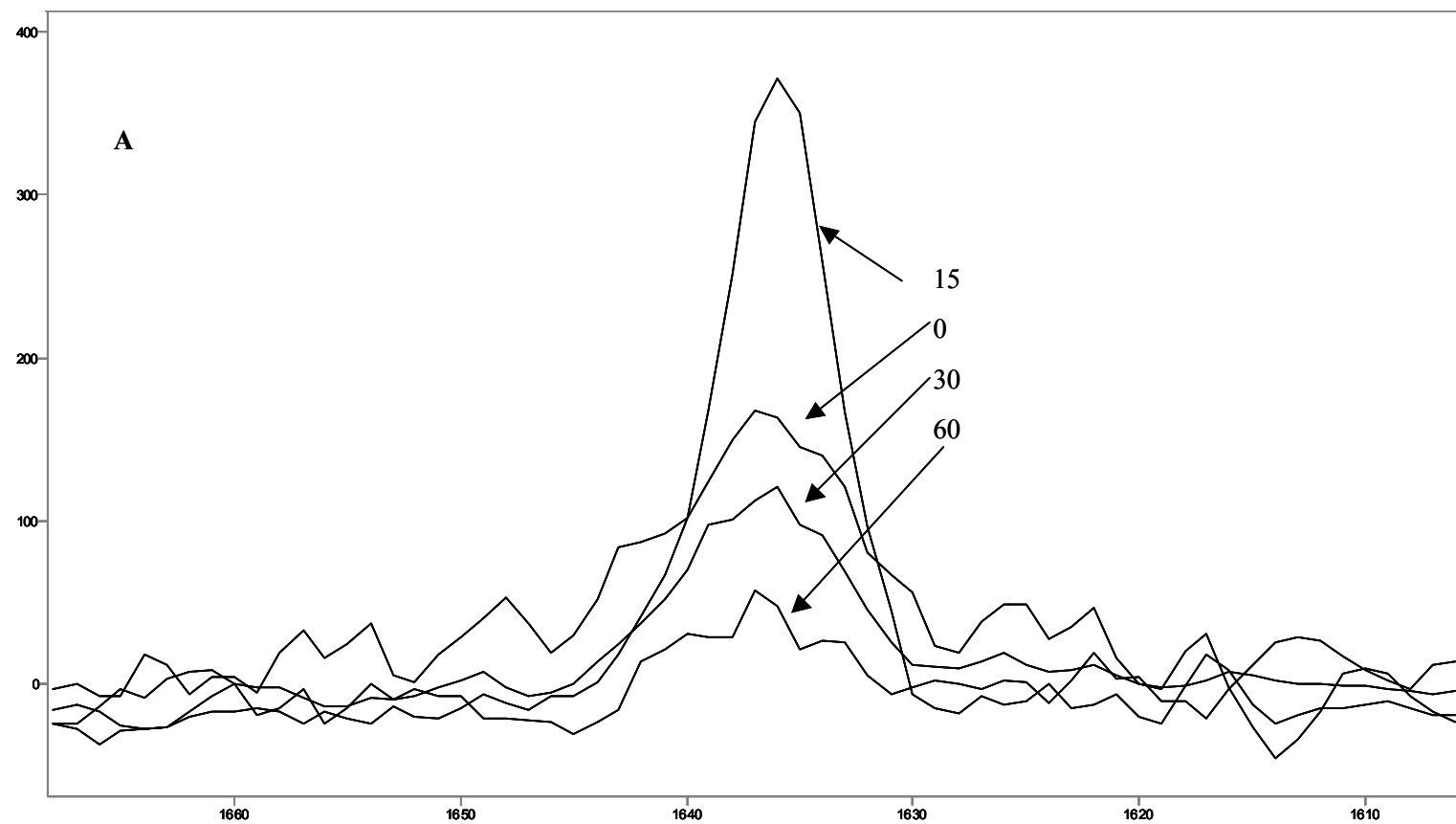
Counts / Raman Shift (cm-1)

Overlay X-Zoom CURSOR

File # 1 : 1218D2O60

Res=None

Figure A-6. (A). Sample 2 change in C=C stretch during irradiation (B) Sample 2 change in C-N stretch during irradiation

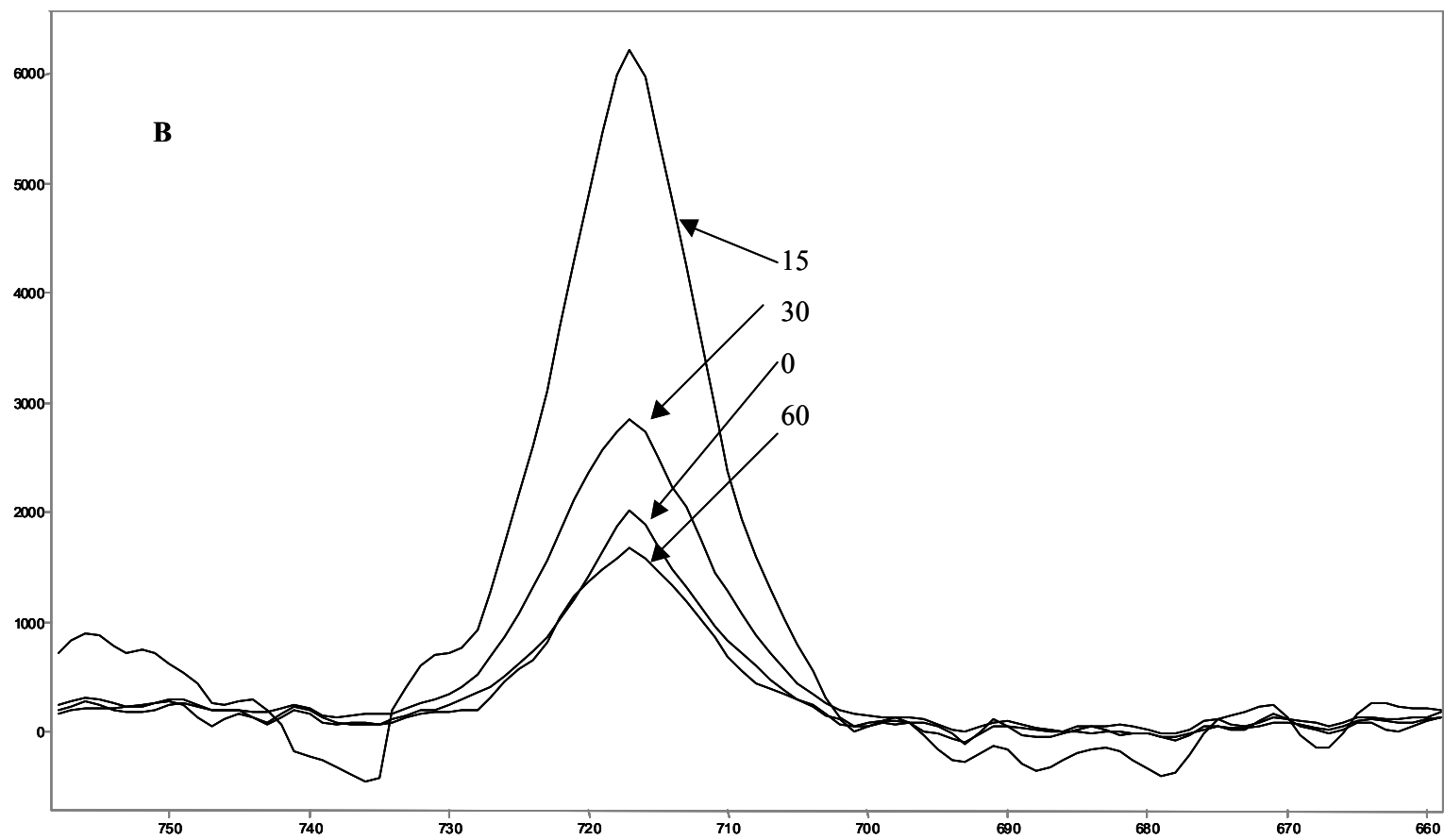


Counts / Raman Shift (cm-1)

File # 2 : 0308D2O15

Overlay X-Zoom CURSOR

Res=None



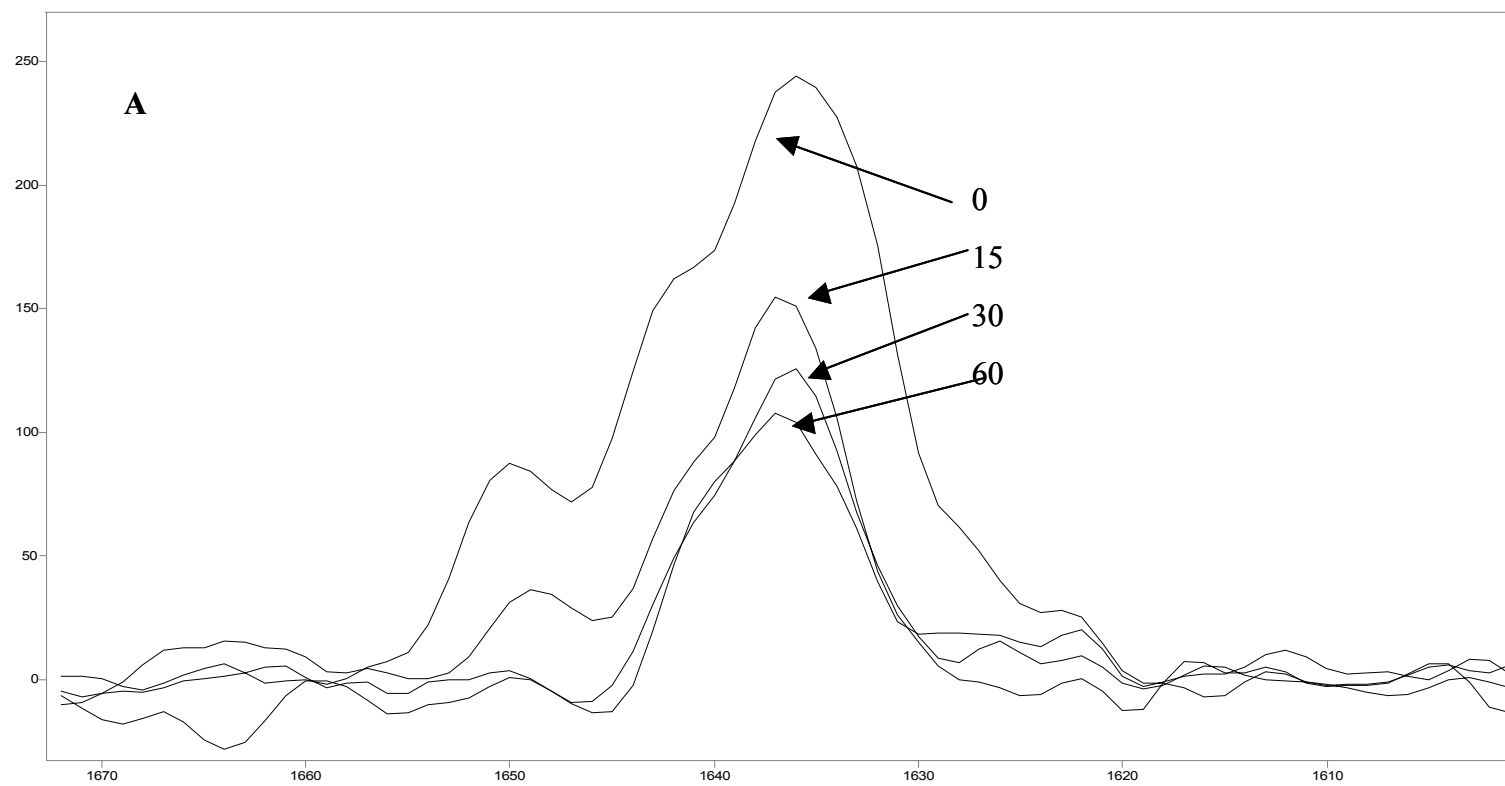
Arbitrary / Arbitrary

File # 4 : 0308D2060

Overlay X-Zoom CURSOR

Res=Nonr

Figure A-7. (A). Sample 1 smoothed C=C stretch during irradiation. (B). Sample 1 smoothed C-N stretch during irradiation.

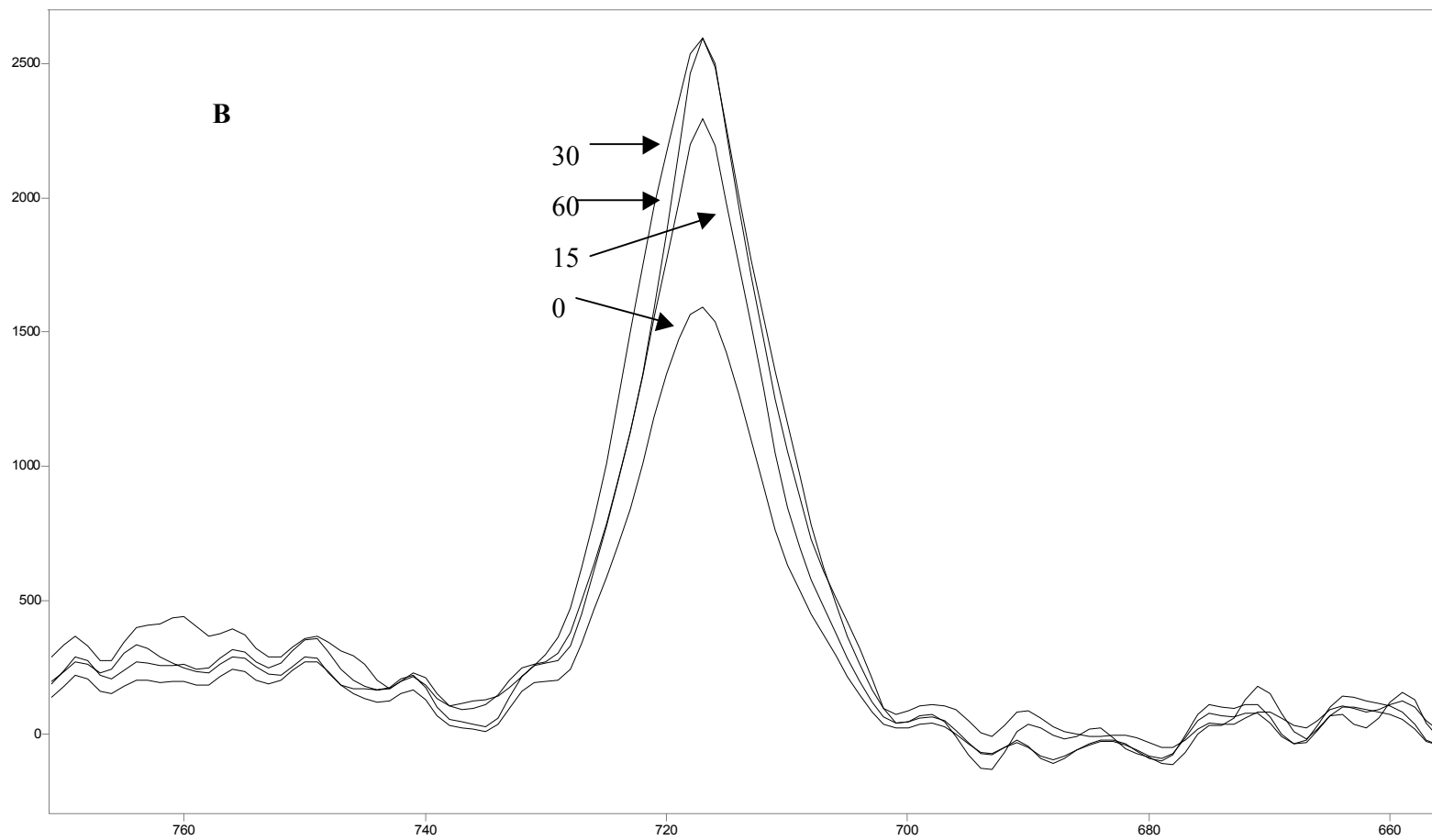


Counts / aman Shift (cm-1)

Overlay X-Zoom CURSOR

File # 1 1218D2O0SMOOTH

Res=None



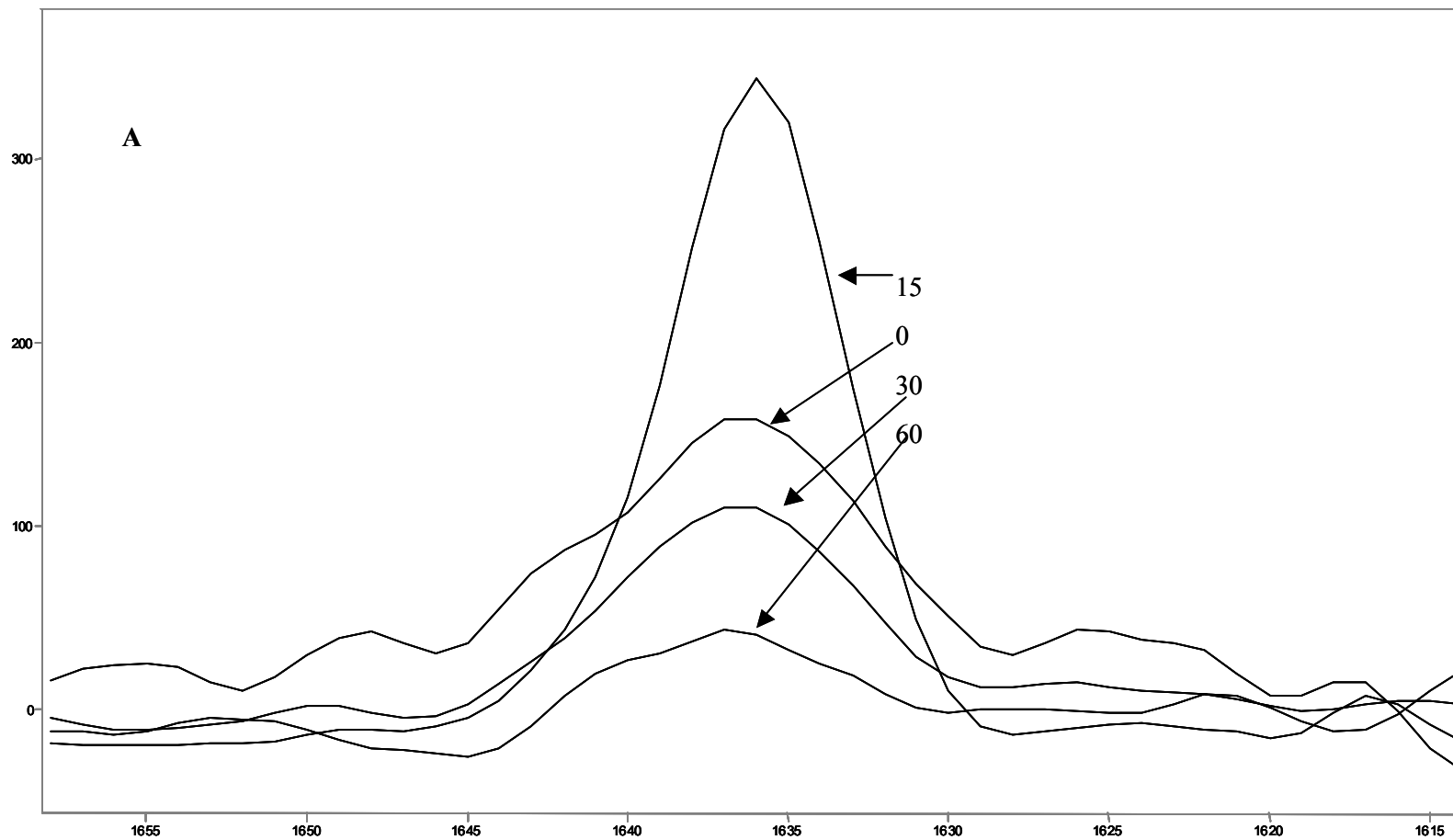
Counts / Raman Shift (cm-1)

Overlay X-Zoom CURSOR

File # 1 : 1218D2O0SMOOTH

Res=None

Figure A-8. (A). Sample 2 smoothed C=C Stretch during irradiation (B) Sample 2 smoothed C-N stretch during irradiation

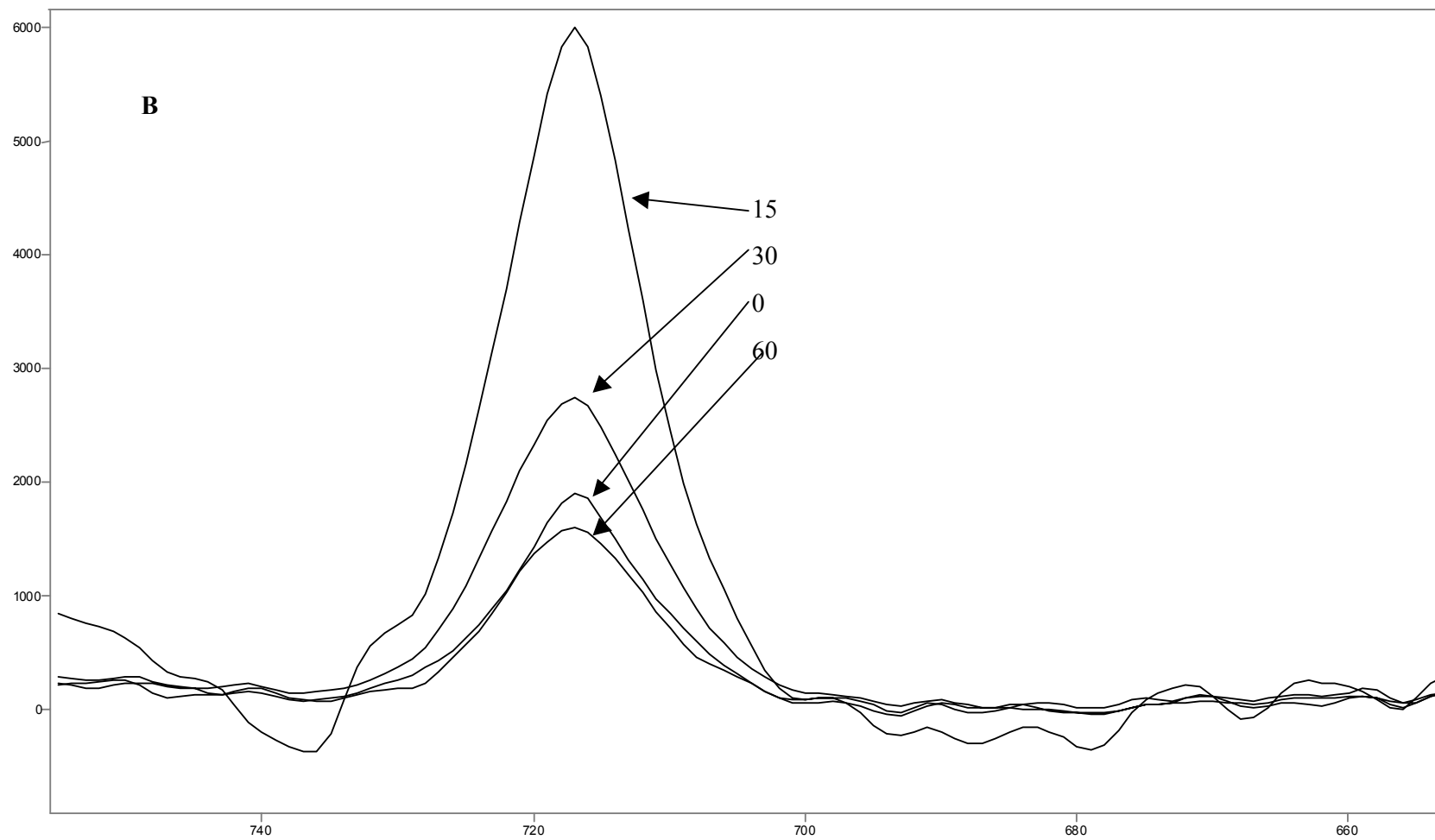


Counts / Raman Shift (cm-1)

Overlay X-Zoom CURSOR

File # 3 : 0308D2O15SMOOTH

Res=None



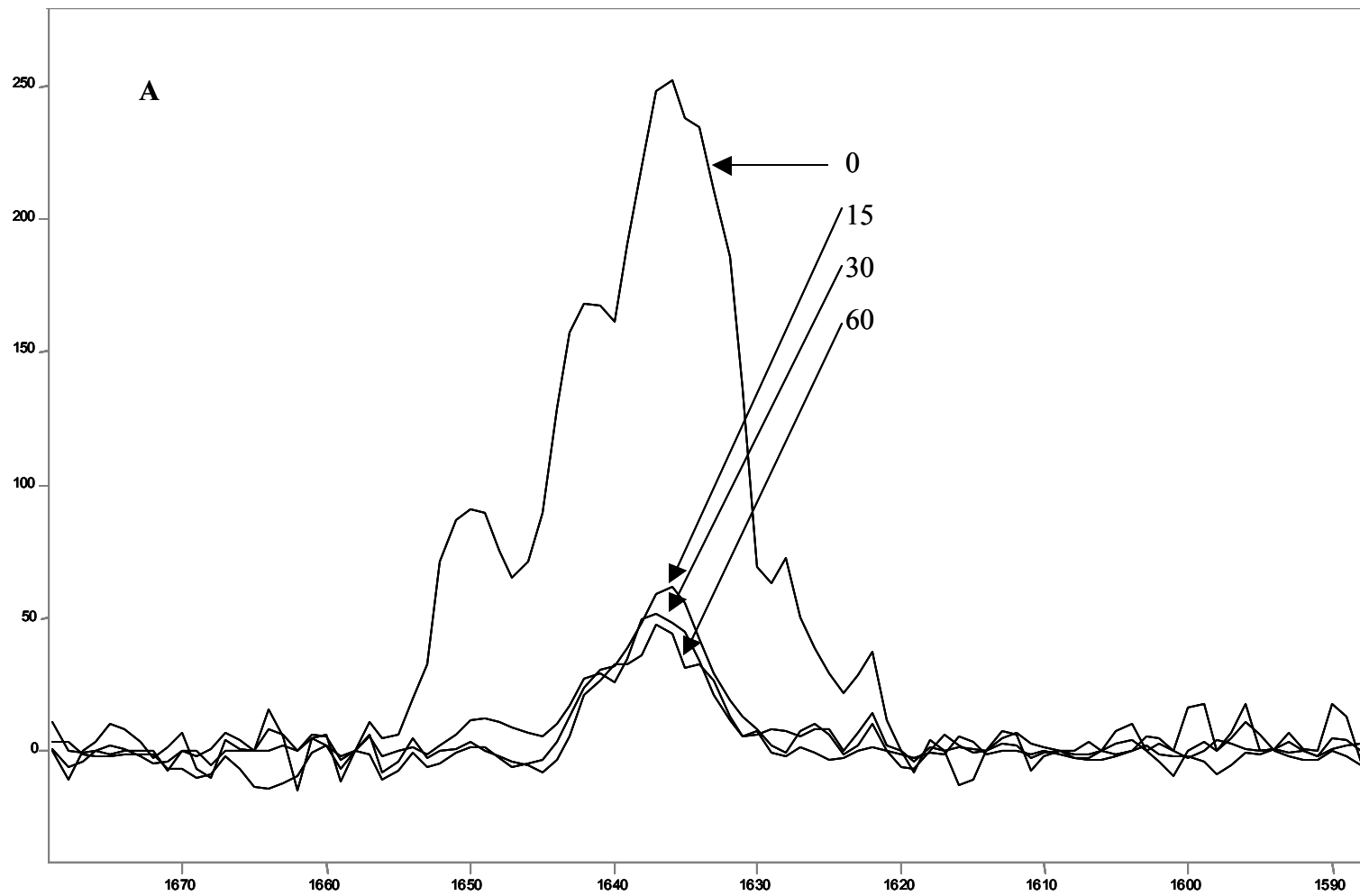
Counts / Raman Shift (cm-1)

Overlay X-Zoom CURSOR

File # 3 : 0308D2O15SMOOTH

Res=None

Figure A-9. (A) Sample 1 normalized C=C stretch (B) Sample 2 normalized C=C stretch (C) Sample 1 smoothed and normalized C=C stretch (D) Sample 2 smoothed and normalized C=C stretch.

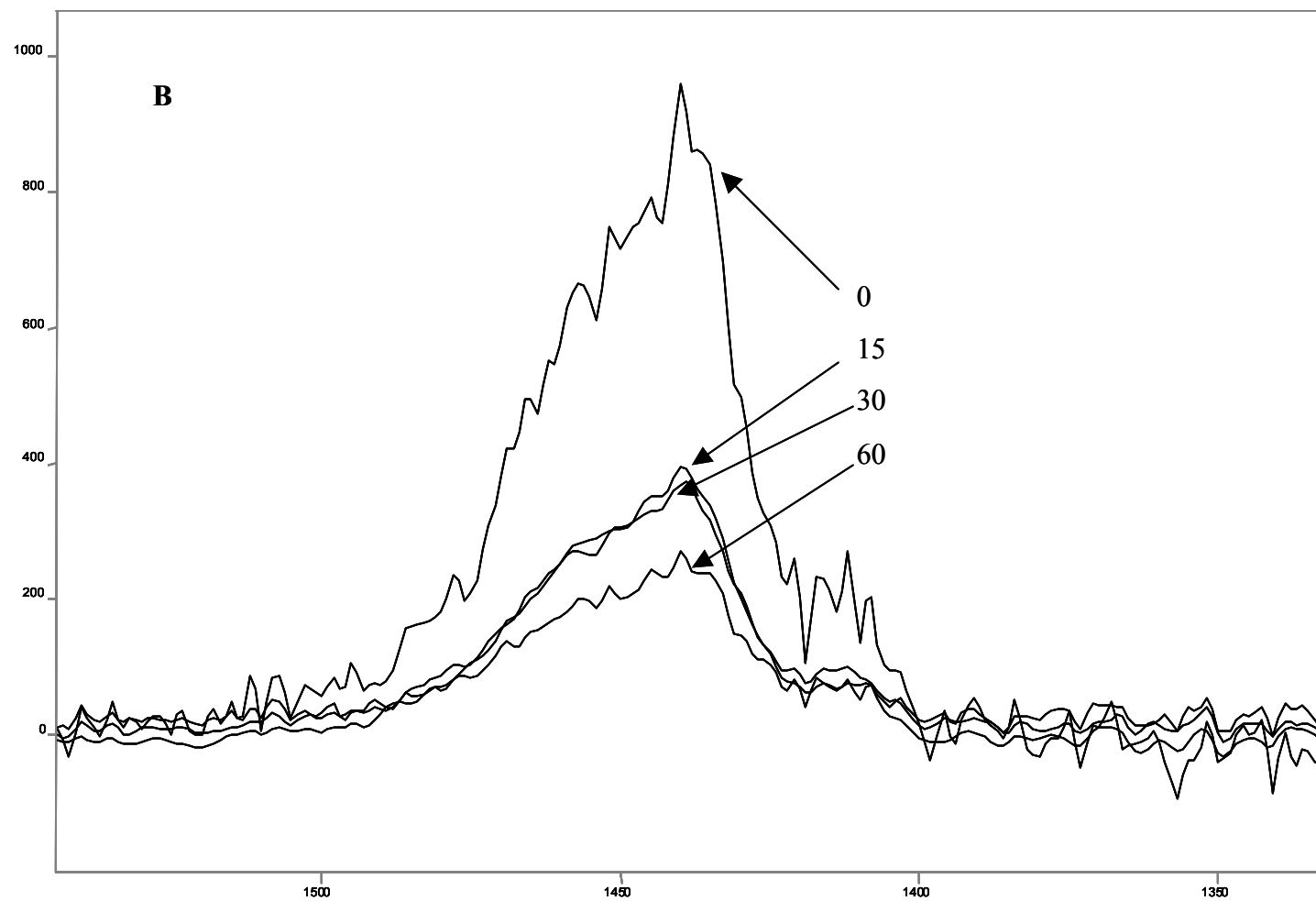


Counts / Raman Shift (cm-1)

Overlay Y-Zoom CURSOR

File # 1 : 1218D200

Res=None

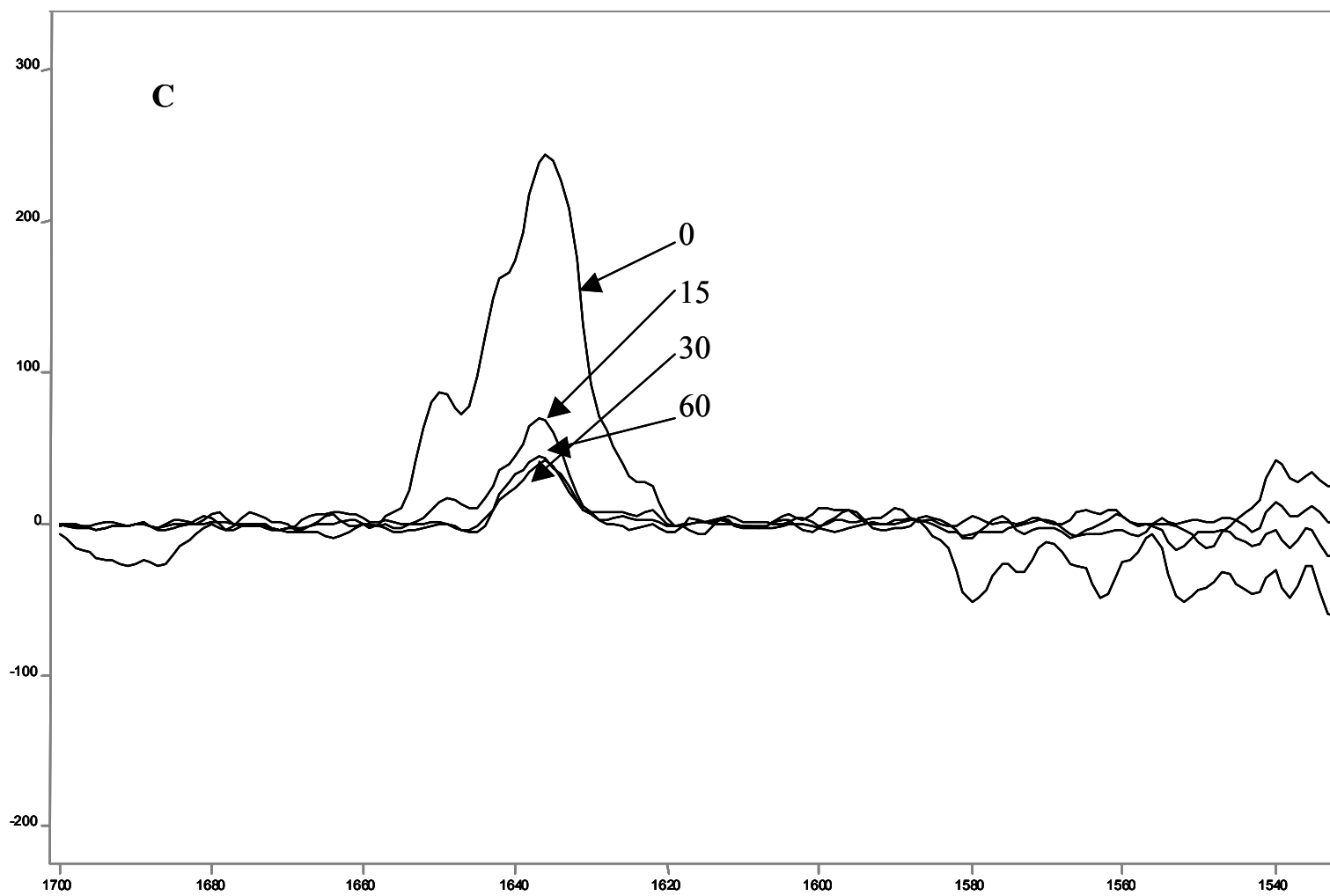


Counts / Raman Shift (cm-1)

Overlay Y-Zoom CURSOR

File #4 : 0308D200

Res=None

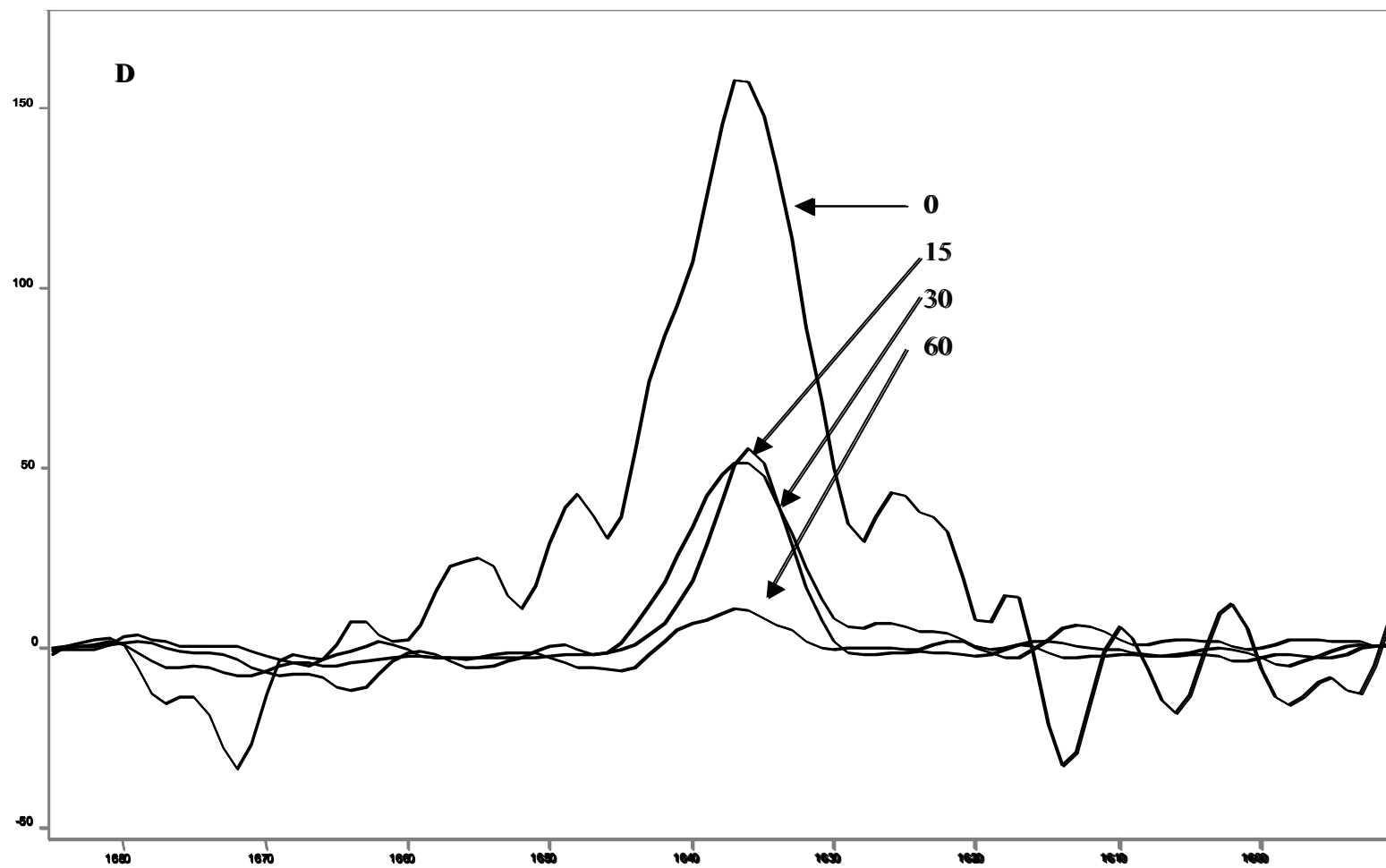


Counts / Raman Shift (cm-1)

Overlay Y-Zoom CURSOR

File # 3 : 1218D2030SMOOTHNORM

Res=None



Counts / Raman Shift (cm-1)

Overlay Y-Zoom CURSOR

File # 4 : 0308D200SMOOTH

Res=None

Table A-3. Numerical values for raw Raman data

| Sample 1 | Irradiation Time | C=C Area | C-N Area | Ratio | Percent |
|----------|------------------|----------|----------|----------|----------------|
| | (Minutes) | | | | Polymerization |
| | 0 | 3873.797 | 22933.93 | 0.168911 | 0 |
| | 15 | 1241.834 | 30809.75 | 0.040307 | 76 |
| | 30 | 1172.656 | 34037.56 | 0.034452 | 80 |
| | 60 | 874.9811 | 32666.47 | 0.026785 | 84 |
| Sample 2 | | | | | |
| | 0 | 1236.317 | 19853.47 | 0.062272 | 0 |
| | 15 | 2547.864 | 97157.8 | 0.026224 | 58 |
| | 30 | 904.8186 | 37628.3 | 0.024046 | 61 |
| | 60 | 427.3655 | 24800.1 | 0.017232 | 72 |

Table A-4. Numerical values for smoothed Raman data.

| Sample 1 smoothed | Irradiation Time | C=C Area | C-N Area | Ratio | Percent |
|-------------------|------------------|----------|----------|----------|----------------|
| | (Minutes) | | | | Polymerization |
| | 0 | 4007.966 | 21882.63 | 0.183157 | 0 |
| | 15 | 1627.142 | 30299.78 | 0.053701 | 71 |
| | 30 | 1055.052 | 33871.54 | 0.031149 | 83 |
| | 60 | 1087.837 | 32491.29 | 0.033481 | 82 |
| Sample 2 smoothed | | | | | |
| | 0 | 1168.883 | 21430.43 | 0.054543 | 0 |
| | 15 | 2463.291 | 94738.47 | 0.026001 | 52 |
| | 30 | 952.8313 | 37371.54 | 0.025496 | 53 |
| | 60 | 251.8686 | 24059.46 | 0.010469 | 81 |

and the area beneath the peak was taken. The peak-fitting program in Grams32/AI was used to perform the fitting. This method allows for a more certain baseline selection in the noisier spectra, the results from this method are shown in Table A-5.

In examining the data, we see that there are substantial differences in the values obtained from sample one as compared to sample 2. These differences are easily attributed to the noise present in the sample. With the exception of the 15-minute irradiation period specimen from sample 2, the intensity values are fairly low and the SNR is 3:1. This leads to uncertainty in the choice of baseline when calculating the integrated area of the C=C stretch. As expected, we see large differences in the smoothed data as well. Rather surprisingly, the agreement between the smoothed data and the raw data for sample 1 is rather good. However, in the second sample where the SNR is poor, the smoothing makes a large difference in the area of the peak.

The closest agreement between measurements occurs in the peak fitted data. This data also matches most closely with the data from sample 1 which has a better SNR than that of Sample 2. The peak, or curve, fitting application in Grams is typically used to resolve overlapped bands. Although often misused, this can be a powerful analysis tool if the true number of bands and peak positions in a sample is known. For the minimally hydrated lipid samples, the peak position is known and no other band overlap the C=C stretch. By eliminating the possibility of a false report, we may use this tool to reduce the effects of noise in our measurement. Due to the agreement between the two samples in the curve fit data and their agreement with the raw data from sample 1, the peak fitting data was chosen for comparison with the IR data.

Comparison of Raman and infrared minimally hydrated lipid data. To make an accurate comparison of the data for each type of measurement, it is necessary to examine the standard deviation. As previously discussed, the handling of the data is crucial in making an accurate

Table A-5. Numerical values for peak fitting Raman data.

| Sample 1 peak fitted | Irradiation | C=C Area | C-N Area | Ratio | Percent Polymerization |
|----------------------|-------------------|----------|----------|----------|---------------------------|
| | Time (Minutes) | | | | |
| | 0 | 4080.515 | 22933.93 | 0.177925 | 0 |
| | 15 | 1646.725 | 30809.75 | 0.053448 | 70 |
| | 30 | 1117.839 | 34037.56 | 0.032841 | 82 |
| | 60 | 936.6932 | 32666.47 | 0.028674 | 84 |
| Sample 2 peak fitted | | | | | |
| | 0 | 2042.64 | 19853.47 | 0.102886 | 0 |
| | 15 | 2438.506 | 97157.8 | 0.025098 | 76 |
| | 30 | 1110.586 | 37628.3 | 0.029515 | 71 |
| | 60 | 308.7579 | 24800.1 | 0.012450 | 88 |

determination of the percent polymerization for each method. If this is not handled properly, the comparison of the two sets of data has no meaning. A list of standard deviations is shown for each of the types of analysis previously discussed is shown in Table A-6. From this data, we can see that our choice of peak fitted Raman data and raw IR data are the appropriate choices for each technique. The smaller standard deviation will allow for a more accurate comparison of the results from the two methods. A plot of percent polymerization versus time for both the Raman and infrared measurements is shown in Figure A-10. From the plot, we can see that the fifteen minute irradiation period does not correspond for the two measurement types, even including the error bars. The other measurements at thirty and sixty minutes both fall within the limits of error for and indicate that the agreement between the Raman and infrared measurements is adequate for comparing the two techniques. Although these results seem to indicate that Raman is a viable measurement method for percent polymerization when using an internal standard, it should also be noted that the limited number of measurements performed on this system to date cannot be expected to provide absolute value calibration for the given irradiation periods. As with any new system being measured, repeated sampling is the best insurance of an accurate determination.

Quantitation of Photopolymerization in minimally hydrated lipid sample with 514.5nm irradiation by Raman microscopy. Data analysis for the 514.5 nm irradiated lipid sample was conducted in the same manner as previously described for the white light irradiated samples. The findings were very similar in regards to the agreement between the raw data and the data obtained by peak fitting. A notable exception to this agreement is for the sample irradiated for 30 seconds. The peak fitted data provided for a percent polymerization of 12 percent while the raw data yielded a value of 25 percent polymerization. Table A-7 provides the numerical values for the integrated areas of each measurement while three representative spectra are shown in

Table A-6. Standard deviation in Raman and IR data measurements.

| Measurement Type | Irradiation Time (Min) | Standard deviation σ |
|-----------------------|------------------------|-----------------------------|
| Infrared Raw | 0 | 0 |
| | 15 | 2.8 |
| | 30 | .7 |
| | 60 | 3.5 |
| Infrared Interpolated | 0 | 0 |
| | 15 | 29.0 |
| | 30 | 13.4 |
| | 60 | 7.8 |
| Raman Raw | 0 | 0 |
| | 15 | 12.7 |
| | 30 | 13.4 |
| | 60 | 8.5 |
| Raman Smoothed | 0 | 0 |
| | 15 | 13.4 |
| | 30 | 21.2 |
| | 60 | .7 |
| Raman Peak Fitted | 0 | 0 |
| | 15 | 4.2 |
| | 30 | 7.78 |
| | 60 | 2.83 |

Figure A-10. Plot of percent polymerization Raman vs. IR.

Percent Polymerization in minimally hydrated Lipid

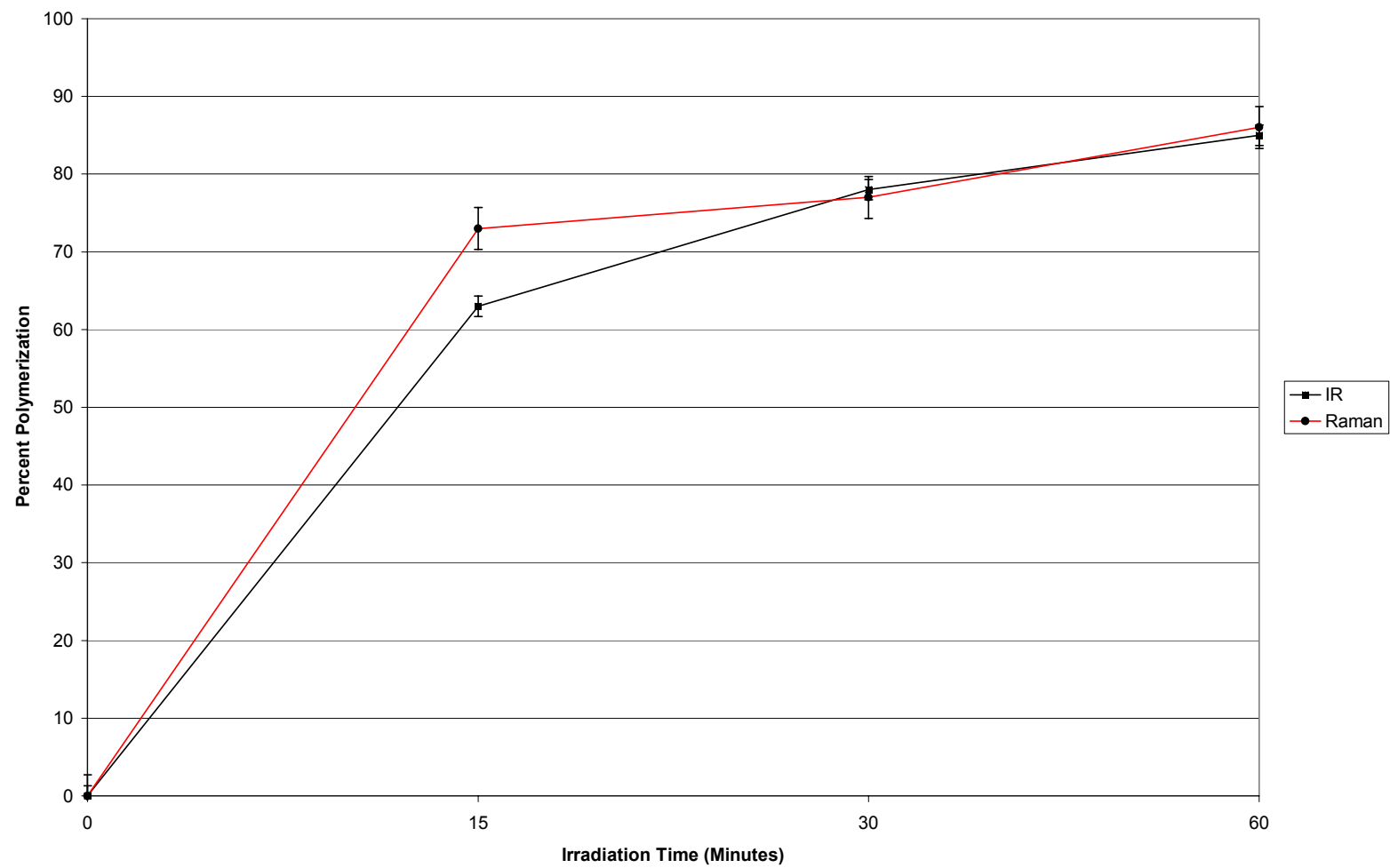


Table A-7. Raman COG and Peak Fit values for green irradiation

Raman Analysis of Minimally Hydrated Lipid Using
COG

| Time (Minutes) | Area of C=C | Area of C-N | Ratio of C=C to C-N | Percent Polymerization |
|---------------------------|--------------------|--------------------|--------------------------------|-----------------------------------|
| 0 | 128173.7 | 1188790.0 | 0.1078 | 0 |
| 30 | 1746.4 | 21712.2 | 0.0804 | 25 |
| 90 | 1297.3 | 22255.3 | 0.0583 | 46 |
| 150 | 1008.1 | 23406.4 | 0.0431 | 60 |
| 210 | 13180.2 | 1117428.0 | 0.0118 | 89 |
| 240 | 0.0 | 896766.0 | 0.0000 | 100 |

Raman Analysis of Minimally Hydrated Lipid Using Peak Fitting

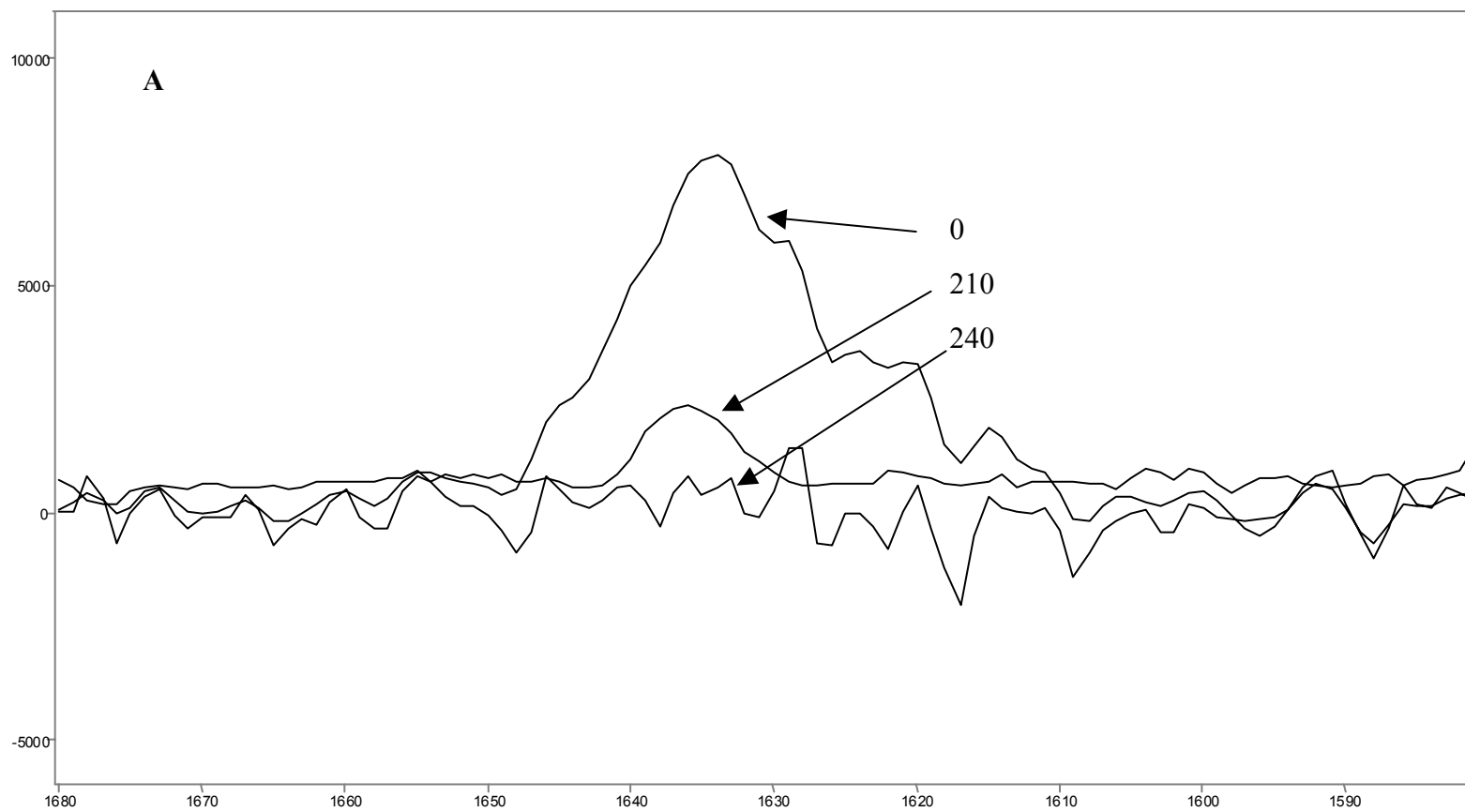
| | | | | |
|-----|----------|-----------|--------|-----|
| 0 | 127181.5 | 1188790.0 | 0.1070 | 0 |
| 30 | 2050.0 | 21712.2 | 0.0944 | 12 |
| 90 | 1286.4 | 22255.3 | 0.0578 | 46 |
| 150 | 1018.4 | 23406.4 | 0.0435 | 59 |
| 210 | 12055.1 | 1117428.0 | 0.0108 | 90 |
| 240 | 0.0 | 885418.5 | 0.0000 | 100 |

Figure A-11. Representative data are shown here due to the large difference in relative intensities for this data. This variability comes from variations in exciting laser power from sample run to sample run. The Ar⁺ pump laser was tuned for 514.5 nm light to irradiate these samples and then tuned for multi-line visible to pump the Ti:Sapphire ring laser used for incident irradiation with the Raman microscope. Despite efforts to maintain constant power density from run to run, this was not possible. Normalized data of all irradiation times are shown in Figure A-12. This data represents a single sample and as such, cannot be measured for standard deviation. However, because this methodology is based on the previous comparison to IR, it cannot be more accurate than this measurement. Based on the results obtained from the 514.5nm irradiation, we see nearly an order of magnitude decrease in irradiation times for polymerization.

Quantitation of Photopolymerization in PTFE graft sample with 514.5nm irradiation by Raman microscopy. Analysis of these films was conducted in the manner described previously with the following modification. Due to several overlapping bands in the 1580 cm⁻¹ to 1730 cm⁻¹ region it was necessary to perform a spectral subtraction order to isolate the C=C stretching vibration for analysis. This was accomplished by using a PTFE graft sample that included all of the layers of the membrane mimetic film with the exception of the monoacrylate-PC and photoinitiator as a background sample and subtracting this from samples of the membrane mimetic film irradiated for the given time periods. The tabulated results of the measurement are shown in Table A-8. The data following subtraction are shown in Figure A-13 with the normalized data being shown in Figure A-14.

Discussion of error and ways to minimize its effects. For this set of experiments, the single greatest source of error is the small sampling size. As the number of repeat measurements becomes greater, the standard deviation from the mean generally becomes smaller. It is with this

Figure A-11. (A) C=C stretch during irradiation by 514.5 nm light (B) C-N stretch during irradiation by 514.5 nm light.

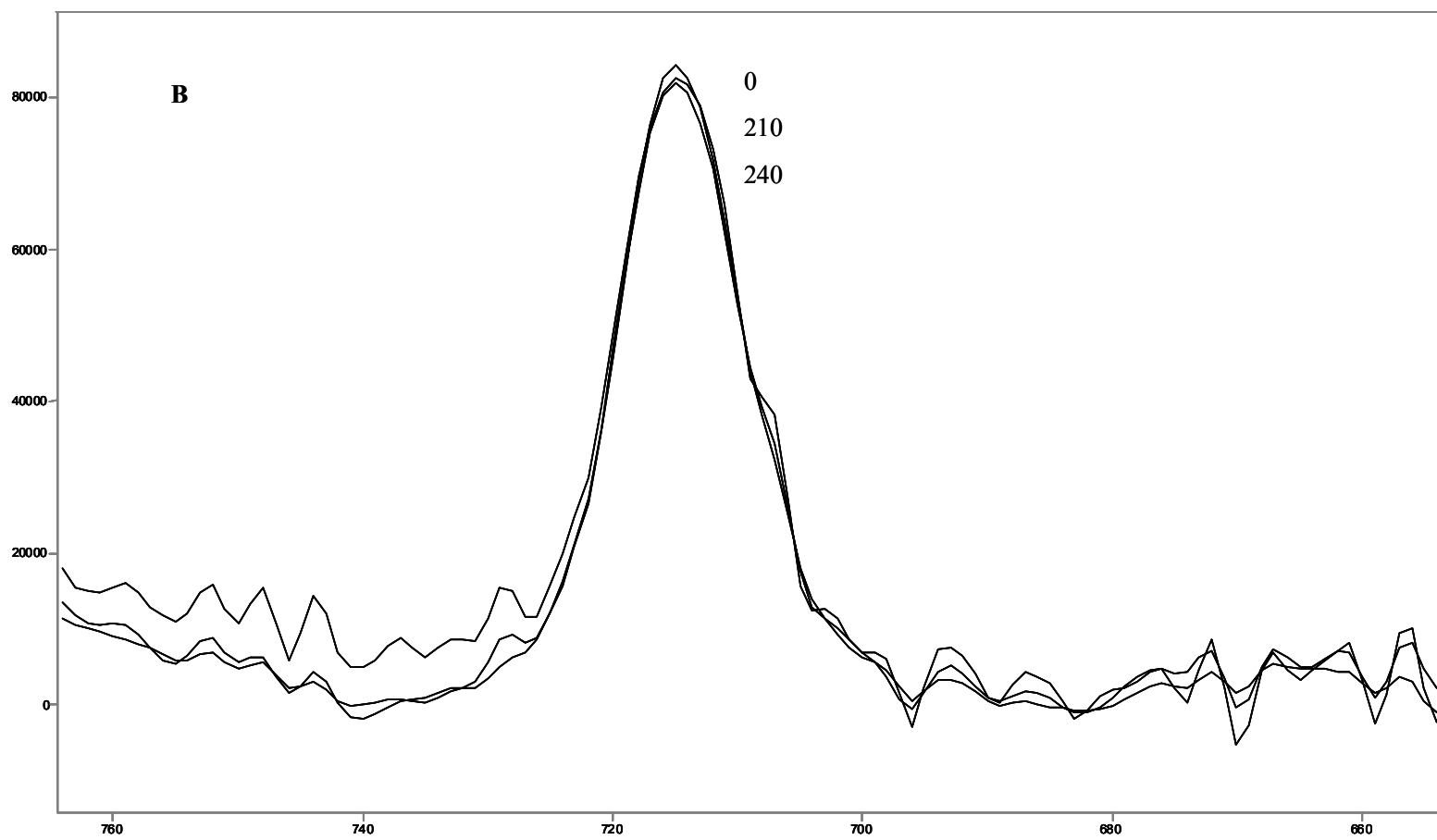


Counts / Raman Shift (cm-1)

Overlay X-Zoom CURSOR

File # 2 : 0419GREEN210

Res=None



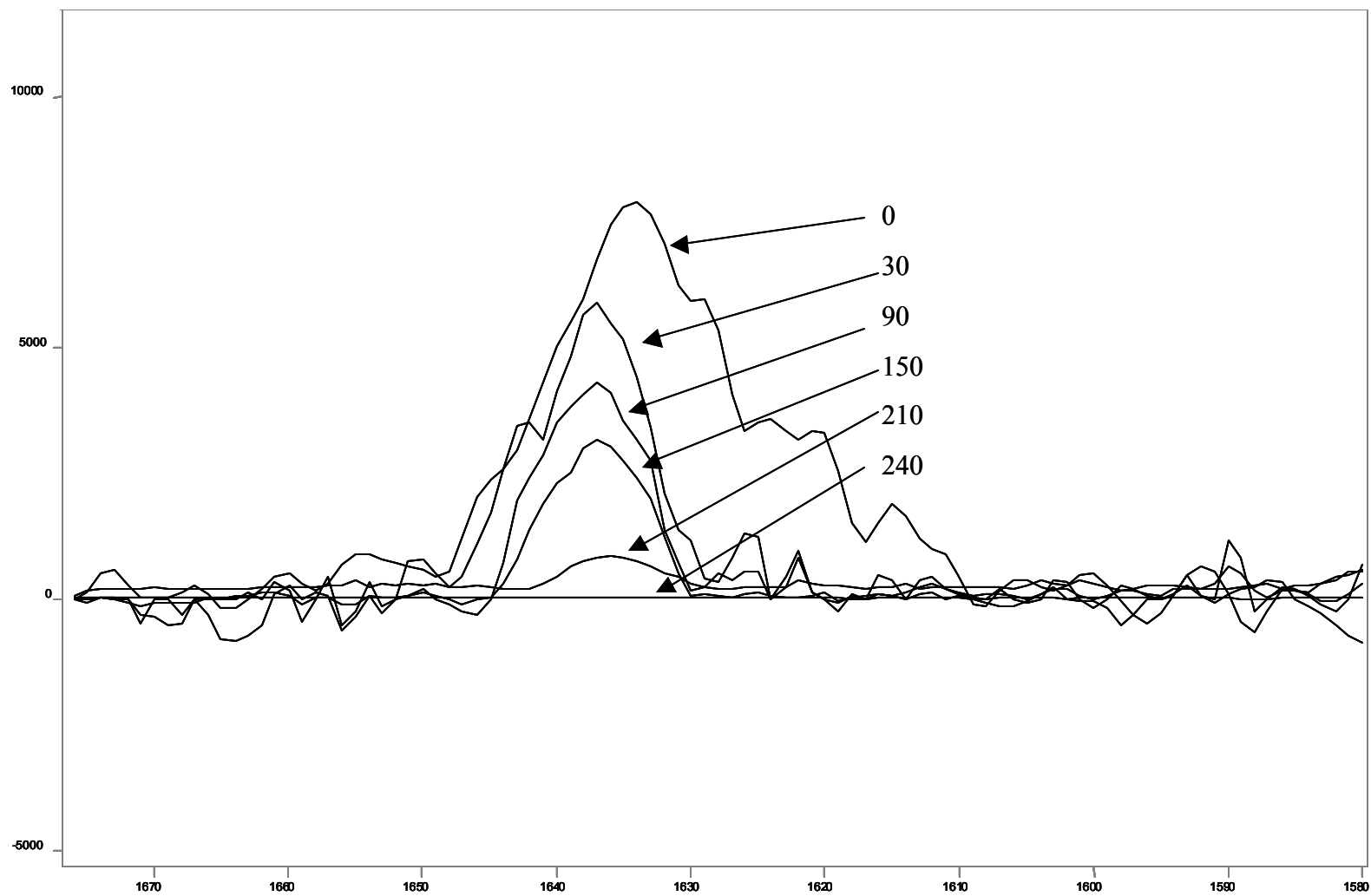
Counts / Raman Shift (cm-1)

Overlay X-Zoom CURSOR

File # 3 : 0419GREEN240

4/19/2002 5:27 PM Res=None

Figure A-12. Normalized C=C data for 514.5 nm irradiation



Counts / Raman Shift (cm-1)

Overlay Y-Zoom CURSOR

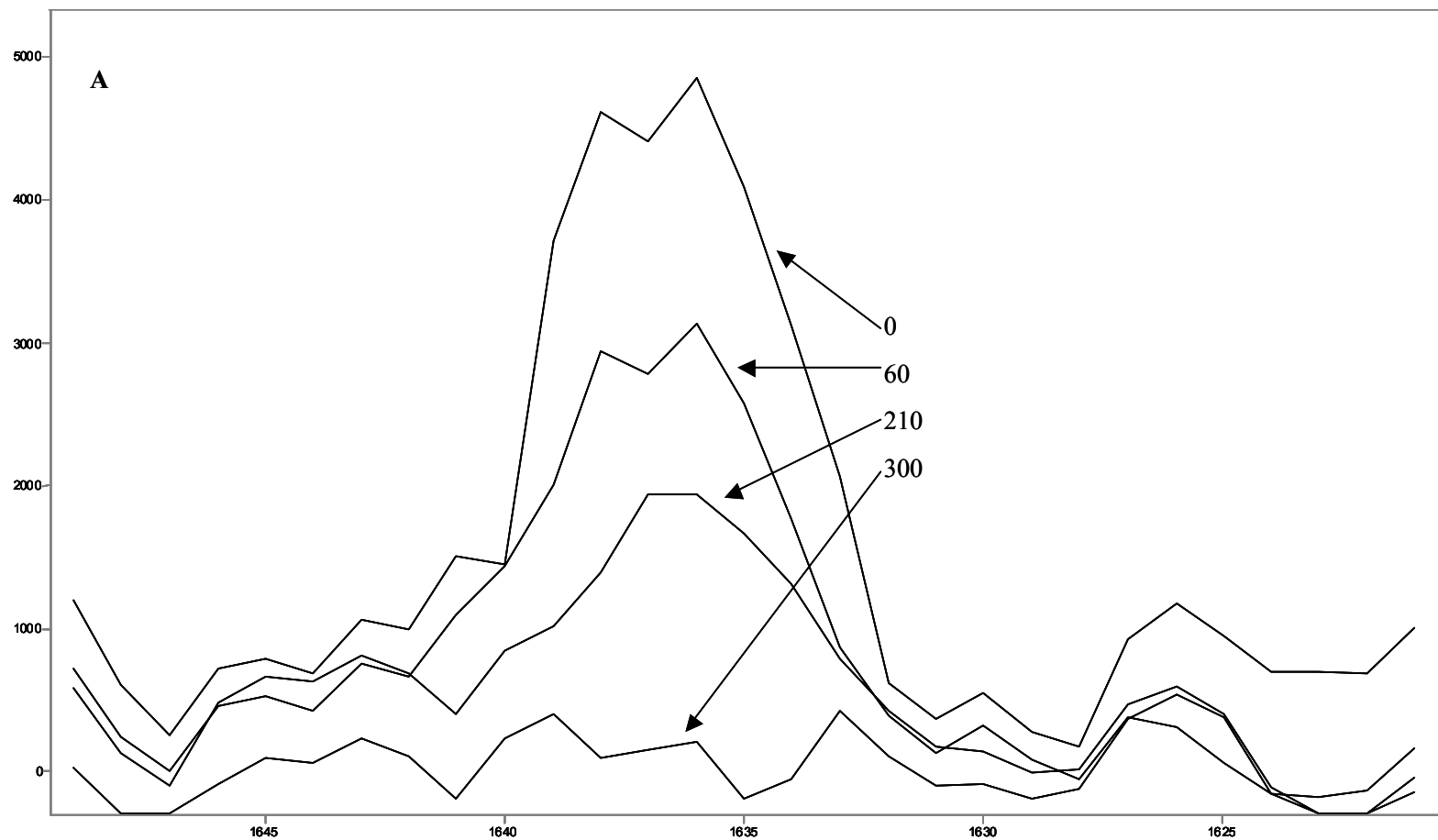
File # 1 : 0419GREEN 0

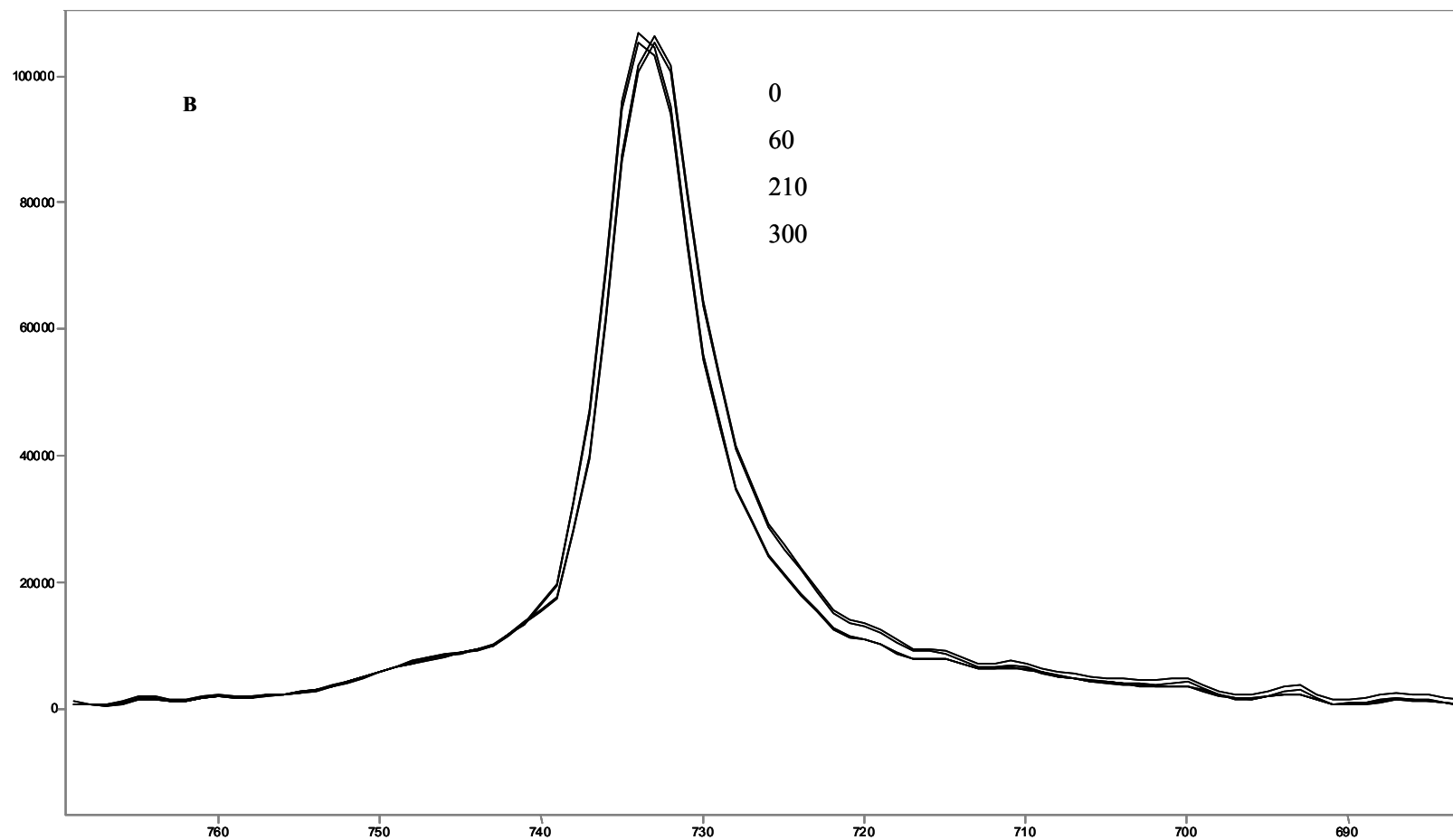
4/19/2002 2:50 PM Res=None

Table A-8. Tabulated data for PTFE graft irradiation.

| COG | Irradiation Time | | | | Percent |
|----------|------------------|----------|----------|----------|----------------|
| | (Seconds) | C=C Area | C-N Area | Ratio | Polymerization |
| | 0 | 22576.1 | 1068719 | 0.021124 | 0 |
| | 60 | 13887.59 | 1069949 | 0.012980 | 39 |
| | 210 | 5624.35 | 1093444 | 0.005144 | 76 |
| | 300 | 0 | 1101819 | 0.000000 | 100 |
| Peak Fit | Irradiation Time | | | | Percent |
| | (Seconds) | C=C Area | C-N Area | Ratio | Polymerization |
| | 0 | 22576.1 | 1078104 | 0.020941 | 0 |
| | 60 | 13887.59 | 1075627 | 0.012911 | 38 |
| | 210 | 5624.35 | 1112504 | 0.005056 | 76 |
| | 300 | 0 | 1105711 | 0.000000 | 100 |

Figure A-13. (A). PTFE Graft C=C after subtraction (B) PTFE Graft C-N stretch during irradiation





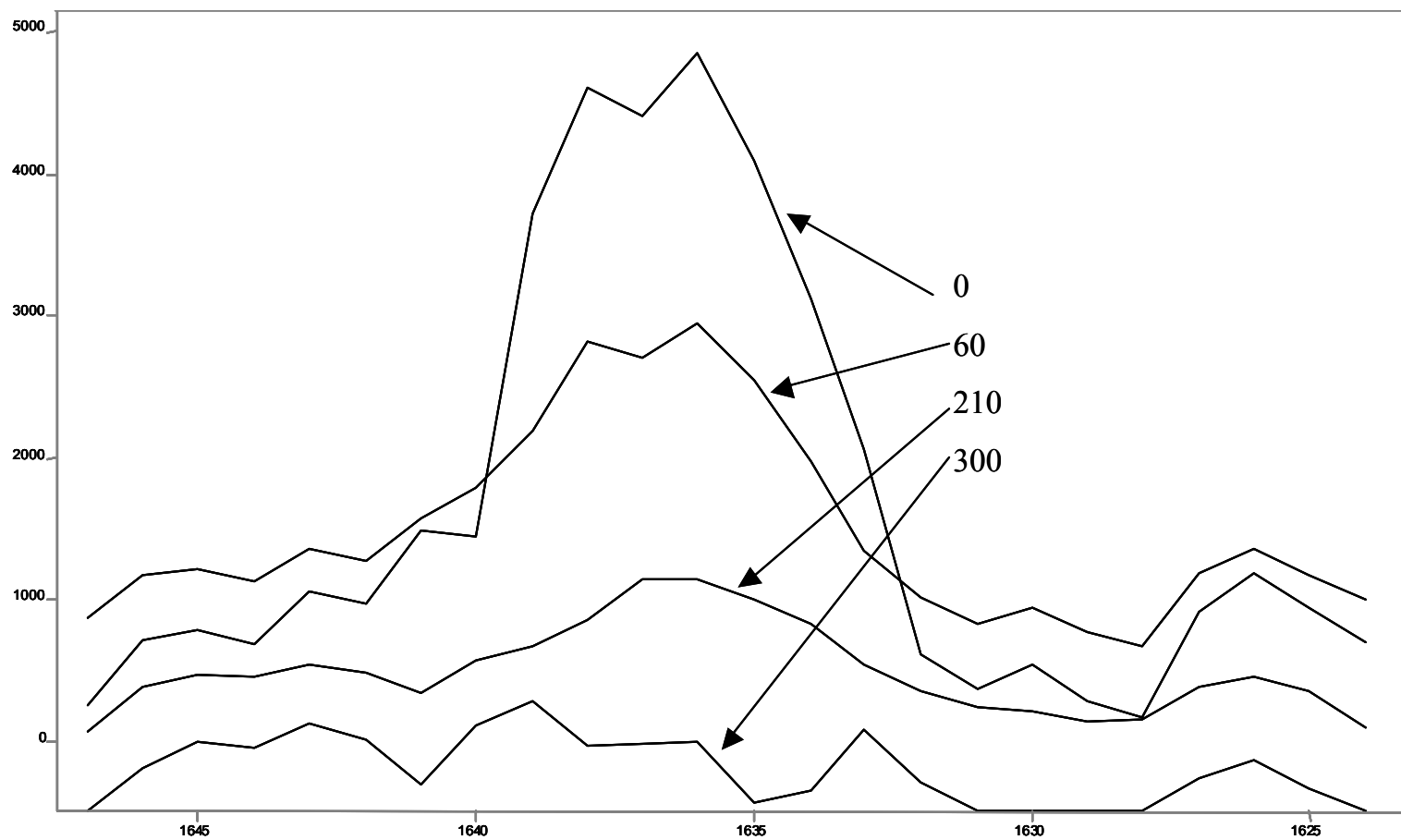
Counts / Raman Shift (cm-1)

Overlay X-Zoom CURSOR

File # 1 : 0604GRAFT0SUB

Res=None

Figure A-14. Normalized C=C data from Graft sample.



Counts / Raman Shift (cm-1)

File # 1 : 0604GRAFT0SUB

Overlay Y-Zoom CURSOR

Res=None

in mind that the author acknowledges the limitations of the measurements presented herein. As research continues on the development of the membrane mimetic film, samples will become more readily available. The increased sample availability will lead to a larger number of measurements and a more accurate determination of percent polymerization by the methods presented in this appendix and in Chapter III of this dissertation.

Another significant source of error in the Raman measurements of the white light irradiated films is the noise present in the spectra. The most readily apparent solution to minimizing this source of error is through a larger number of co-added acquisitions. With samples irradiated by 514.5 nm wavelength light, much longer integration times are also possible since sample drying is not an issue for the shorter irradiation and measurement times. Through a combination of improved signal to noise and the addition of a larger number of samples, the accuracy of the measurements presented here may be improved over time.